creative commons

COMMONS DEED

저작자표시-비영리-변경금지 2.0 대한민국

이용자는 아래의 조건을 따르는 경우에 한하여 자유롭게

- 이 저작물을 복제, 배포, 전송, 전시, 공연 및 방송할 수 있습니다.

다음과 같은 조건을 따라야 합니다:

저작자표시. 귀하는 원저작자를 표시하여야 합니다.

비영리. 귀하는 이 저작물을 영리 목적으로 이용할 수 없습니다.

변경금지. 귀하는 이 저작물을 개작, 변형 또는 가공할 수 없습니다.

- 귀하는, 이 저작물의 재이용이나 배포의 경우, 이 저작물에 적용된 이용허락조건을 명확하게 나타내어야 합니다.
- 저작권자로부터 별도의 허가를 받으면 이러한 조건들은 적용되지 않습니다.

저작권법에 따른 이용자의 권리는 위의 내용에 의하여 영향을 받지 않습니다.

이것은 이용허락규약(Legal Code)을 이해하기 쉽게 요약한 것입니다.

Disclaimer

dCollection

[UCI]I804:48009-200000222449

DOCTOR OF PHILOSOPHY

SYNTHESIS AND PHYSICAL PROPERTIES OF MICRO-NANOSTRUCTURED V_2O_5: STRUCTURE, OPTICAL CHARACTERIZATION, AND APPLICATION

THE GRADUATE SCHOOL

OF THE UNIVERSITY OF ULSAN

DEPARTMENT OF PHYSICS

LE, KHAC TOP

SYNTHESIS AND PHYSICAL PROPERTIES OF MICRO-NANOSTRUCTURED V_2O_5: STRUCTURE, OPTICAL CHARACTERIZATION, AND APPLICATION

Supervisor: Prof. SOK WON KIM

A DISSERTATION
Submitted to the Graduate School of University of Ulsan
in Partial Fulfillment of the Requirements for the Degree
DOCTOR OF PHILOSOPHY IN PHYSICS

By
LE, KHAC TOP

Department of Physics

Ulsan, Korea

May 2019

SYNTHESIS AND PHYSICAL PROPERTIES OF MICRO-NANOSTRUCTURED V_2O_5: STRUCTURE, OPTICAL CHARACTERIZATION, AND APPLICATION

This certifies that the dissertation

of Le Khac Top is approved

Committee Chair Professor Byung-Gook Yoon

Committee Member Professor Sok Won Kim

Committee Member Professor Sung Hyon Rhim

Committee Member Professor Kibog Park

Committee Member Dr. Manil Kang

Department of Physics

Ulsan, Korea

May, 2019

ACKNOWLEDGEMENTS

Firstly of all, I would like to express my devout gratitude to my advisor Prof. Sok-Won Kim, for his devoted supervision and incessant support to my Ph.D. study.

I also would like to express my sincere gratitude to co-advisor Dr. Manil Kang, for his helpful directions, supportive comments, and suggestions.

I am very thankful to Dr. Jaeran Lee and lab-mates who have been provided me with constant help during my study at Laser imaging lab.

I would like to thank all Professors in the Department of Physics, University of Ulsan, who have lectured for my Ph.D. study.

I would like to thank the Vietnamese and Korean students of the Department of Physics and the Department of Chemical Engineering. I am very grateful to everybody who has been supporting vital materials, synthesis equipment, and measurement systems for my research. In particular, I would like to thank Spintronic Materials Lab (Prof. Sunglae Cho), Semiconductor Device Research Lab (Prof. Yong-Soo Kim), Organic Electronic Physics Lab (Prof. Shin-Uk Cho), and Flexible Nanomaterials Lab.

Finally, deep in my heart, I would like to thank my extended family, my wife, and my daughter for their fervent love, sympathy, and encouragement during this arduous journey, and in fact without these it is impossible to attain such applaud able achievements.

Le Khac Top

ABSTRACT

Bulk V_2O_5 is a diamagnetic semiconductor with a band gap (E_g) of about 2.30 eV, which is based on the ionic configuration with filled O*2p* and unoccupied V*3d* orbitals. However, the special electronic structure of V_2O_5 forms three bands, including V*3d* states, V*3d* split-off states, and mid-gap states, which lead to interesting optical properties of V_2O_5 micro-nanostructures. They have four main transitions, including the transition between VB and V*3d* states of CB, the transition between VB and V*3d* split-off of CB, the transition between VB and the mid-gap defect state, and the transition between mid-gap defect states and CB. Therefore, the band edge absorption and photoluminescence (PL) peak positions of low-dimensional V_2O_5 materials do not coincide and are distributed over wide ranges of 0.75 to 3.49 eV and 0.73 to 3.30 eV, respectively. The wide ranges of band edge absorption and broad PL of V_2O_5 micro-nanostructures are clarified in terms of factors such as the morphology, synthesis method, growth conditions, crystal size, micro-nano size, phase transition, and measurement conditions. These factors not only affect the broad emission but also the PL intensity.

Fundamental understanding of the optical characteristics plays a key role in V_2O_5 micro-nano device applications. This thesis summarizes and analyzes the fabrication processes, structure, optical characterization, and photocatalytic activity of V_2O_5 micro-nanostructures, including thin films (TFs), nanoparticles (NPs), micro-nanorods (NRs), micro-nanowires (NWs), nanospheres (NSs), nanohollows (NHs), and V_2O_5/RGO nanocomposites. The relations among the separation, diffusion, recombination, and degradation of the electron-hole pairs in V_2O_5 micro-nanostructures are also discussed. The thesis also demonstrates the role of V_2O_5 micro-nanostructures and other materials (OMs) in V_2O_5/OMs heterostructures for slowing down recombination, prolonging lifetime, improving electron-hole separation, and increasing photocurrent to enhance the photocatalytic activity.

V_2O_5 TFs with micro-nanostructure were fabricated by an electrodeposition method using an aqueous solution of NH_4VO_3. The annealing temperature strongly affects the surface morphology, crystal structure, and photoluminescence (PL) properties. The formation of α-V_2O_5 structure occurred when the sample was annealed at temperatures below 500 ℃. As the annealing temperature increases, some of the α-V_2O_5 structures were distorted and restructured

to form a high-quality mix of α-β phase V_2O_5. This leads to wide absorption and enhancement of the visible-light due to the presence of numerous defects on the surface of the V_2O_5 films.

V_2O_5 nanostructures of NPs, NRs, NWs, NSs, and NHs were prepared by hydrothermal and chemical reaction methods. The morphology measurements showed well-shape nanostructures, the X-ray diffraction (XRD) and Raman results revealed that all nanostructures had an α-V_2O_5 phase with an orthorhombic structure. A large increase of the V^{4+} oxidation state in NSs compared to the other nanostructures was observed by X-ray photoelectron spectroscopy (XPS) measurements and confirmed by Raman spectroscopy. The results show that a larger number of V^{4+} oxidation states of V_2O_5 NSs strongly enhanced PL intensity compared with other structures that showed weak PL. In particular, V_2O_5 NSs showed intense ultraviolet (UV) PL near 395 nm (~3.14 eV) due to strong excitation by UV light, while this PL peak was not observed from other nanostructures.

The bottom level of the CB of V_2O_5 has to be less negative than the redox potential of H^+/H_2 (eV vs. NHE), but electrons in the CB can react in the oxidation reaction with dye solution due to the special electron structure of V_2O_5. A large amount of charge separation in V_2O_5 NSs and the large surface contact area in V_2O_5 NHs and NPs result in more efficient photocatalytic activity than from V_2O_5 NRs and NWs. Reduced graphene oxide (RGO) was mixed with pure V_2O_5 nanostructures to form V_2O_5/RGO nanocomposites. The peak photoluminescence (PL) intensity is around 670 nm in the V_2O_5/RGO nanocomposites, which is much lower than that of pure V_2O_5. This seems to be evidence of facile electron transfer from V_2O_5 to RGO due to the strong adhesion of RGO with pores on the V_2O_5 surface. This leads to the enhancement of the sunlight photocatalytic activity of the V_2O_5/RGO nanocomposites. The relation between the separation, diffusion, recombination, and degradation of the electron-hole pairs in the V_2O_5 nanostructures and V_2O_5/RGO nanocomposite is discussed.

TABLE OF CONTENTS

LIST OF FIGURES

LIST OF TABLES

Chapter 1. Introduction and Background

1.1 Introduction

Vanadium is a highly abundant element in the Earth's crust and can exist in different valence states. The principal oxides of vanadium occur as single valence oxide in the oxidation states of V^{2+} to V^{5+}, which are in the forms of vanadium monoxide (VO), vanadium sesquioxide (V_2O_3), vanadium dioxide (VO_2), and vanadium pentoxide (V_2O_5).[1–3] Moreover, the oxygen vacancies in the vanadium-oxygen phase can form a mixture of valence oxides, such as V_3O_7, V_4O_9, and V_6O_{13} (a mixture of V^{5+} and V^{4+}), as well as a series of oxides: V_6O_{11}, V_7O_{13}, and V_8O_{15} (a mixture of V^{4+} and V^{3+}).[2] The mixing phase forms two series of phases: the Magnéli phase V_nO_{2n-1} and the Wadsley phase V_nO_{2n+1}.[4]

The oxidation states of vanadium depend on ambient conditions such as the temperature, pressure, phase, vanadium concentration, pH, and fabrication method. With changing oxygen concentration, VO_x fabricated by the sputtering method changes phase sequentially ($V \rightarrow V_2O \rightarrow VO_2 \rightarrow V_2O_3 \rightarrow V_6O_{13} \rightarrow V_2O_5$).[5] In aqueous solutions, the phase transition depends on the vanadium concentration and pH.[6] VO_x exists as multiple phases that depend on the annealing times, annealing temperatures, and O_2/Ar gas ratios in the sputtering method.[7] The three valence states of V_2O_5, VO_2, and V_2O_3 can be controlled by using annealing atmospheres of air, vacuum, and a mixture of 95% Ar/5% H_2 gas when using a single polyol route with vanadium ethylene glycolate as the only precursor.[8]

Among the various vanadium oxides, V_2O_5 is the most stable. Micro-nanostructures of V_2O_5 have attracted a great deal of attention due to their promise in various applications, and they can be fabricated by many different methods. V_2O_5 exists in flue-gas deposits from oil-fired furnaces and residues from elemental phosphate plants.[9] V_2O_5 gels were first synthesized in 1885 from ammonium vanadate (NH_4VO_3) salt.[10] The first analysis of the crystal structure of V_2O_5 was carried out by Ketelaar in 1935.[11] One of the most important applications of V_2O_5 is its ionic storage capacity due to its layer structure. Some papers have reviewed V_2O_5 micro-nanostructures in battery applications.[1,9,12–15] Li, Na, K, Ca, Mg, and Al are metals that have been used in V_2O_5 micro-nanostructures for batteries. The injection or extraction of metal ions can change the color of the V_2O_5 film, so it is usually used in electrical and optical switches and smart windows.[16,17] Fig. 1.1 shows a survey of the published literature about V_2O_5 for use

in ionic storage from 1980 to 2015.[12] V_2O_5 has also been widely used in electrochemical,[18] electrochromic,[19] and thermoelectric devices,[20] as well as photocatalytics,[21,22] anti-biofouling agents,[23] and gas-sensors.[24–26]

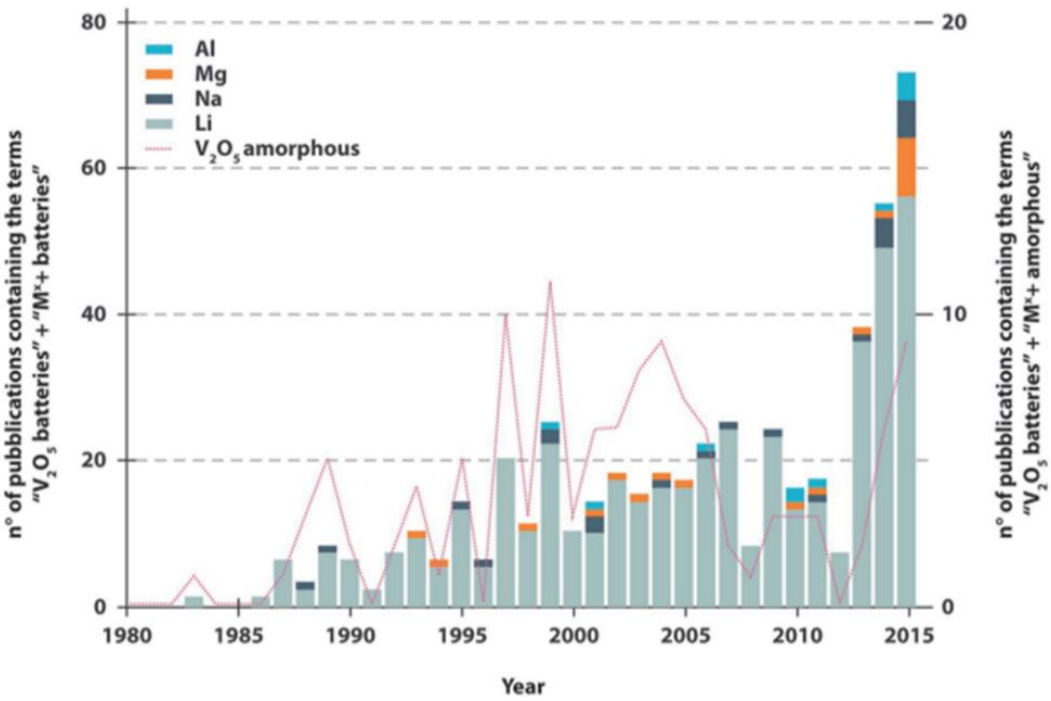

Figure 1.1. Survey of the published literature on V_2O_5 used for ionic storage from 1980 to 2015.[12]

Recently, many efforts have been devoted to improving these promising properties of V_2O_5, including the synthesis of different V_2O_5 micro-nanostructures as one possible avenue. Understanding the effect of the morphology, size, growing conditions, and synthesis methods on the physical properties of V_2O_5 is a very important role for improving the efficiency. Many publications have reported about the optical properties of V_2O_5, but the band edge absorption (optical band gap), PL intensity, and peak position of PL do not coincide. This work discusses the synthesis methods of V_2O_5 micro-nanostructures, including zero-dimensional (0D), 1D, and 2D nanostructures. The effect of V_2O_5 micro-nanostructures on the optical properties is also discussed in depth.

1.2. Preparation methods

1.2.1 Solution method

Solution methods are widely used to fabricate V_2O_5 micro-nanostructures and include hydrothermal, solvothermal, thermal pyrolysis, wet chemical reaction (WCR),

electrodeposition, electrochemical anodization, electrospinning, spray, and sol-gel methods. Solution methods can easily control different morphologies, such as nanoparticles,[27] micro-nanorods,[28] micro-nanotubes,[29] micro-nanowires,[30] micro-nanobelts,[31] nanoribbons,[12] nanospheres,[32] nanohollows,[33] nanoflowers,[34] nanotubulars,[35] three-dimensional porous,[36] micro-nano nests,[37] and ultra-large nanosheets.[38] Fig. 1.2 summarizes some of the morphologies that have been obtained by solution methods.

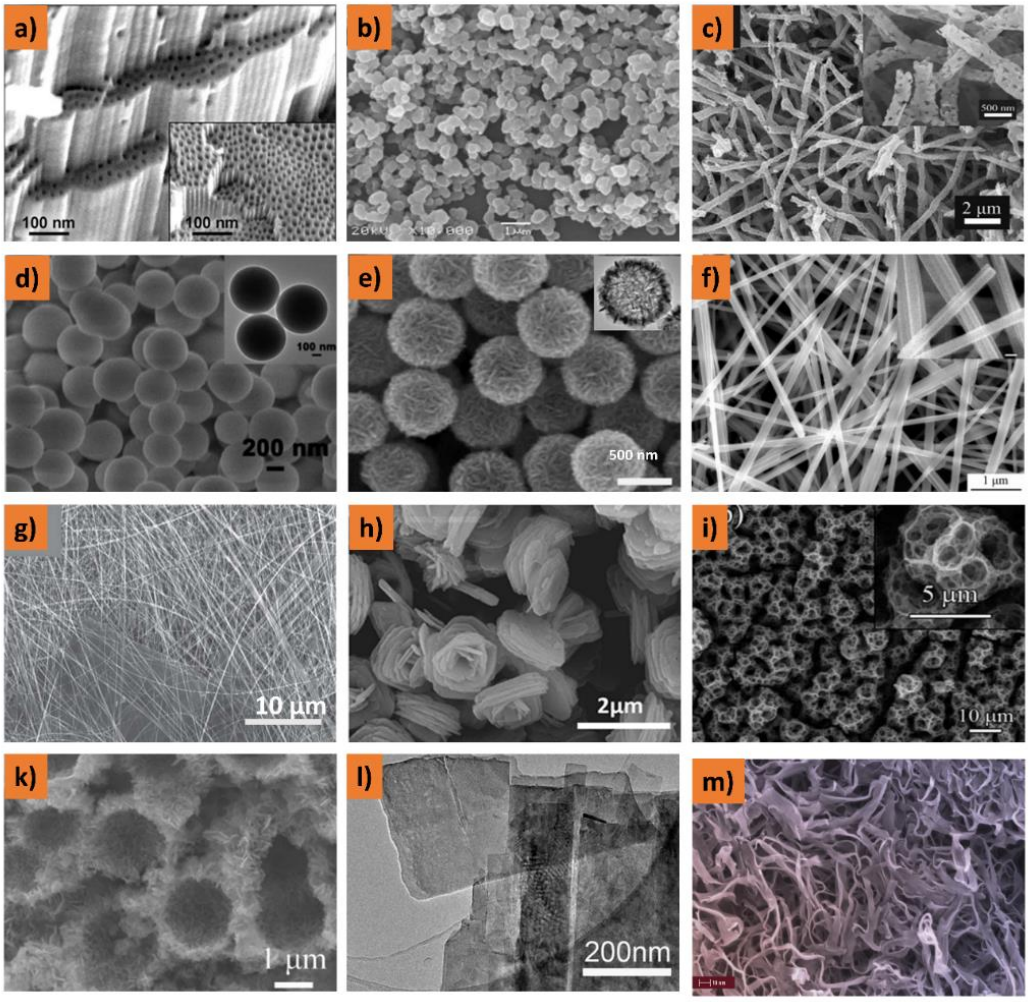

Figure 1.2. Some of the V_2O_5 micro-nanostructures obtained from solution methods: (a) nanotubulars,[35] (b) nanoparticles,[27] (c) nanotubes,[39] (d) nanospheres,[32] (e) nanohollows,[33] (f) nanobelts,[31] (g) nanowires,[40] (h) micro-nano flowers,[34] (i) micro-nano porous,[36] (k) micro-nano nests,[37] (l) ultra-large nanosheets,[38] (m) micro-nano ribbons.[12]

Compared with other solution methods, anodization is the most challenging for synthesizing V_2O_5 micro-nanostructures due to the instability of vanadium oxide during growth in water containing an electrolyte. This has led to some works that were not successful in obtaining self-organized V_2O_5 nanotubes or ordered porous layers.[41,42] However, Yang *et al.*[35] successfully

fabricated homogeneous V_2O_5 nanopores and nanotubes by electrochemical anodization using complex fluoride-based electrolytes such as $[TiF_6]^{-2}$ and $[BF_4]^-$. In contrast to the anodization method, hydrothermal and WCR methods are facile and low-cost methods to fabricate and control the morphology of V_2O_5 micro-nanostructures. The pre-solution and temperature are the main factors that affect the morphology in hydrothermal methods.

Mu *et al.*[43] carried out a hydrothermal method at 180 ℃ for 24 h with different pre-solutions (acid — solvent) and obtained different morphologies, including nanoflowers ($H_2C_2O_4$ — C_2H_5OH), nanoballs (HNO_3 — C_2H_5OH), nanowires (HNO_3 — H_2O), and nanorods ($H_2C_2O_4$ — H_2O). Wang *et al.*[44] prepared V_2O_5 micro-nanowires with different growth times. $V_2O_5.nH_2O$ sheets were obtained when the reaction time was short, and nanowires were obtained when the time was extended. This method can also fabricate centimeter-long or ultra-long V_2O_5 nanowires and nanobelts.[30,40,45] Non-hydrothermal methods were used to synthesize nanoparticles and nanoflowers.[27,34]

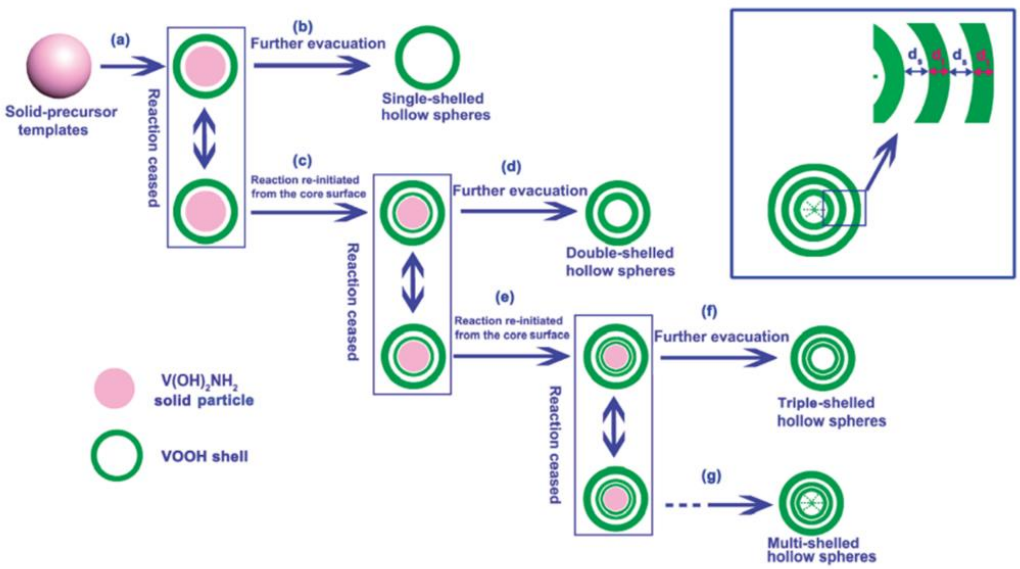

Figure 1.3. Diagram of the transformation of solid templates to single-shelled (a-b), double-shelled (a-c-d), triple-shelled (a-c-e-f), and multi shelled (a-c-e-g) hollow spheres. Inset is the typical multi-shelled hollow spheres, where d_t is the shell thickness, and d_s is the neighboring shell-to-shell distance.[46]

Recently, V_2O_5 micro-nanospheres and micro-nanohollows have been extensively studied using WCR or a combination of WCR and hydrothermal treatment methods. Homogenous solid micro-nanospheres were prepared by WCR at room temperature and annealed at 350 ℃.[47,48] Many kinds of V_2O_5 micro-nanohollows with different surface morphologies can be obtained

by using many different growth conditions in hydrothermal treatments, such as assembled nanoplates,[49] nanoplates with random orientation,[50] double shells,[51] rough-surface hollows,[52,53] single-crystal assembled nanorods,[54] rice-like nanorods,[33] hollows assembled from nanosheets,[55] and multiple shells.[46,55] By combining WCR and hydrothermal methods, ultra-large V_2O_5 nanosheets and mesoporous were synthesized.[38,56] Wu *et al.*[46] reported on the control of the outer shell of micro-nanohollows from $V(OH)_2NH_2$ solid spheres by using a programmed reaction temperature process, as shown in Fig. 1.3. Core/shell structures with different diameters (shell thickness d_t and shell-to-shell distance d_s) were obtained when the sample was heat treated in the range of 100 to 160 ℃. Double-shell hollow spheres were formed by treatment at higher temperature (at 160 ℃). Moreover, different morphologies of V_2O_5 micro-nanostructures can also be controlled by heat treatment.

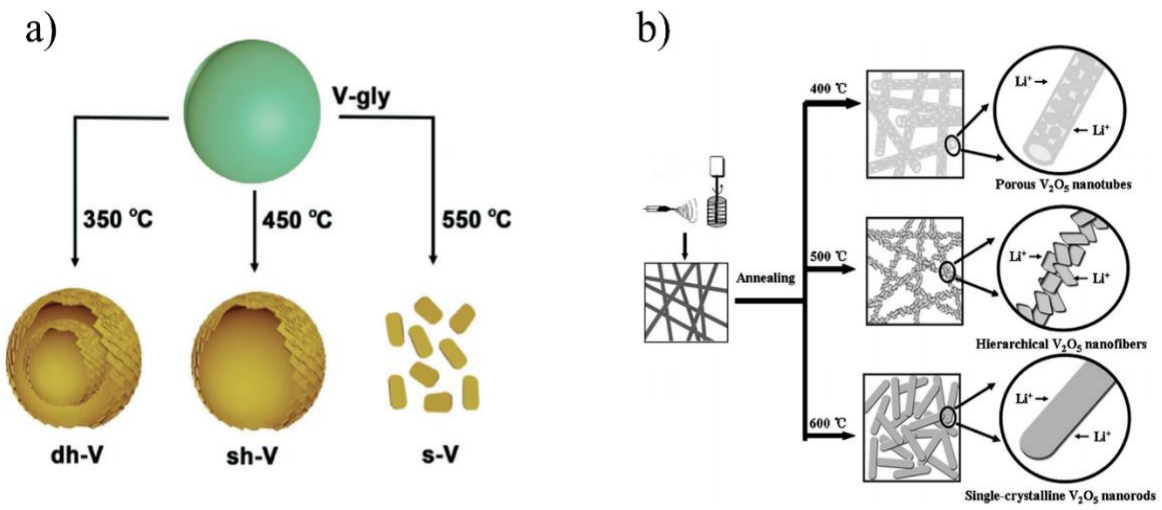

Figure 1. 4. The effect of heat treatment on the morphology of V_2O_5 micro-nanostructures. (a) WCR method,[32] (b) Electrospinning method.[39]

Feifan *et al.*[32] fabricated single-shelled hollows, double-shelled hollows, and nanoparticles using heat treatment at different temperatures and vanadyl glycerolate spheres (Fig. 1.4a). The double-shell hollows were formed by annealing at 350 ℃, single-shell hollows were formed by annealing at 450 ℃, and the hollow spheres were broken down to form nanoparticles by annealing at 550 ℃. Similarly, Wang *et al.*[39] investigated the effect of subsequent annealing using the electrospun technique (Fig. 1.4b). V_2O_5 nanostructures were formed as nanotubes at 400 ℃, nanofibers were formed at 500 ℃, and nanorods were formed at 600 ℃. Wang *et al.*[36] controlled the form from a two-dimensional form to a three-dimensional porous form by using

electrostatic spraying at different temperatures for different times. Moreover, V_2O_5 nanorods, nanoparticles, nanotubes, and mesopores can also be obtained by electrodeposition.[29,57–59]

1.2.2 Chemical vapor deposition method

Chemical vapor deposition (CVD) or chemical vapor condensation (CVC) methods include thermal and low-temperature CVD,[60,61] low and atmospheric-pressure CVD (L-APCVD),[62] atomic layer CVD (ALCVD),[63] metal organic CVD (MOCVD),[64,65] aerosol-assisted CVD (AACVD), and plasma-enhanced CVD (PE-CVD).[66] These techniques are mainly based on the vapor and reaction of vanadium-based organometallic precursors in the gas phase and on the substrate surface to synthesize V_2O_5 micro-nanostructures. The morphology, size, crystal phase, specific surface area, surface composition, and chemical state of the V_2O_5 nanostructures can be controlled by regulating several factors, such as the reaction time, reaction temperature, pressure, solvent properties, precursor composite, and reaction position in the system.[67]

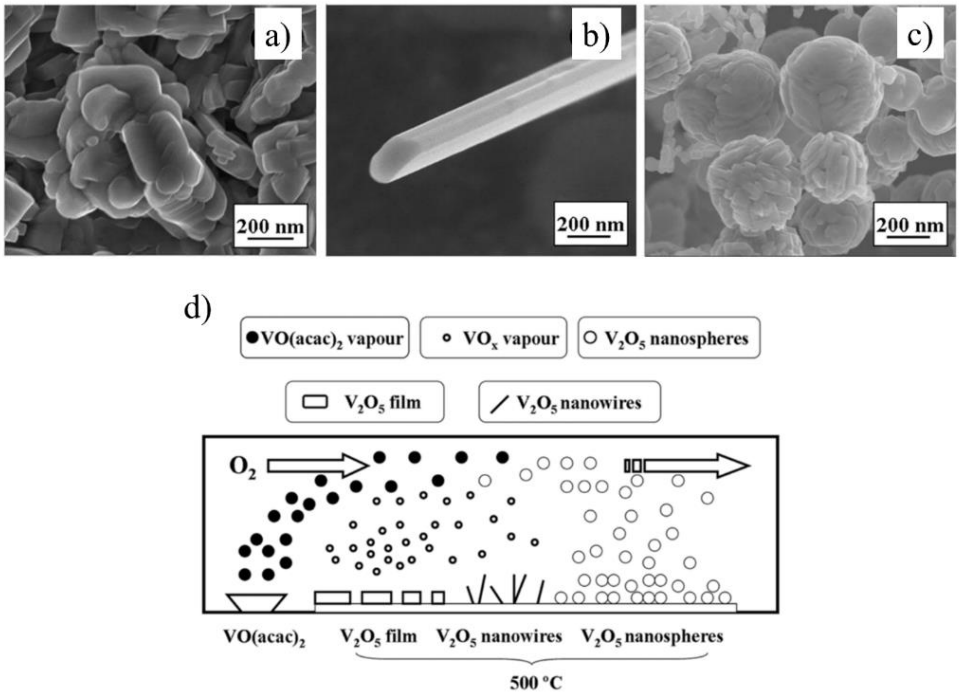

Figure 1.5. (a) V_2O_5 film at 13 cm, (b) nanowires at 18 cm, (c) nanospheres at 30 cm, and (d) diagram of the V_2O_5 nanomaterial growth prepared by CVD.[61]

Among these factors, the temperature is the most important to control the morphology and the size of micro-nanostructures. Le *et al.*[67] reported on the effect of the synthesis temperature on the size and surface area of V_2O_5 particles. Samples prepared at 500 and 700 ℃ had porous

morphology, while different nanoparticle sizes of 15, 60, and 30 nm were obtained at 900, 1100, and 1300 ℃, respectively. Morphologies such as nanoparticles (200 ℃),[68] thin films (300 – 600 ℃),[62] and nanowires with 50-nm diameter and micro-scale length (1100 ℃)[69] can be formed using different temperatures in the L-APCVD technique. The effects of the synthesis temperature on the smoothness, roughness, and surface morphology of V_2O_5 thin film were also investigated using CVD,[60] ALCVD,[63] and MOCVD.[64]

Recently, micro-nano morphologies were controlled by a modified CVD route. Wang *et al.*[61] used the CVD method to control the morphologies of V_2O_5 by changing the reaction position, as shown in Fig. 1.5. V_2O_5 nanocluster thin-films were formed at a high concentration and supersaturation of VO_x in the region near the source material (about 13 cm away). Nanowires were formed at 18 cm due to the low vapor concentration of VO_x, while nanospheres were obtained when the source material was far away (about 30 cm) due to the high concentration and supersaturation of vanadyl acetylacetonate. Similarly, 1D porous V_2O_5 micro-nanotubes were obtained at 55 cm.[70]

1.2.3 Physical vapor deposition method

The most popular techniques to grow 2D film are physical vapor deposition (PVD) methods, including pulsed laser deposition (PLD), pulsed laser ablation (PLA), electron beam evaporation (E-beam), thermal evaporation (TE), melt quenching (MQ), sputtering deposition (including radio-frequency (RF) magnetron sputtering and direct current (DC) magnetron sputtering), and ion beam magnetron sputtering (EB).[71] In comparison with solution and CVD methods, it is difficult to control the V_2O_5 micro-nano morphologies in PVD due to the process of growth in a vacuum and plasma environment. Film morphologies prepared by PVD methods include rod-like films,[72] β-V_2O_5 nanorods,[73] micro-rods, urchin-like structures, nanotips,[74] and perpendicular micro-nano platelets.[75]

Kang *et al.*[72] reported V_2O_5 nanorod films that were grown using an E-beam method. The morphology and crystal structure were affected by the buffer layer and beam dose rate irradiation. The V_2O_5 nanorods were obtained with a beam irradiation dose of 800 kGy both with and without a buffer layer, as shown in Fig. 1.6. Zou *et al.*[76] carried out sputtering on different substrates and post-annealing treatment. The as-grown films on both glass and silicon were amorphous, while β-V_2O_5 phase (on the glass substrate) and α-V_2O_5 phase (on the silicon substrate) were obtained when the sample was annealed at 500 ℃ for 1 h. Other film

morphologies such as nanoparticle hollow-spheres, nanowires, and nanotubes were also fabricated by using combinations with other techniques.[24,77,78] V_2O_5 powder was melted by heating it at high temperature (800 ℃) and quickly poured into water under vigorous stirring. The solution was kept in an autoclave at 200 ℃ for 4 days to obtain V_2O_5 nanowires[24] or kept at room temperature for 7 days, and then an alumina template membrane was dipped into the sol to obtain V_2O_5 nanotubes.[77]

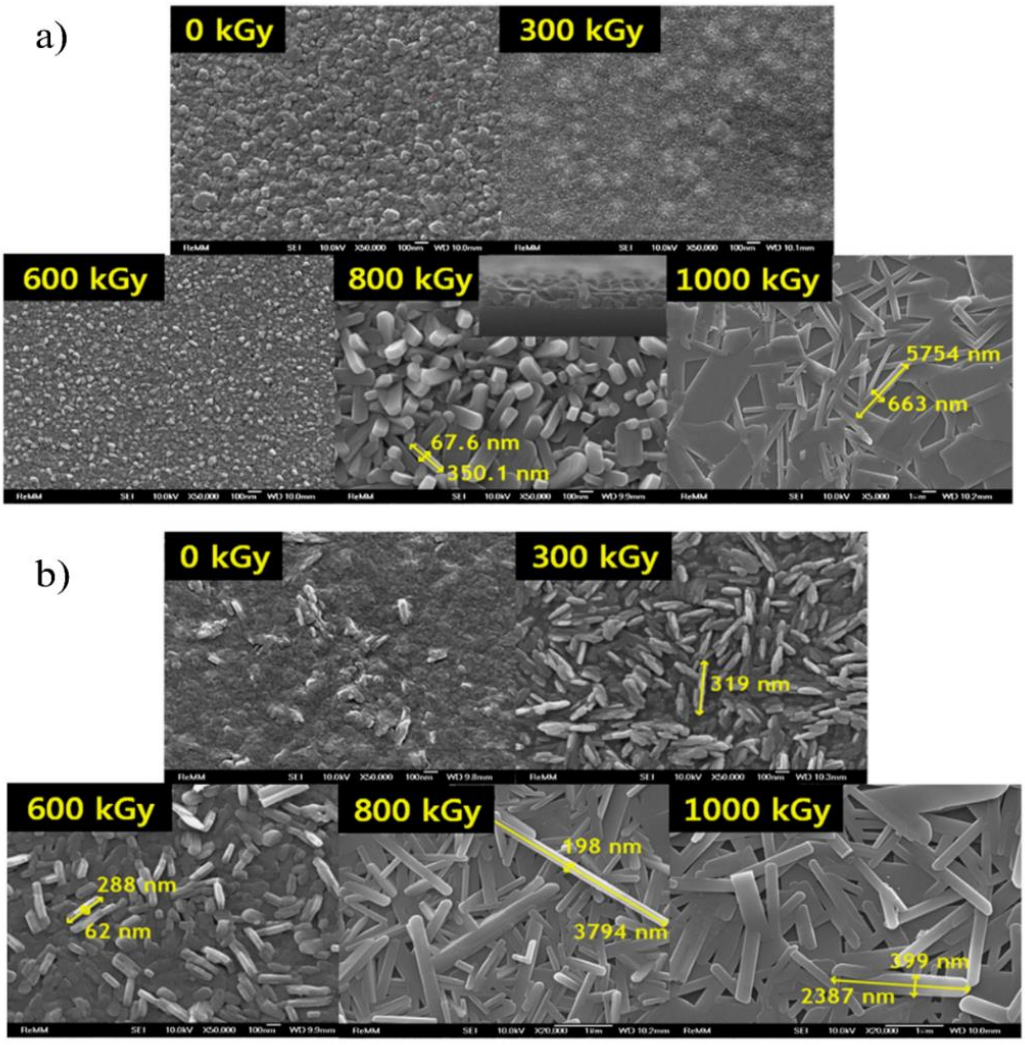

Figure 1.6. The surface morphologies of the V_2O_5 film: (a) Without buffer layer, (b) With buffer layer.[72]

1.3. Structures

1.3.1 Crystal structure

V_2O_5 exists as polymorphic phases that include α-V_2O_5, β-V_2O_5, γ-V_2O_5, and δ-V_2O_5.[79] The α-V_2O_5 phase is the most stable phase and has lattice parameters of a = 1.1512 nm, b = 0.3564 nm, and c = 0.4368 nm. Metastable β-V_2O_5 (a = 0.7111 nm, b = 0.3579 nm, and c = 0.629 nm), mixture of α-β phase V_2O_5, γ-V_2O_5, and δ-V_2O_5 can be obtained by transition from α-V_2O_5 at high temperature or high pressure.[76,80–82] The phase transition of the V_2O_5 structure is also affected by the substrate, film thickness, and synthesis method.[73,76,83,84] The polyhedrons share edges to form $(V_2O_4)_n$ zigzag double chains along the (001) direction and are cross linked along the (100) direction through shared corners.[85] In this structure, there are three types of oxygen centers around vanadium atoms, including terminal (vanadyl) oxygen O(1), O(2) bridging over two vanadium centers, and O(3) bridging over three oxygen coordinated vanadium centers, as shown in Fig 1.7a.[86–88]

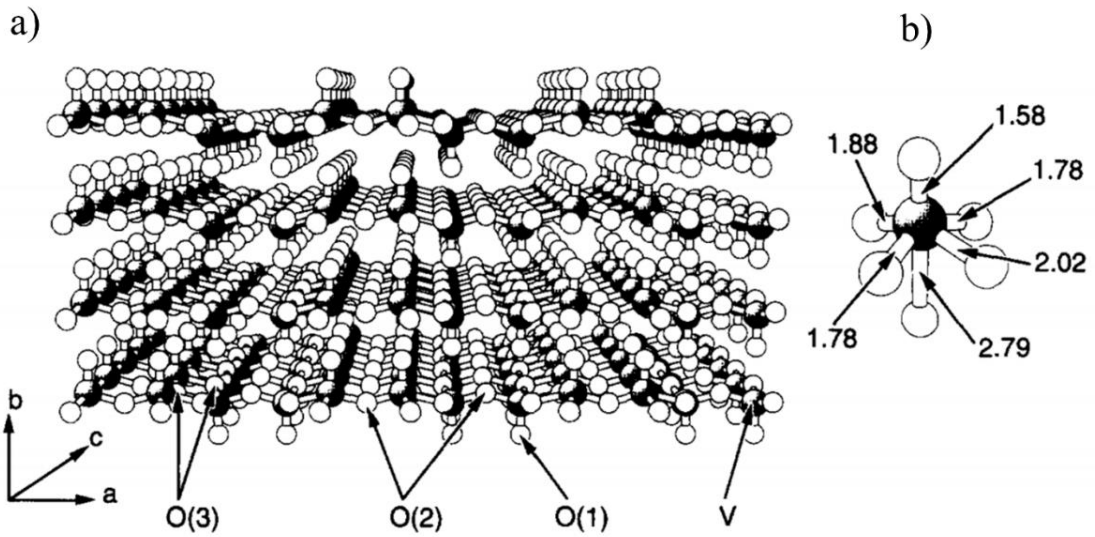

Figure 1.7. The crystal lattice structure of V_2O_5. (a) The location of the vanadium centers, V, and symmetry in equivalent layer/surface oxygen sites, O(1)-O(3) and (b) oxygen coordination around vanadium atom and the V-O distances are done in Å.[88]

O(1) forms only one bond with vanadium with an O(1)-V distance of 1.58 Å, as shown in Fig. 1.7b. O(2) forms two bonds of V-O(2)-V with an O(2)-V distance of 1.78 Å, while O(3) forms three bonds with two bonds with an O(3)-V distance of 1.88 Å and one bond with an O(3)-V distance of 2.02 Å. Moreover, layers form a bond with an O(1)-adjacent layer distance of 2.79 Å.[88] V_2O_5 is an oxygen-deficient semiconductor where oxygen is removed from the crystal at O(1), O(2), or O(3) to form V^{4+} or V^{3+} oxide states. In all possible oxygen vacancies, oxygen site O(1) is the least stable, while the O(3) site is the most stable.[88]

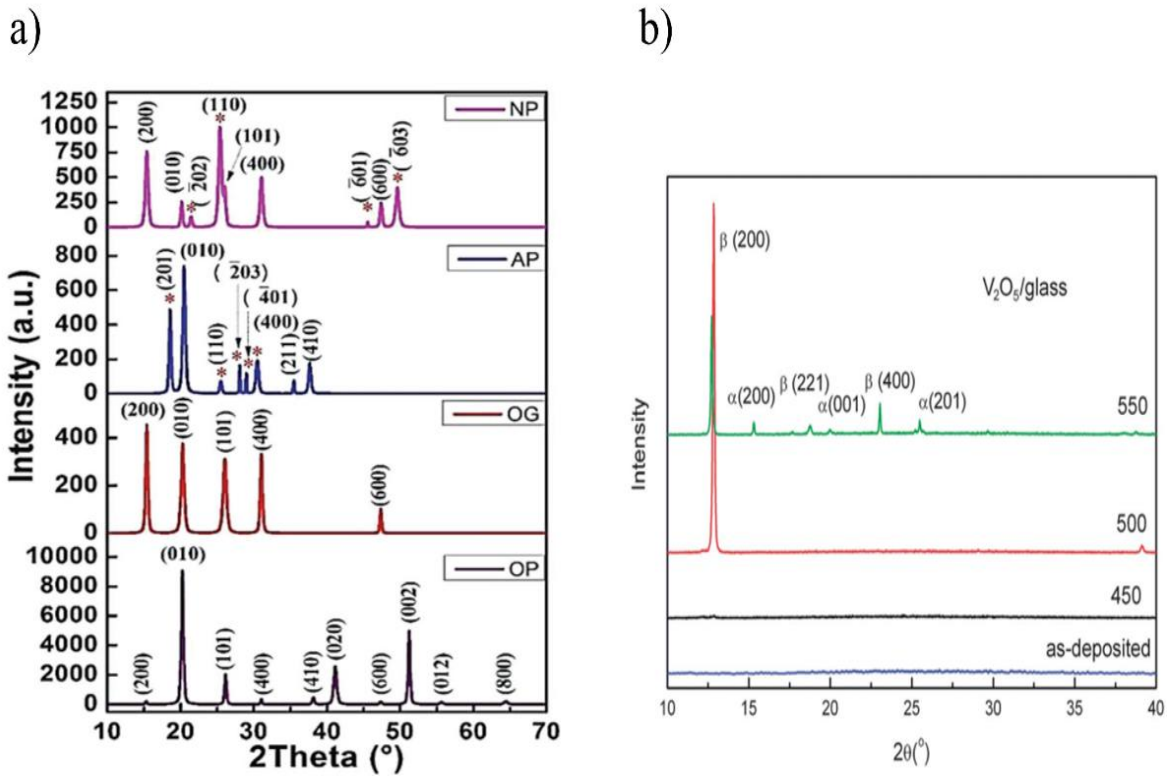

Figure 1.8. The XRD diffraction of V_2O_5 film. (a) Deposited in different gas: oxygen plasma (OP), oxygen gas (OG), argon plasma (AP), and nitrogen (NP),[90] (b) Annealing at different temperatures.[91]

Xiao *et al.*[89] calculated the formation energies of three types of oxygen-vacancies. In both relaxed and unrelaxed cases, E_{vac} of the O(1) vacancies is the lowest, while E_{vac} is the highest in O(3) (relaxed case) and O(2) (unrelaxed case). The formation energies of the oxygen vacancies in V_2O_{5-x} with O(1), O(2), and O(3) are 2.48, 4.17, and 4.44 eV, respectively.[89] These oxygen vacancies lead to the formation of a mixture of two phases of V_2O_5 and V_6O_{13}. Megha *et al.*[90] fabricated V_2O_5 nanostructures by a plasma-assisted sublimation process in different gases (O_2, N_2, and Ar). Fig. 1.8 shows the XRD spectroscopy results of mixed chemicals and mixed crystal phases of V_2O_5 micro-nanostructures. The results show the formation of V_2O_5, mixed V_2O_5-V_6O_{13}, and V_6O_{13} phase depending on the amount of oxygen vacancies (Fig. 1.8a). V_6O_{13} becomes the most stable phase if a sufficient amount of oxygen is removed from the V_2O_5 structures.

Zou *et al.*[76] investigated the effect of the annealing temperature on V_2O_5 film fabricated by magnetron sputtering. The results reveal that the annealing temperature not only affects the forming crystals but also causes phase transition in the local crystallization of the V_2O_5 structure. At higher temperature (550 ℃), the V_2O_5 films form mixed phases of α-V_2O_5 and β-V_2O_5

structures (Fig. 1.8b). The annealing temperature affects the forming crystals and causes phase transition in the local crystallization of the V_2O_5 structure. During the annealing, the energy for the diffusion of V and O ions is enough to form α-V_2O_5 at low temperature (below 500 ℃). At higher temperature (550 – 650 ℃), some of the α-V_2O_5 structures become unstable and are distorted to form mixed phases of α-V_2O_5 and β-V_2O_5 structures.[91]

1.3.2 Band structure

Pure V_2O_5 is a diamagnetic semiconductor, and its band structure is based on an ionic configuration with filled O*2p* orbitals and unoccupied V*3d* orbitals. Chakrabarti *et al.*[86] used density functional theory (DFT) to calculate the density function of the V_2O_5 bulk and the V_2O_5 surface, as shown in Fig. 1.9. The result shows that V_2O_5 bulk has a direct band gap of 2.30 eV at the Γ point and an indirect gap (corresponding to a transition R to Γ) of 1.90 eV. A V_2O_5 (010) single-layer slab has a direct gap of 2.30 eV and an indirect gap of 2.10 eV. The valence-band widths are 5.5 ± 0.5 eV and 5.0 ± 0.5 eV for bulk and single-layer V_2O_5, respectively. Eyert and Hock did calculations based on DFT and the local-density approximation (LDA) by using an augmented spherical wave (ASW) and inserting empty spheres into the open crystal structure of V_2O_5. They showed that the indirect gap of V_2O_5 is 1.74 eV.[92] Similarly, the indirect band shows a separation of about 1.73 eV between the valence band (VB) and the conduction band (CB) according to the linear muffin-tin orbital (LMTO) method.[87]

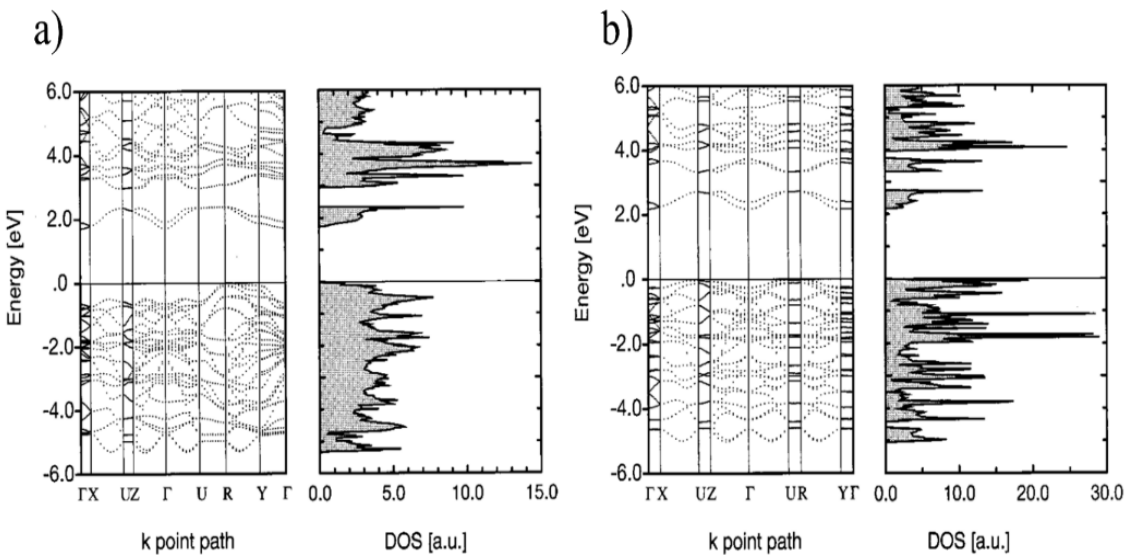

Figure 1.9. Band structure and total densities of states of (a) bulk V_2O_5 and (b) V_2O_5(010) single-layer slab.[86]

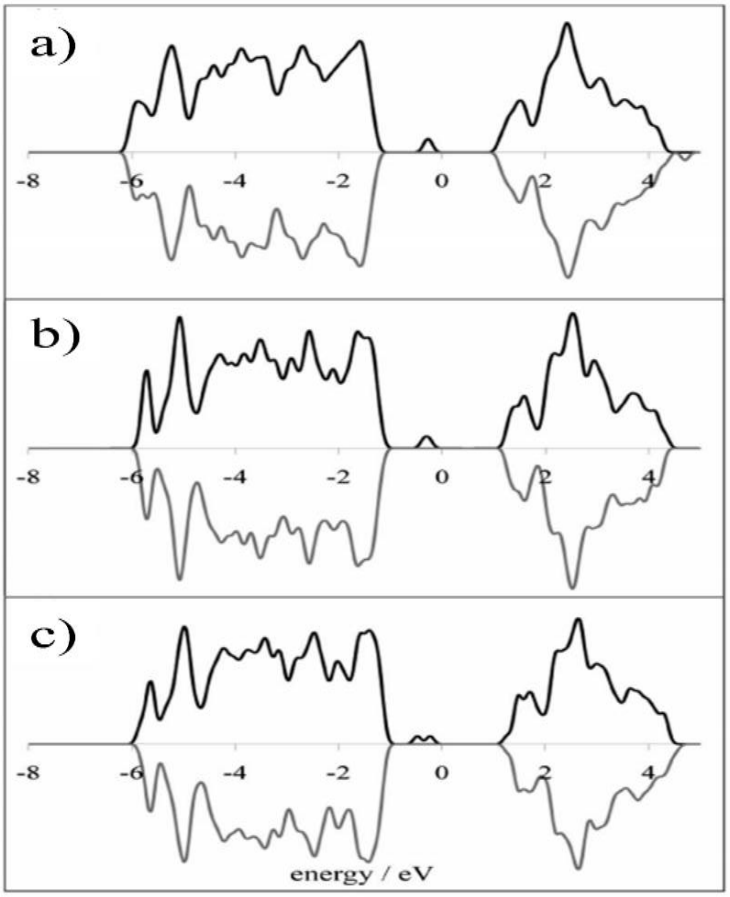

Figure 1.10. The formation of defect states of V_2O_5 oxygen vacancies at different positions. (a) O(1) site, (b) O(2) site, and (c) O(3) site.[93]

Parker *et al.*[94] used the first-principles orthogonalized linear combination of atomic orbitals (OLCAO) method and found an indirect band gap of about 2.00 eV and a direct band gap of about 2.40 eV. However, the calculations show that the CB consists of a pair rather than a localized band from V$3d_{xy}$ and V$3d_{yz}$ (t_{2g} symmetry) with the O2_{py} orbital because of the large effective mass and the presence of another gap above the bottom CB, which is called a split-off band.[94,95] These split-off bands are separated from the higher CB with a gap of 0.60 eV and a gap width of 0.75 eV.[94] Normally, the optical gap or band gap (E_g) of V_2O_5 is defined by the transition between the top of the O*2p* band and the bottom of the V*3d* split-off (Fig. 1.9). Therefore, the gap between the top of the O*2p* band and the bottom of the V*3d* includes an additional ~1.35 eV. V_2O_5 is a semiconductor with a larger energy gap (direct gap) of 3.30 eV, and there is another localized band at ~0.60 eV below the main gap.[74,94,96]

Scanlon *et al.*[93] calculated the formation of mid-gap states at about 0.70 – 1.00 eV due to the oxygen vacancies, which depend on the loose oxygen position in the crystal. Fig. 1.10 shows

the formation of mid-gap states for O(1), O(2), and O(3) vacancies. For the O(1) vacancies, the states are located at about ~0.95 eV, while those of O(2) and O(3) are at about 0.75 eV and 0.69 eV, respectively. Therefore, the electronic structure of V_2O_5 can be seen as a semiconductor with three bands, including two localized bands of the CB and mid-gap band due to the numerous oxygen vacancies.

1.4. Optical properties

1.4.1 Absorption

Absorption occurs when there is light with energy higher than the band gap E_g of materials. In this case, an electron jumps from the VB to the CB by absorbing a photon, which creates an electron-hole pair. The law of conservation of energy to the inter-band transition is shown in Eq. (1.1) and Eq. (1.2).[97]

$$E_f = E_i + \hbar\nu \qquad \text{(Direct gap)} \qquad (1.1)$$

$$E_f = E_i + \hbar\nu \mp \hbar\omega \qquad \text{(Indirect gap)} \qquad (1.2)$$

where E_f is the energy of the final state in the upper band, E_i is the energy of the electron in the lower band, $\hbar\nu$ is the photon energy, and $\hbar\omega$ is the phonon energy. The light intensity of material is characterized by applying Beer's law (Eq.(1.3)):

$$I = I_o \exp^{-\alpha d} \qquad (1.3)$$

where d is the film thickness, and α is the absorption coefficient of the material. The relation between the absorption coefficient and the optical band gap of the material is shown using a Tauc plot and Eq. (1.4).[98]

$$\alpha\hbar\nu = B\left(\hbar\nu - E_g\right)^n \qquad (1.4)$$

where $\hbar\nu$ is the photon energy, B is a constant, E_g is the optical band gap, and n is an exponent that can have values of n = 1/2, 2, 3/2, and 3, which correspond to direct allowed, indirect allowed, direct forbidden, and indirect forbidden transitions, respectively. The calculations and photo-absorption experiments show that V_2O_5 is a semiconductor with both direct and indirect band gaps.

Kang *et al.*[99] measured the direct and indirect band gaps at different temperatures. At 20 K, the band edge is 2.67 eV for the indirect gap and 2.26 eV for the direct gap, while at 300 K, the band edge is 2.64 eV for the direct gap and 2.16 eV for the indirect one. The direct and indirect values depend on the temperature, as shown in Fig. 1.13b. The direct E_g increased to a greater extent during a temperature change of 300 - 150 K than with further changes below 150 K, and the indirect E_g varied more stably below 150 K than above. The electron-phonon interaction and thermal expansion are two distinct mechanisms that affect the temperature dependence of band gap in the semiconductor. The lattice dilation effect due to the change of temperature can contribute to bandgap shifts.[99] Some reports show that the band edge absorption for indirect-direct transition is 2.19 – 2.08 eV,[100] 2.50 – 2.15 eV, and 2.70 – 2.35 eV.[101]

The optical properties of single-crystal V_2O_5 have been investigated to gain a better understanding of the electronic band structure of this material.[94] However, measurement of the optical properties of V_2O_5 micro-nanostructures shows that the properties are strongly affected by many factors, such as the morphology, phase transition, and external treatment. Most of the reports describe the band edge transition at 2.00 to 2.70 eV. Other reports show that the band edge transition is lower, such as 1.72 eV,[102] 1.75 eV,[103] 1.80 eV,[104] and 1.95 eV,[105] or higher, such as 2.85 eV,[106] 2.80 – 2.90 eV,[107] 2.93 eV,[108] 3.27 eV,[109] and 3.49 eV.[102]

The band edge absorption (E_g) has been evaluated in experimental measurements based on Tauc or Cody plots.[110] However, the band structure forms three bands above VB (O*2p* states), including V*3d* states, V*3d* split-off states, and mid-gap states. The number of electron transitions of these states is not the same. V_2O_5 micro-nanostructures also co-exist with different valence phases, such as a mixture of V^{4+} and V^{5+}, as well as different crystal phases, such as a mixture of α-β-V_2O_5 and α-δ-V_2O_5. The morphologies, growth conditions, and synthesis methods can shift the absorption band. Moreover, micro-nano-size also affects the absorption edge due to the quantum confinement effect.[85] Recently, some reports have shown evidence of the semiconductor-metal transition (SMT)[111,112] or metal-insulator transition (MIT)[71,113] of V_2O_5 micro-nanostructures. This leads to a difference in the peaks and tail absorption spectroscopy due to the overlap of peaks.

At room temperature, when pure α-V_2O_5 absorbs the photon from an excitation source, electrons can jump to a higher state in four ways, as shown in Fig. 1.15a: (1) from VB to V*3d* states of CB, (2) from VB to V*3d* split-off states of CB, (3) from VB to mid-gap states, and (4) from mid-gap states to CB. The increase in intensity of these processes depends on the local

structure of V_2O_5 and the excitation source. Almost all reports indicate that the absorption of V_2O_5 is based on the transition between O*2p* and V*3d* split-off bands corresponding to the band edge at about 2.30 eV. Electron transition from occupied O*2p* to unoccupied V*3d* strongly occurs due to the quantum confinement effect of V_2O_5 nanoparticles. As a result, the absorption edge shows a blue and a violet shift.[106,108]

The tailing absorption also depends on the coordination between oxygen and V^{5+} ions, including tetrahedral coordination (from 217 to 270 nm), square pyramidal coordination (from 282 to 410 nm), and octahedral coordination (from 411 to 570 nm).[114] Kenny *et al.*[115] measured the absorption of single-crystal V_2O_5 following the crystal direction. The band edge occurs at 2.15, 2.22, and 2.17 eV for E//a, E//b, and E//c, respectively. Clauws and Vennik investigated the infrared absorption and found two bands at 1.25 and 1.52 eV for E//a and one band at 1.00 eV for E//b due to defects.[116] In addition, the transition from O*2p* to the *d* band structure of vanadium results in bands centered at 2.92 eV for E//a and 3.15 eV for E//c.[117]

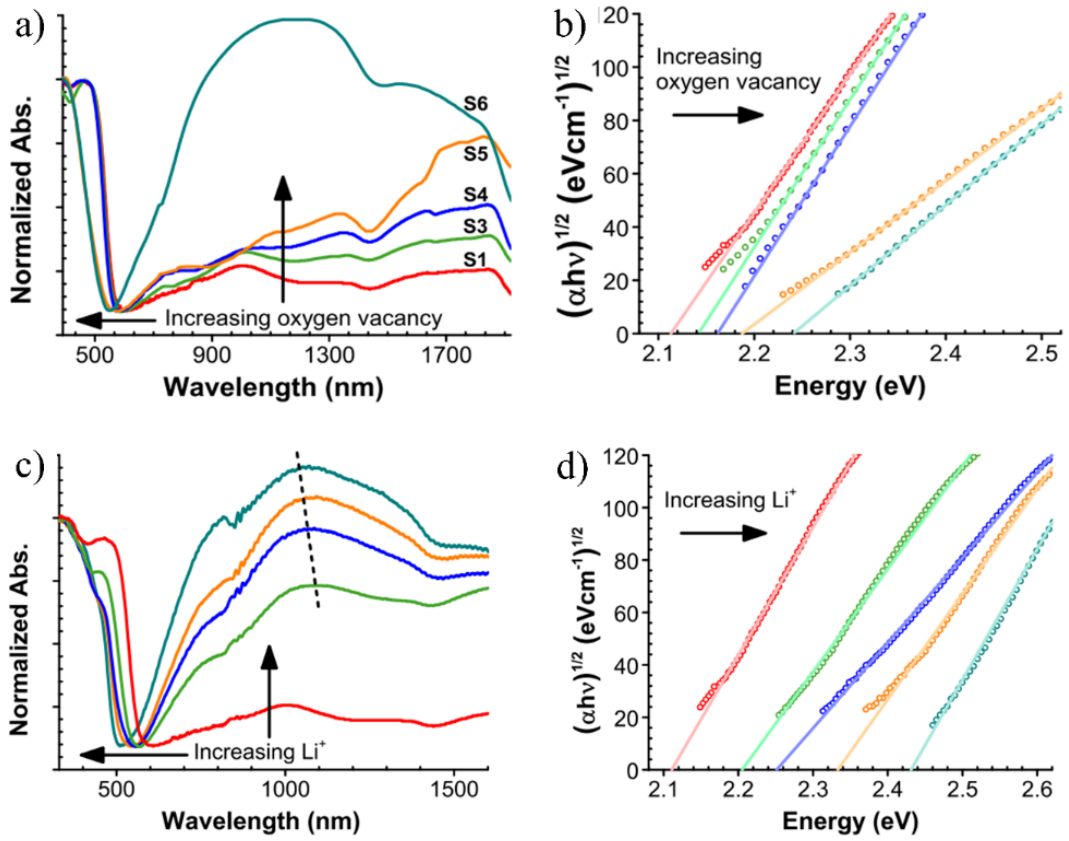

Figure 1.11. The oxygen vacancy dependence and Li inserting dependence of the absorption spectrum of V_2O_5 nanowires.[118]

Fig. 1.11 shows the effect of the oxygen-vacancy concentration and inserting Li^+ on the absorption of V_2O_5 film. Wang *et al.*[118] reported absorbance in the near-infrared (NIR) region due to a strong increment of the transition between mid-gap states and V*3d* states with increasing oxygen vacancies and lithium intercalation, as shown in Fig. 1.11a and c. Li^+ and oxygen vacancies also increase the band gap from 2.10 to 2.45 eV (Li^+ intercalation) and from 2.10 to 2.25 eV (oxygen vacancies), as shown in Fig. 1.11b and d. The band edge also increases due to the Li^+. Therefore, E_g increases from 2.03 to 2.62 eV (x = 0 to 0.54)[119] and from 2.25 to 3.10 eV (x = 0.0 to 0.75) in $Li_xV_2O_5$.[96]

When the electron concentration in V_2O_5 increases due to the insertion of electrons and lithium ions into the film, the Fermi level moves up to near the split-off band and enters it as the concentration becomes large enough. This leads to a wide optical gap with $E_g = E_{g0} + \Delta E_g^{BM}$, where E_{g0} is the optical gap of pure V_2O_5, and ΔE_g^{BM} is the Burstein-Moss shift.[119] The presence of V^{4+} due to the formation of defects in the V_2O_5 film leads to a tailing absorption shift to low energy at about 635 – 710 nm.[103–105] The large oxygen-vacancy absorption is separated into two distinct regions: (1) high energy due to the transition between VB and CB and (2) low energy due to the transition between VB and mid-gap states. This low-energy absorption just affects the tail absorption when the number of oxygen vacancies is small. The absorption curve of the V_2O_5 film shows two regions: one at $h\nu > 2.30$ eV and one at $h\nu < 2.30$ eV.[120] The second region reveals two distinct absorption bands at 1.20 eV and 1.70 eV.

The optical energy E_g of pure α-V_2O_5 films is also affected by the morphology and growth methods. Table (1.1) shows the band edges of some of the morphologies of V_2O_5 micro-nanostructures obtained with different synthesis methods. Joseph *et al.*[121] studied the local structure of V_2O_5 bulk, nanoparticles, and nanowires. The V-O double chains in the nanowires significantly enhance the atomic order compared with the bulk material, while nanoparticles have a large configuration. This leads to a different electronic structure due to order and disorder in the micro-nanostructures. The band gap of the thin film fabricated by the EB method increases from 2.18 to 2.36 eV with increasing film thickness from 840 to 1200 nm, which corresponds to crystal size reductions of 45 to 31 nm.[122] The band edge decreases from 2.40, to 2.35, 2.15, and 2.02 eV as the thickness increases from 110 to 195, 256, and 365 nm for films synthesized by TE.[123]

Table 1.1. Band-edge absorption of the morphologies and synthetic method of V_2O_5 micro-nanostructures.

Morphology	Method	Note on some parameters	E_g (eV)	Ref
Bulk	Commercial	Bulk powder	2.20	[126]
Precursor Wire Rod	Hydrothermal	2 – 5 μm diameter 20 – 30 nm diameter 30 – 40 nm diameter	2.20 2.55 2.60	[127]
Particle	WCR	10 – 15 nm diameter	2.18	[128]
Particle	WCR	16 nm diameter	2.34	[129]
Particle	WCR	25 – 30 nm diameter	2.85	[106]
Particle	WCR	5 – 8 nm diameter	2.93	[108]
Particle	Sol-gel	96.5 nm diameter	3.27	[109]
Rod	Hydrothermal	90 – 180 nm diameter, ~μm length	2.29	[114]
Rod	Sputtering	β-V_2O_5, ~μm length	2.30	[130]
Rod	WCR	2 – 3μm diameter	2.55	[131]
Wire	CVD	50 – 100 diameter, ten micrometer length	2.48	[126]
Wire	CVD	50 nm diameter, 10 μm length	2.74	[69]

Flower	Hydrothermal	150 nm diameter, ~3 µm length	2.10	[132]
Flower	Sol-gel	~ 5 µm in size	2.19	[133]
Flower	Hydrothermal	~ 5-7 µm in size	2.48	[134]
Flower film	Spray pyrolysis	26 nm crystal size	2.30	[135]
Thin film	Sol-gel	48 nm thickness	2.58	[136]
Hollow	Solvothermal	~700 nm diameter	2.10	[137]
Sphere	Hydrothermal	~ 2.5 µm diameter	2.34	[138]
Sheet	Sol-gel	40 – 80 nm in size	2.25	[139]
Ribbon	TE	300 nm (width), 100 nm (height), and Ultra-long	2.30	[140]
Belt	Hydrothermal	Super length	2.30	[141]
Tube	Melting quench	~95 nm diameter	2.90	[77]
Macro-plates	WCR	10 – 11 µm length	3.40	[142]

The effect of the nanocluster size on the band gap of semiconductor materials was compared via the Bohr radius. The energy gap increases as the diameter of the particles decreases to less than the Bohr radius. The Bohr radius of V_2O_5 is calculated using Eq. (1.5).[124]

$$a_B = \frac{4\pi\varepsilon_0\hbar^2\varepsilon}{e^2 m_0 \mu} = 4.52 \text{ nm} \qquad (1.5)$$

where $\mu = m_e m_h/(m_e+m_h)$ is the reduced exciton mass, and m_e (0.24) and m_h (0.5) are the electron and hole effective masses, respectively. ε_0, ε, and e are the dielectric constant of a vacuum, the dielectric constant of V_2O_5, and elementary charge, respectively. The different energy width of CB between small crystal size and bulk material is described by Eq. (1.6).[125]

$$\Delta E(d) = \frac{2\hbar^2\pi^2}{d^2}\left[\frac{1}{m_e^*}+\frac{1}{m_h^*}\right] - \frac{3.572e^2}{\in d} - \frac{0.124e^4}{\hbar^2\in^2}\left[\frac{1}{m_e^*}-\frac{1}{m_h^*}\right]^{-1} \qquad (1.6)$$

where d is the particle diameter, m_e^* and m_h^* are the reduced masses of an electron and a hole, and $\in$ is the permittivity.

The band edge of V_2O_5 also depends on the synthesis conditions. The energy gap of V_2O_5 film deposited by the EB method increases from 2.04 to 2.30 eV when increasing the oxygen partial pressure from 10^{-7} to 10^{-4} mbar.[143] The optical band changes from 2.45 to 2.43, 2.33, and 2.32 eV with different annealing atmospheres (as-grown, oxygen, vacuum, and air, respectively).[144] The effect of the synthesis conditions on the formation of non-stoichiometry in the V_2O_5 structure leads to the formation of localized states in the gap. The band edge of V_2O_5 films fabricated by a sol-gel method with metalorganic, organic, and inorganic precursors occurs at 1.70, 2.20, and 2.50 eV, respectively.[145] E_g decreased from 2.47 to 2.12 eV, from 2.60 to 2.13 eV, from 2.53 to 2.35 eV, and from 2.29 to 2.02 eV due to the crystallite size and strain value when the annealing temperature was increased from 30 to 500 ℃,[146] from 250 to 350 ℃,[147] from 350 to 500 ℃,[148] and from 275 to 320 ℃,[149] respectively.

Thiagarajan *et al.*[150] investigated the effect of the substrate on the band edge and found E_g = 2.36 eV for glass substrate, 2.10 eV for ITO substrate, and 2.05 eV for FTO substrate. Raj *et a* [102]. investigated the effect of the crystalline nature of V_2O_5 on different substrates on the optical properties. On the glass substrate, the band edge absorption increased from 2.50 to 3.49 eV, which corresponds to the thickness increasing from 148 to 300 nm. On the Si substrate, the band edge changes to 2.32, 1.88, 2.45, and 1.72 eV with thicknesses of 176, 276, 237, and 300 nm, respectively. The different substrates affect the crystal formation, including the amorphous characteristics, polycrystalline characteristics, crystallite size, dislocation density, texture coefficient, stacking fault probability, microstrain, and crystal phase transition (α, β, γ, and δ phase). These effects result from the preferential orientation of the crystals and lead to changes of crystal structure, which affect the band structure of the V_2O_5 material.[76,102,150]

The phase transition is a factor that strongly affects the band structure of V_2O_5 and includes crystal phase transitions (α, β, γ, and δ phase), chemical phase transitions (from V^{2+} to V^{5+}), and band structure transitions (MIT, SMT). The band gap of β-V_2O_5 is smaller than that of α-V_2O_5, and the split-off conduction band is wider for β-V_2O_5 than α-V_2O_5.[151,152] Absorption measurements revealed that the band gap of V_2O_5 thin films was reduced from 2.68 to 2.36 eV due to the phase transition from α-V_2O_5 to β-V_2O_5.[153] The mixing of α and β phase V_2O_5 can result in wide absorption and a shift toward a longer wavelength.[91] E_g decreased from 2.44 to 2.34 eV due to the change from V_2O_5 to V_4O_9,[154] while two absorption peaks were observed due to both inter-band and intra-band photo transitions in VO_2 and V_4O_9. As a result, the values of E_g obtained with the film were 3.10 eV and 1.50 eV.[155]

Recently, some reports illustrated the MIT and SMT in V_2O_5. These transitions led to reduced band edges at 1.70 eV,[112] 1.10 eV,[113] 1.50 eV, and 0.75 eV.[71] The SMT and MIT appear due to the electrons being excited across the gap and entropy.[112] The band reduced to 1.10 eV due to the formation of an isolated surface defect and electron-electron-phonon interaction when the sample was heated to high temperature.[71,112,113]

1.4.2 Photoluminescence

Photoluminescence is re-emission that results from the annihilation of electron-hole pairs due to electron-hole recombination after the absorption of a photon.[97] In V_2O_5 material, photoluminescence (PL) includes phosphorescence and fluorescence, which have values related to the V=O double bond vibration state. When light illuminates a V=O double bond on the surface, an electron is transferred from oxygen to vanadium ions, forms excited singlet and triplet states, and recombines with the ground hole states. This process of fluorescence and phosphorescence is shown in Eq. (1.7).[156–158]

$$[V^{5+} = O^{2-}]_{S_o} \xrightarrow{h\nu} [V^{4+} - O^{-}]_{S_1} \rightarrow [V^{4+} - O^{-}]_{T_1} \xrightarrow{RH} [V^{5+} = O^{2-}]_{S_o} + R \qquad (1.7)$$

S_0 is the ground state, S_1 is the singlet state, T_1 is the triplet excited state, and R can be photon or phonon emission.

Fig. 1.12 shows the PL emission excited by 250 nm and 330 nm light sources. Electrons excited from singlet states S_1 and S_2 quickly relax to triplet state T_1 due to unstable photoactivated species of S_1 and S_2 states. This relaxation process involves the loss of energy from electrons due to collisions and scattering in materials resulting in phonon emission. At

room temperature or higher, this process is much more active than at low temperature. Therefore, both the phosphorescence and fluorescence decrease with increasing degassing temperature. When the temperature decreases from 300 to 77 K, the phosphorescence increases while the fluorescence hardly changes.[158] At room temperature, the PL disappears or is very weak.[158]

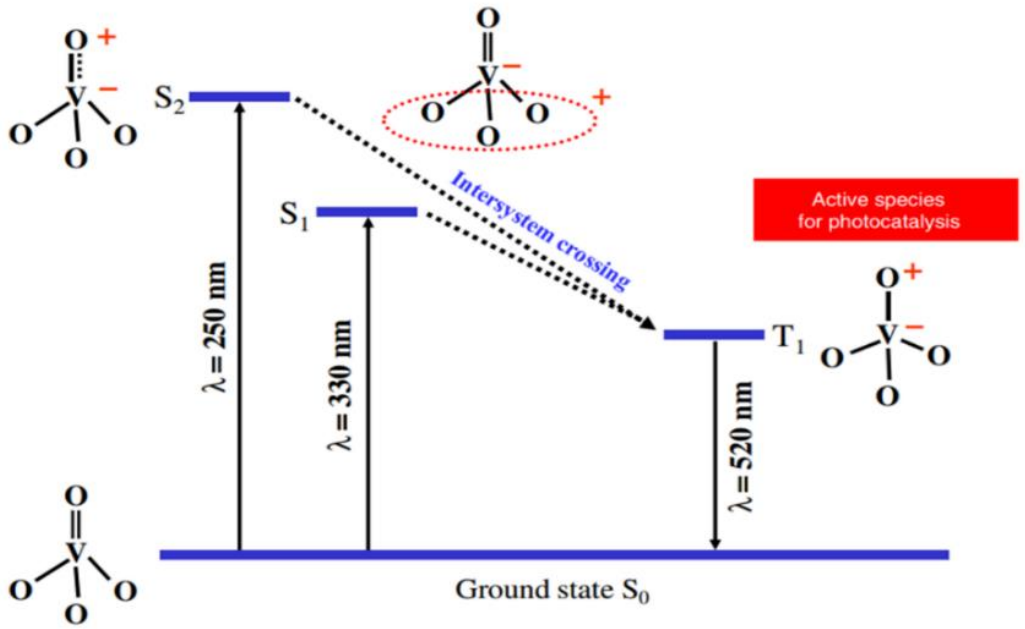

Figure 1.12. Energy diagram of alumina-supported orthovanadate-like (V=O)O3 species.[157]

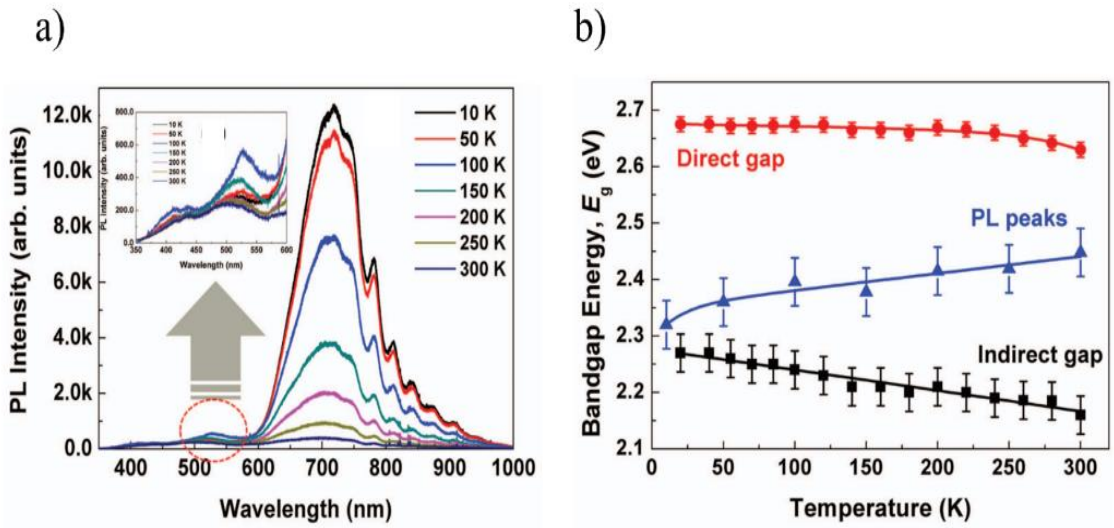

Figure 1.13. (a) Effect of temperature measurement on PL intensity, (b) PL peak and interband transition of V_2O_5 nanorod film.[99]

Table 1.2. Photoluminescence of the morphologies and synthesis methods of V_2O_5 micro-nanostructures.

Morphology	Method	Excitation source	Peak position (nm)	Ref
Bulk powder	Commercial	365 nm	375	[126]
Nanocluster (film): 100 – 200 nm Nanospheres: 200 – 500 nm diameter Nanowires: 200 nm diameter, 10 µm length	CVD	325 nm	391 385 391, 620, 688	[61]
Nanoparticles: 16 nm diameter	WRC	420 nm 560 nm	458 588	[129]
Micro-nanobelts: 250 – 400 nm diameter and 25 – 30 µm length	VPD	< 400 nm	417	[165]
Nanoparticles 15 – 20 nm diameter	WCR	475 nm	502	[128]
V_2O_5/Al_2O_3	WCR	250 nm	520	[157]
Nanoparticles: 20 nm diameter	CVD	325 nm	543	[68]
Nanosheets: graphene-like 2D sheets	Light-assisted WCR	275 nm	545	[166]
Nanobelts: 30-200 nm width, ultralong	Melting + hydrothermal	514 nm	661.2	[167]
Nanorods: 1 µm diameter, 2 – 3 µm length	WCR	327 nm	418, 453	[168]

Nanoparticles: 5 – 8 nm diameter	WCR	380 nm	460, 593	[108]
Thin films	E-Beam	330 nm	485, 526	[122]
Nanorods: 200 nm diameter, 3 μm length	E-Beam	325 nm	530, 710	[72]
Nanorods: 50 – 70nm diameter, 2 – 5 μm length	Household microwave	320 nm	385, 410, 552	[169]
Nanospheres: 284 nm diameter	WCR	325 nm	396, 530, 710	[164]
Nanowires: 100 nm diameter, more than 10 μm length	TE	325 nm	400, 560, 710	[170]
Nanorods: 80 – 100 nm diameter, 500 nm length	CSP	325 nm	410, 534, 692	[147]
Thin films (V_2O_5/ITO)	E-Beam	330 nm	485, 510, 528	[150]
Thin films (V_2O_5/FTO)	Electro-deposition	325 nm	426, 531,700	[91]
Rods/slices: rod: 1 μm diameter, 10 μm length, slice: about micrometer	Electro-deposition	325 nm	426, 526, 598, 695	[91]
Thin films: as-grown	Sputtering	325 nm	480, 525, 563, 695	[171]
Nanoparticles: 96.5 nm diameter	Sol-gel	325 nm	382, 397, 450, 469, 530, 557	[109]
Thin films: after 10 pulses	Sputtering	325 nm	408, 448, 527, 582, 708	[171]

Nanowires: 50 nm diameter, 10 μm length	CVD	266 nm	~300 – 580, 600 – 750	[69]
Nanowires: 50-100 diameter, several ten micrometer length	CVD	365 nm	~350 – 700	[126]
Nanobelts: ~100 nm diameter, μm length	PVD	325 nm	~450 – 725	[172]
Nanorods: β-V_2O_5, ~μm length	Sputtering	325 nm	~450 – 750	[161]
Nanoparticles: 250 nm diameter	Solvent-catalyst	Light source	~470 – 640	[173]
V_2O_5-PVAc fibers	WCR	514.5 nm	~520 – 775	[174]
Nanorods: 30 – 40 nm diameter	Hydrothermal	Xenon lamp	~540 – 830	[175]
Nanowires: 10 – 20 nm diameter, μm length	Hydrothermal	Xenon lamp	~540 – 830	[175]
Nanoribbons: 100 – 300 nm diameter, μm length.	Heating foil	475 nm	~550 – 750	[140]
Nanorods: 200 nm diameter and 1 μm length.	TOA	514 nm	~550 – 850	[160]
Nanorods: 100 nm diameter and 2 μm length.	TOA	514 nm	~550 – 800	[159]
Bulk powder	Commercial	514.5 nm	~540 – 840	[176]

The PL intensity of V_2O_5 thin film is very weak at room temperature (300 K)[69,72,99,158] which is a challenge in analyzing the luminescence of V_2O_5. Therefore, the solution to investigate the luminescence with regular PL measurements of V_2O_5 is usually to do it at low temperature or to use the cathode luminescence (CL) method.[74] Fig. 1.13a shows that the PL intensity of V_2O_5 is strongly enhanced when the measurement temperature decreases from 300 K to 10 K. The PL peak centered at 710 nm becomes approximately 25 times more intense, but low-temperature measurement leads to a peak shift, which may be due to a reduction in emissions caused by crystal defects such as vacancies and disorders. Fig. 1.13b shows that the peak position shifts to low energy from 2.45 to 2.32 eV with decreasing temperature from 300 to 10 K.[99]

Recently, various V_2O_5 micro-nanostructures have been grown to enhance the PL intensity, such as micro-nanorods, micro-nanowires, and hybrid nanostructures such as V_2O_5/ZnO nanorods.[159–161] Studies have reported the improvement of the visible PL due to the contribution of excess electrons from defects and transfers from ZnO to V_2O_5. The vanadium atoms near the defects receive excess electrons from the crystal due to the removed oxygen atoms.[86,118,162] These electrons can fill a part of the conduction band or the split-off band.[118] The absorption is enhanced due to the formation of large amounts of V^{3+} and V^{4+} oxidation states during annealing and growth, which may also cause the enhanced PL intensity.[163,164]

V_2O_5 has four kinds of transition absorption, and its band edge absorption is very wide (from 0.75 to 3.49 eV). Reports also show a wide, broad range of PL for V_2O_5 micro-nanostructures of 0.73 to 3.3 eV. However, the PL peak position, the number of peaks, and the broad emission of V_2O_5 micro-nanostructures are not the same. Table (1.2) shows that the PL spectra may appear as one to six peaks or a wide range emission. The main reason for the different peak positions and number of peaks has not been explained.

Le *et al.*[164] reported on the high-intensity PL of V_2O_5 nanospheres due to the presence of a high concentration of the V^{4+} state with three peaks. Another PL peak centered at 710 nm (1.74 eV) is attributed to mid-gap states (1.84 eV) formed by oxygen defects. Three peaks at 400 nm (3.10 eV), 560 nm (2.21 eV), and 710 nm (1.75 eV) are also shown in V_2O_5 nanowires.[170]

Abd-Alghafour *et al.*[147] investigated the effect of the annealing temperature on the optical properties of V_2O_5 nanorods. The annealing temperature affects the PL intensity, while the peak positions are similar with three peaks at 410 nm (3.10 eV), 534 nm (2.31 eV), and 692 nm (1.79

eV). Wang *et al.*[118] studied the form of mid-gap defect states at 0.75 eV below the CB due to thermal reduction and electrochemical reduction (lithium insertion). The PL appears in broad emission ranges of 1000 to 1500 nm (electrochemical reduction case) and 1100 to 1700 nm (thermal reduction case) due to the transition between CB and midgap defect states. Other reports show very wide ranges of broad emission of 350 to 700 nm (nanowires),[126] 450 to 725 nm (nanobelts),[172] 540 to 830 nm (nanorods),[175] and 550 to 850 nm (nanorods).[160]

Fig. 1.14a shows that oxygen vacancies also appear in a broad emission range of 1.60 to 3.3 eV, while the nominally undoped V_2O_5 shows broad emission from 1.90 to 2.50 eV. Fig. 1.14b demonstrates that the PL peak at high energy increases with the concentration of oxygen vacancies. The oxygen vacancies due to the reduced V_2O_5 can create electrons, as shown in Eq. (1.8).[148] These excess electrons fill the split-off states and shift the Fermi level to a higher energy state.[118] This leads to shifting of the ultraviolet absorption and enhances the ultraviolet PL intensity.[118,164]

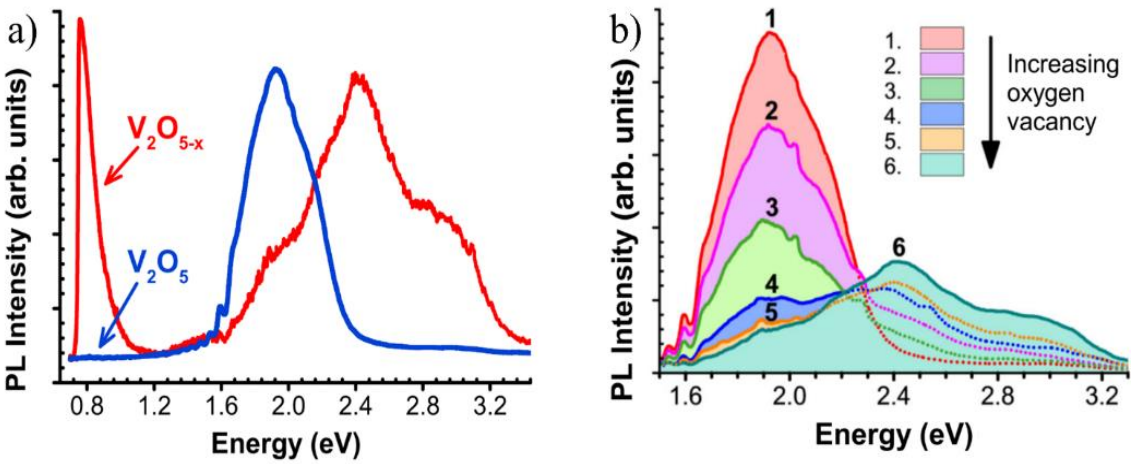

Figure 1.14. (a) The PL of V_2O_{5-x} and V_2O_5, (b) shift in the band-edge PL emission with increasing oxygen-vacancy concentration.[118]

Othonos *et al.*[69] and Kang *et al.*[72] investigated the strong PL intensity at shorter wavelengths and the decrease at longer wavelengths due to the enhanced oxygen vacancies during laser irradiation. Oxygen vacancies were created due to decomposed water or increasing lattice temperature during laser irradiation. This leads to the formation of various energy states in CB due to the increasing number of carriers or the creation of a new oxidation state (a mixture of V^{3+}, V^{4+}, and V^{5+}). Consequently, more PL peaks appear at higher energy.[69,72]

$$V_2O_5 \rightleftarrows V_2O_{5-x} + \left(\frac{x}{2}\right) O_2 + (x)O_V^{2+} + (2x)e^- \qquad (1.8)$$

The PL intensity of the peak at ~690 nm slightly decreases and becomes static after initial exposure for 45 min, while a PL peak appears at ~450 nm, and the intensity is strongly enhanced.[69] The PL of colored film (10 pulses) shows two more peaks at 408 nm and 448 nm compared with as-grown film.[72] The absorption shows that the band edge of V_2O_5 film increases due to irradiation.[177] The visible emission (540 – 840 nm) can be quenched by the irradiation (from 0 to 60 min) due to increasing temperature and photochromism.[176]

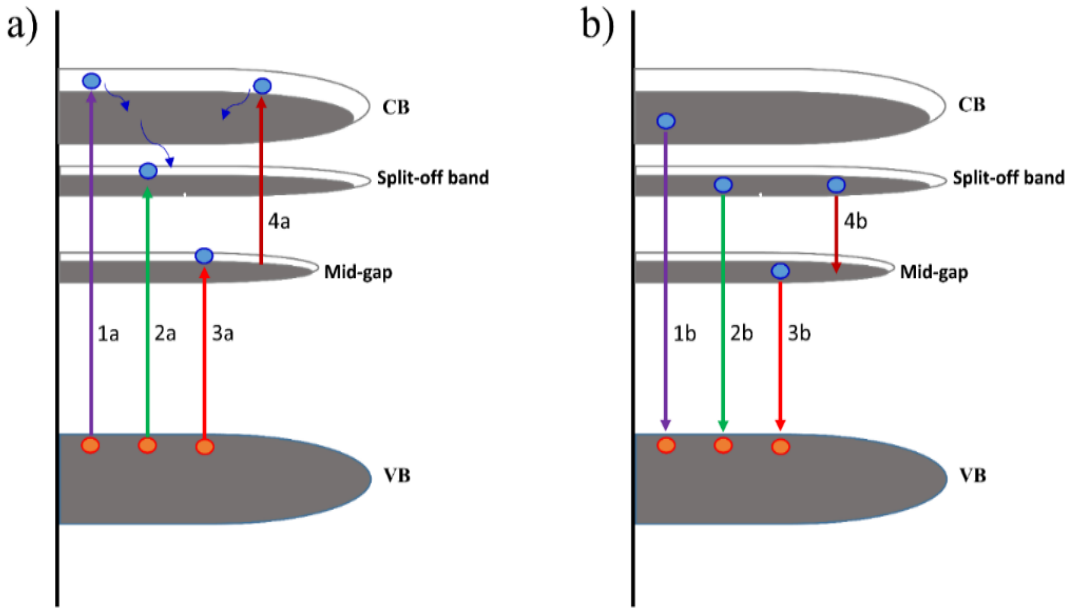

Figure 1.15. Diagram of different transitions that can appear in V_2O_5 nanostructure. (a) Absorption transition, (b) Recombination transition.

Similar to the absorption spectrum with four kinds of transitions, V_2O_5 micro-nanostructures also have four kinds of transition recombination, as shown in Fig. 1.15b: (1) transition from the V*3d* states of CB to VB, (2) transition from the V*3d* split-off states of CB to VB, (3) transition from mid-gap states to VB, and (4) transition from CB to mid-gap states. These transitions can occur individually or simultaneously. However, electrons can relax from a higher band to a lower band or can relax from higher states to lower states into a partial band before recombining with VB. These relaxations occur primarily on a femtosecond time scale via the emission of optical phonons with inelastic and elastic scattering.[178] The electrons and holes relax until they can emit a photon or recombine non-radiatively.[97] This may lead to different peak positions and numbers of peaks.

The PL peak positions and broad emission of V_2O_5 are also affected by the morphology of structures, synthesis methods, vacancies in the structure, and excitation source (Table (1.2)). Most reports indicate the PL of V_2O_5 is from 1.70 to 3.10 eV, which correspond to wavelengths of about 730 to 400 nm. Diaz-Guerra *et al.*[74] studied the cathode luminescence (CL) with three kinds of morphologies. The untreated powder shows one peak at 1.70 eV, and nanorods show two peaks at 1.70 eV and 3.10 – 3.30 eV, while nanotips show two peaks at 2.20 eV and 3.30 eV with wide, broad emission from 1.70 to 3.30 eV.

Similarly, the PL properties are also affected by the morphologies of V_2O_5 nanostructures synthesized by CVD. Nanoclusters and nanospheres show one peak at 391 nm and 385 nm, respectively, while the PL of nanowires shows three peaks at 391, 620, and 688 nm. The PL center peak position of the band edge shifts from 1.95 to 2.45 eV due to the increase of oxygen vacancies (Fig. 1.14b)[118] and from 2.29 to 2.35 eV due to the change from amorphous to crystal structure.[122]

1.4.3 Photo-degradation

Photo-degradation is an important application of the optical properties of V_2O_5. The form of the band structure including V*3d* of the CB, V*3d* split-off band, and mid-gap states lead to V_2O_5 having suitable photocatalytic activity for use with sunlight or visible light.[21,127] In water splitting, high efficiency is achieved when the bottom level of the CB of the semiconductor is more negative than that of the redox potential of a normal H^+/H_2 hydrogen electrode (eV vs. NHE). The top level of the VB should be more positive than that of the redox potential of O_2/H_2O.[179–181]

Compared with other metal oxides (such as TiO_2, $SrTiO_3$, and ZnO), V_2O_5 micro-nanostructures have low performance due to the bottom level of the CB being less negative than that of with H^+/H_2.[182] The lowest CB of V_2O_5 lies at about 5.0 – 5.2 eV (vacuum level),[183,184] while the negative potential of the redox potential of H^+/H_2 (eV vs. NHE) is about 4.5 eV (vacuum level).[180,185] The VB and CB potentials of V_2O_5 at the point of zero charge can be calculated using Eq. (1.9) and Eq. (1.10).[186,187]

$$E_{VB} = X - E^e + 0.5E_g \qquad (1.9)$$

$$E_{CB} = E_{VB} - E_g \qquad (1.10)$$

where E_{VB} is the VB edge potential, X is the electronegativity of V_2O_5 (about 6.10 eV),[188] E^e is the energy of free electrons on the hydrogen (about 4.50 eV), E_g is the band edge of materials, and E_{CB} is the CB edge potential. The band edge absorption of V_2O_5 is about 2.00 – 2.70 eV. Therefore, E_{VB} is about 2.60 – 3.00 (eV vs. NHE), and E_{CB} is about 0.60 – 0.20 (eV vs. NHE). The electrons at the bottom CB are not able to reduce oxygen molecules (O_2), while holes are able to produce $HO^{\bullet}$. However, the presence of V^{4+} due to the surface defects during the growth process plays a vital role in the generation of $O_2^{\bullet-}$ radicals.[21]

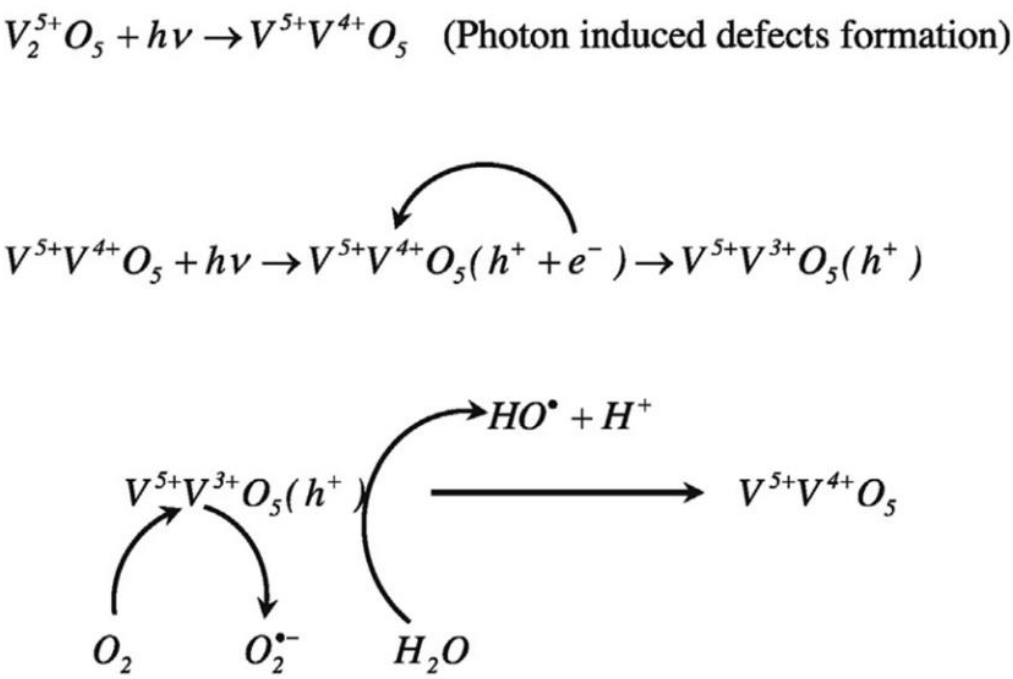

Figure 1.16. Diagram of the process of formation of surface traps and the transfer of electrons for the generation of $O_2^{\bullet-}$ radicals under illumination.[21]

Fig. 1.16 shows a diagram of the formation process of surface traps and the transfer of electrons for the generation of $O_2^{\bullet-}$ radicals under illumination.[21] Electrons excited at V*3d* states due to absorption from VB and mid-gap states ("1a" and "4a" in Fig. 1.15a) can participate in the reduction reaction. Some reports show that the transition at about 385 – 410 nm (3.20 – 3.00 eV)[61,170,171] correspond to V_{CB} = 0.00 – 0.10 (eV vs. NHE). This shows that electrons in the CB of V_2O_5 can react to produce $O_2^{\bullet-}$.

In order to improve the photocatalytic performance, morphologies such as nanowires, nanobelts, nanoparticles, 2D nanosheets, porous V_2O_5, and nanohollows have been fabricated to increase the surface area and defect states.[21,114,127,137,190,191] However, the

photocatalytic efficiency of pure V_2O_5 is still low. The width of the band gap, amount of charge separation, mobility, and surface area are factors that play important roles in the photocatalytic activity. Hetero-nanostructures between V_2O_5 and other nanomaterials have received great attention due to the great enhancement in the catalytic performance of V_2O_5. Examples of such nanomaterials include Au/V_2O_5/ZnO,[192] $Ag_2O/V_2O_5/TiO_2$,[189] Bi/$BiVO_4/V_2O_5$,[193] SnO_2/V_2O_5,[194,195] V_2O_5/TiO_2,[196,197] graphene nanosheets/V_2O_5/TiO_2,[198] and carbon nanostructures/V_2O_5.[199]

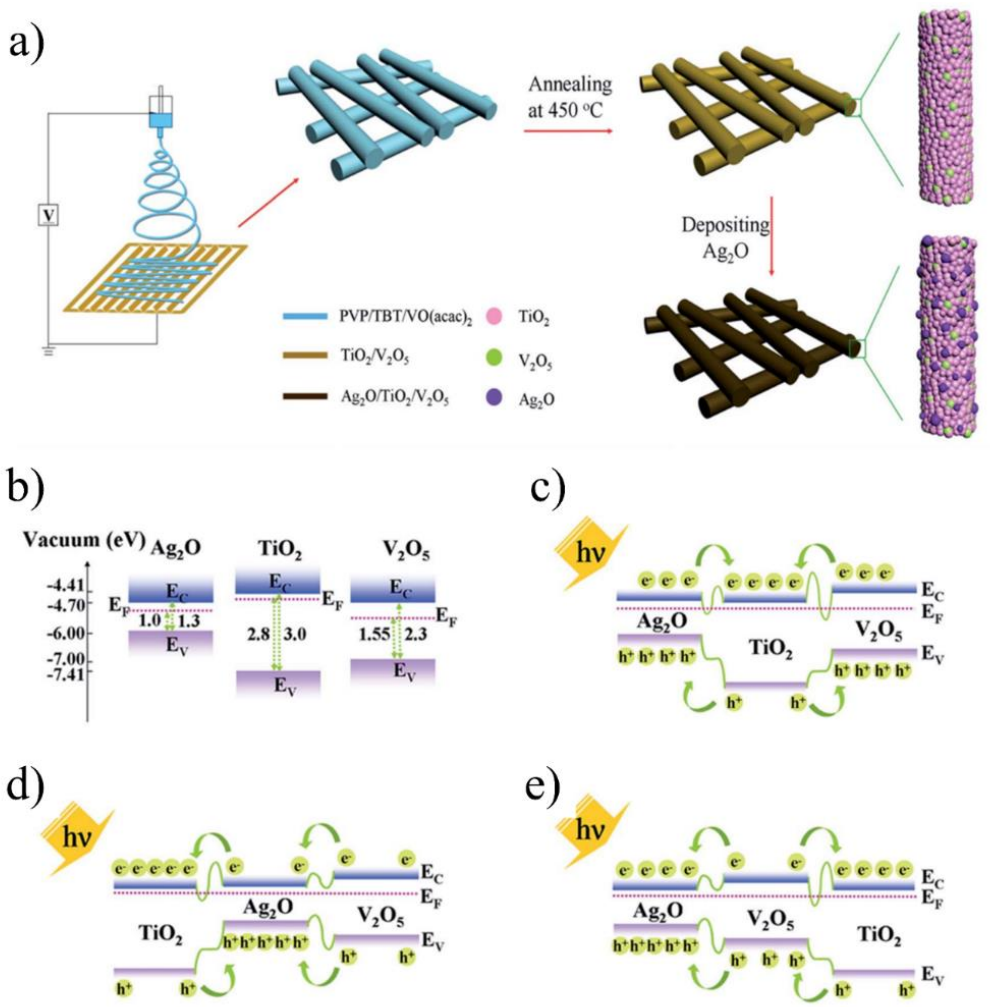

Figure 1.17. (a) Diagram of fabrication process of hetero-structures, (b) Band structure of three kinds of hetero-structures, diagram of energy band matching, and proposed mechanisms of charge carrier transition of (c) $Ag_2O/TiO_2/V_2O_5$, (d) $TiO_2/Ag_2O/V_2O_5$, and (e) $Ag_2O/V_2O_5/TiO_2$.[189]

In hetero-structures, electron-hole pairs can transfer between materials, slow down recombination, and prolong the lifetime of the electron-hole pairs. This leads to improved electron-hole separation, increased photocurrent, and enhanced photocatalytic

activity. Table. (1.3) shows a comparison of the photocatalytic performance of V_2O_5 for different morphologies, synthesis methods, and hetero-structures.

Fig. 1.17a and b show the fabrication process and band structure of three kinds of hetero-structures that were derived from the interface between V_2O_5, Ag_2O, and TiO_2.[189] In these hetero-structures, electrons at the CB of Ag_2O and V_2O_5 transfer to TiO_2 (Fig. 1.17c), electrons transfer from V_2O_5 to Ag_2O, and then electrons on Ag_2O transfer to TiO_2 (Fig. 1.17d). Electrons on TiO_2 transfer to V_2O_5, and then electrons on V_2O_5 transfer to AgO_2 (Fig. 1.17e).

Table 1.3. Photocatalytic performance of V_2O_5 nanostructures and V_2O_5/OMs hetero-structures.

Sample	Method	Irradiation source, time, and dye solution	Performance (%)	Ref
V_2O_5 precursor	Hydrothermal	Visible light, 210 min, Methyl Blue	<10	[127]
V_2O_5 nanowires			28	
V_2O_5 nanorods			31	
V_2O_5 commercial	Solvothermal	Visible light, 7h, 1,2-dichlobenzene	45	[137]
V_2O_5 solids			34	
V_2O_5 nanohollows			18	
V_2O_5 nanorods	Hydrothermal	Visible light, 300 min, Rhodamine-6G	85	[114]
		Visible light, 300 min, Methyl Orange	48	
		Visible light, 300 min, Methyl Blue	24	

V_2O_5 bulk	Hydrothermal+ WCR	UV light, 120 min, Toluidine blue O	~90	[194]
V_2O_5 nanowires		UV light, 75 min, Toluidine blue O		
SnO_2/V_2O_5 nanowires		UV light, 45 min, Toluidine blue O		
V_2O_5 nanorods	Hydrothermal	Mercury lamp, 210 min, Methyl Blue	<10	[200]
V_2O_5/RGO nanocomposites		Mercury lamp, 255 min, Methyl Blue	~85	
		Visible light, 390 min, Methyl Blue	~75	
		UV light, 210 min, Methyl Blue	~62	
V_2O_5 nanorods	Hydrothermal	Visible light, 300 min, Methyl Blue	~27	[191]
Graphen-V_2O_5		UV light, 240 min, Methyl Blue	~100	
		Visible light, 150 min, Methyl Blue	~100	
		Sunlight, 90 min, Methyl Blue	~100	
V_2O_5 nanorods	Hydrothermal	Sunlight, 95 min, AO dye	~40	[198]
V_2O_5/TiO_2		Sunlight, 60 min, AO dye	~95	
GNS-V_2O_5/TiO_2		Sunlight, 20 min, AO dye	~100	

Fig. 1.18 shows the role of V_2O_5 in a hetero-structure to improve the photocatalytic performance under UV-vis and visible light irradiation.[197] Under UV-vis light irradiation, pure V_2O_5 and P25 (commercial TiO_2 nanoparticles) exhibit low

photocatalytic efficiencies of 27.8% and 74.3%, respectively. However, the photocatalytic efficiency was enhanced by the formation of $TiO_2@V_2O_5$ core-shell hollow porous microspheres (HPMs). Under visible light irradiation, P25 and TiO_2 HPMs have almost no photocatalytic activity due to the wide band gap of TiO_2 (3.20 eV), and the pure V_2O_5 nanoparticles exhibit about 31.8% efficiency.

The photo-degradation activity was markedly improved in the $TiO_2@V_2O_5$ core-shell HPMs structure. Under both UV-vis and visible light irradiation, the V_2O_5 extends and enhances the light absorption. Therefore, the hetero-structure of $TiO_2@V_2O_5$ exhibits higher photocatalytic performance than pure TiO_2 or pure V_2O_5. Moreover, the absorption band around 600 – 713 nm[196] or 770 nm[201] due to the presence of V^{4+} in a hybrid structure improves the performance of visible light photocatalysis. Rakkesh *et al.*[198] reported on the photo-degradation under sunlight irradiation. Compared with pure V_2O_5 nanorods and V_2O_5/TiO_2 core/shell structures, the GNS-V_2O_5/TiO_2 exhibits better conductivity because the electrons from metal oxides quickly transfer to co-catalysts (GNS) and enhance the photocatalytic performance with pure V_2O_5 (40% for 60 min), V_2O_5-TiO_2 (95% for 60 min), and GNS-V_2O_5/TiO_2 (100% for 20 min).

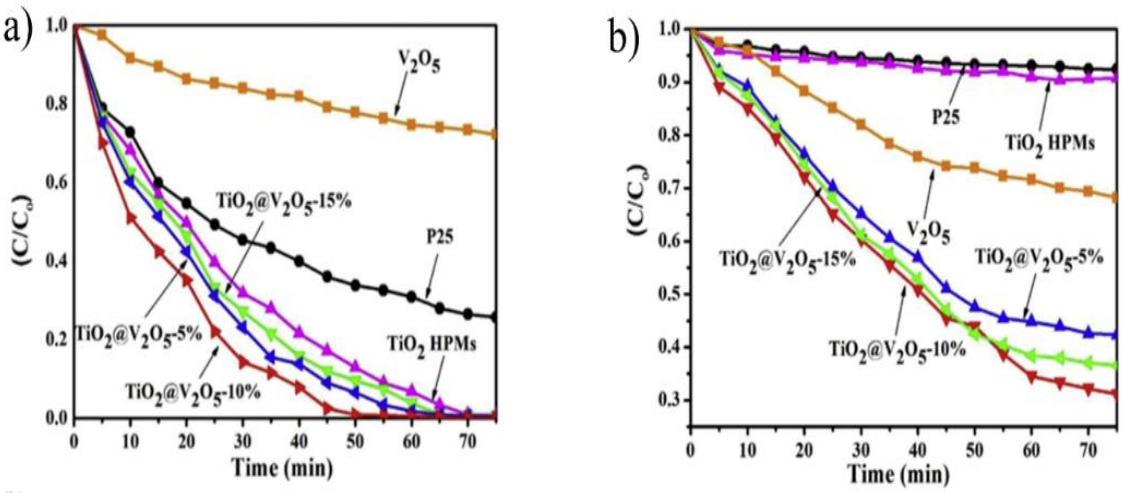

Figure 1.18. The photocatalytic performance of P25, pure TiO_2 HPMs, and $TiO_2@V_2O_5$ core/shell HPMs under (a) UV-vis light irradiation and (b) visible light irradiation.[197]

Chapter 2. Experimental Section

2.1 Synthesis of V_2O_5 micro-nanostructures

This research reports on various V_2O_5 micro-nanostructures with different morphologies prepared by different methods. Six types of micro-nanostructures, thin film (TFs), nanoparticles (NPs), nanorods (NRs), nanowires (NWs), nanospheres (NSs), nanohollows (NHs), and RGO/V_2O_5 micro-nanocomposites, are fabricated by the electrodeposition, the hydrothermal,[30,202] and the wet chemical reaction[46] methods.

2.1.1 V_2O_5 thin films

The V_2O_5 micro-nano thin films were prepared by an electrodeposition method using a fluorine-doped tin oxide (FTO) substrate as a cathode. The electrolyte for the electrodeposition was formed by dissolving 0.234 g of NH_4VO_3 in 150 mL of H_2O and stirring it at room temperature for 2 h. This solution was transferred to a bath and kept at a constant temperature of 60 ℃ during electrodeposition. Prior to electrodeposition, the FTO substrate was sequentially cleaned by ultra-sonication in ethanol and deionized water. Then for the electrodeposition, FTO substrate was immersed into the bath with a distance between the two electrodes kept at 10 cm. The deposition current density was kept constant at 0.5 mA/cm^2 during the growth period of 90 min. After the completion of the growth process, the sample was dried in air at 50 ℃ for 2 h and annealed at different temperatures in air for 2 h.

2.1.2 V_2O_5 nanoparticles and nanorods

The V_2O_5 NPs and NRs were synthesized by hydrothermal method. First, 0.45 g of V_2O_5 powder (99.99%, Sigma-Aldrich) was dissolved in 25 mL distilled water, and the solution was stirred for 1 h. Then, 2.5 mL hydrogen peroxide (H_2O_2: 30 wt%, Wako, Japan) was slowly dropped into this solution under stirring, and the solution was continuously stirred for 24 h to obtain dark yellow gel. Subsequently, 3 mL hydrazine ($N_2H_4 \cdot H_2O$, Sigma-Aldrich) was added to the resulting gel solution and stirred for 1 h. This solution was then transferred to a 50- mL autoclave and kept in an oven at 205 ℃ for 6 h. The resulting precursor was washed with anhydrous ethanol and distilled water several times. The precursor was then dispersed in distilled water and spin-coated onto

a quartz substrate at a speed of 3000 rpm for 1 minute. Annealing conditions for the precursor determined the final nanostructure: V_2O_5 NPs were obtained by annealing at 350 ℃ for 2 h in air; V_2O_5 NRs were obtained by annealing at 500 ℃ for 2 h in air.

2.1.3 V_2O_5 micro-nanowires

V_2O_5 NWs were fabricated in a similar manner with synthesis nanoparticles and nanorods. Under continuous magnetic stirring, 0.364 g V_2O_5 powder and 20 mL H_2O were mixed at room temperature, and then 4 mL 30% H_2O_2 was slowly dropped into this solution. Stirring was continued for 1 h, after which a light orange solution was obtained. The resultant solution was transferred to a 50-mL autoclave and kept in an oven at 205 ℃ for 48 h. The product was washed with anhydrous ethanol and distilled water several times. Finally, the product was drop coated onto a quartz substrate and then dried at 80 ℃ for 6 h in vacuum.

2.1.4 V_2O_5 micro-nanospheres

V_2O_5 NSs were fabricated by chemical reaction method. First, 0.234 g NH_4VO_3 (99.99 %, Sigma-Aldrich) was dissolved in 60 mL distilled water, and the solution was stirred for 1 h. Then, 1 mL of 1 M HCl (Sigma-Aldrich) solution was added drop-wise to the solution and stirred for 30 min before 3 mL hydrazine $N_2H_4 \cdot H_2O$ was added, and the solution was stirred for another 10 min at room temperature. The product, $V(OH)_2NH_2$ NSs, was filtered, washed several times with distilled water, and then dried at 80 ℃ for 6 h. The precursor was then dispersed in deionized water and was spin (or drop) coated onto a quartz substrate. Finally, to obtain V_2O_5 NSs, the coated precursor was calcined in a tubular furnace at 350 ℃ in ambient air for 2 h.

2.1.5 V_2O_5 nanohollows

The V_2O_5 nanohollows (NHs) were fabricated by the hydrothermal treatment of $V(OH)_2NH_2$ nanospheres, which were fabricated by a wet chemical reaction method.[46,164] First, 0.234 g of NH_4VO_3 (99.99 %, Sigma-Aldrich) was dissolved in 60 mL of distilled water, and the solution was stirred for 1 h. Then, 1 mL of 1 M HCl solution (Sigma-Aldrich) was added drop-wise to the solution and stirred for 1 h before 3 mL of hydrazine $N_2H_4 \cdot H_2O$ was added. The solution was stirred for 15 minutes at room temperature.

To obtain the NHs, the solution containing $V(OH)_2NH_2$ NSs was transferred to a 120-mL autoclave and kept in an oven at 120 ℃ for 6 h. The precursors of the $V(OH)_2NH_2$ NSs and VOOH NHs were filtered and washed several times with distilled water. The VOOH NHs products were dried in a vacuum at 80 ℃ for 6 h. Finally, to obtain the V_2O_5 nanostructures, the products were calcined in a tubular furnace at 350 ℃ in ambient air for 2 h.

2.2 Synthesis RGO and V_2O_5/RGO nanocomposites

Graphene oxide (GO) was synthesized from expanded graphite by the modified Hummers method.[203] First, 500 mL of H_2SO_4 was added to expanded graphite (5 g) under stirring. The mixture was cooled down to 0 ℃ by keeping it in an ice bath. Next, 30 g of $KMnO_4$ was slowly added to keep the reaction temperature below 20 ℃, and then the reaction was warmed to 35 ℃ and stirred for 2 h. At that time, 2 L of distilled water was added slowly, and then 50 ml of H_2O_2 (30%wt) was added. The color of the suspension changed from dark to yellow with bubbles. The suspension was washed with 5 L of 10 % HCl and distilled water several times until the GO dispersion reached pH 6.

RGO was prepared by reduction of the GO solution (1 mg/10 mL). First, 10 mg GO was ultra-sonicated for 1 h, and then ascorbic acid (AA) was added to the solution (GO:AA with 1:1) and stirred at 60 ℃ for 2 h. This solution was transferred to a 120-mL autoclave and kept at 120 ℃ for 6 h. The RGO product was washed several times with distilled water and dried in a vacuum at room temperature.

The V_2O_5/RGO nanocomposites were prepared by solution mixing. First, 10 mg of V_2O_5 nanostructures were suspended in 10 mL of distilled water and sonicated for 15 min, and then 5 mg of RGO was suspended in 10 mL of distilled water and sonicated for 2 h. Both of the solutions were mixed and stirred at room temperature for 2 h.

2.3 Characterization methods

The morphology of the V_2O_5 micro-nanostructures was investigated by high-resolution scanning electron microscopy (HR FE-SEM, MIRA LMH, TESCAN, Czech) and transmission electron microscopy (TEM, H-8100, Hitachi, Japan). The crystal structure of the nanostructures was characterized using an X-ray diffractometer (XRD, DMax 2000, Rigaku, Japan) with Cu $K\alpha$ radiation at a wavelength of 1.54 Å, as well as

a Raman/PL spectrometer (Horiba Jobin-Yvon, LabRAM HR, Japan), which was equipped with a He-Ar laser with a wavelength of 514.5 nm and a maximum power of 200 mW. X-ray photoelectron spectroscopy (XPS) measurements were performed to investigate the composition and V^{4+} oxidation states of the V_2O_5 nanostructures. The XPS spectra of the micro-nanostructures were recorded with a system equipped with a 300-W Mg $K\alpha$ source (Thermo-Scientific MultiLab, ESCA). The absorption spectra were measured using a UV-vis spectrophotometer (SolidSpec-3700, Shimadzu, Japan) in the wavelength range of 330 − 900 nm. PL measurements were performed at room temperature using a Raman/PL spectrometer equipped with a He-Cd laser with a wavelength of 325 nm and a maximum power of 200 mW.

2.4 Photocatalytic measurements

Photocatalytic activity measurements were carried out using a UV-vis spectrophotometer (HP8453) and Xe-lamp irradiation. First, 5 mg of material was dispersed in distilled water, dropped on a quartz substrate, and dried at 200 ℃ for 1 h. The samples were then immersed in a 30-mL solution of 15 μM methylene blue (MB, 98%, Samchun chemical, Korea) and stirred in a dark room for 45 min for the adsorption-desorption of the dye molecules before carrying out photo-catalysis.

Chapter 3. Optical Characterization of α-V_2O_5 and Mixed α-β V_2O_5 Phase Films

3.1 Motivation

The metastable β-V_2O_5 phase and a mixture of α-β phase V_2O_5 can be obtained from the transition of α-V_2O_5 at high temperature or high pressure.[76,80–82] The phase transition of the V_2O_5 structure is also affected by the substrate, film thickness, and synthesis method.[73,76,83,84] The process and mechanism of the α-β phase transition in V_2O_5 have been demonstrated. However, the influence of the phase transition on the PL properties has not been investigated.

Some reports show the effect of growth conditions on the optical band gap of α-V_2O_5. An increased optical band gap from 1.95 eV to 2.45 eV and multiple PL peaks were observed due to the presence of vacancy defects.[118,171] The edge absorbance shifts to lower energy due to the growth process at different temperatures,[146,204] and intercalated lithium.[118,119] The PL intensity of the V_2O_5 nanostructure strongly depends on the synthesis method, crystal structure, and magnetic field treatment.[159–161,174]

In the present study, I report on V_2O_5 micro-nanostructure with different surface morphologies prepared by electrodeposition method using constant applied current. And the effect of annealing temperature to surface morphology, crystal structure, mixed α-β phase V_2O_5 structure, optical, and room-temperature PL properties were investigated and discussed.

3.2 Results and discussion

Fig. 3.1 shows FE-SEM images of the morphologies of the FTO substrate and V_2O_5 films annealed at different temperatures. The as-deposited V_2O_5 film shows a smooth surface due to the amorphous V_2O_5 film. The rod-like structure was observed when annealed at 400 ℃, and the film begins to transform into a nano-rod array at 450 ℃. The nano-rod structure with length ~1μm and diameter ~ 200 nm clearly appears when the sample is annealed at 500 ℃. When annealed at a higher temperature of 550 ℃, the rod-like structure of the V_2O_5 tends to increase in length about ~1 - 4 μm with diameter about 200 - 500 nm due to the high diffusion rate in

the surface of the film and become mixed phases of α-V_2O_5 and β-V_2O_5 with micro-nano plates.[83]

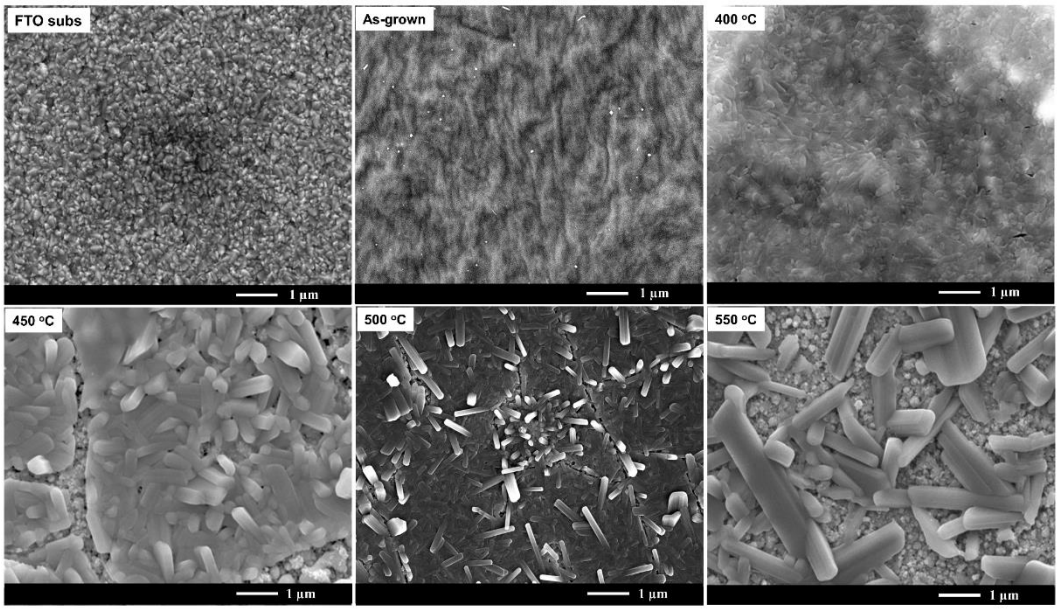

Figure 3.1. SEM images of V_2O_5 thin films annealed at different temperatures.

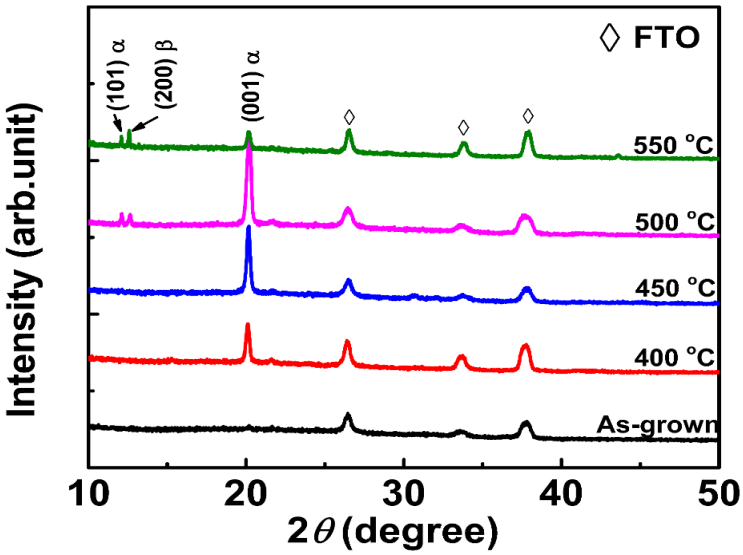

Figure 3.2. XRD patterns of V_2O_5 thin films annealed at different temperatures.

Fig. 3.2 shows the XRD patterns of the V_2O_5 films annealed at different temperatures. As shown in the pattern of the as-grown film, no V_2O_5 peak appears (the other peaks belong to the FTO substrate). This means that the as-prepared film is amorphous. As the annealing temperature increases from 400 to 500 ℃, a peak appears at 20.2 ° for the (001) plane of α-

V_2O_5. The intensity of the α-phase (001) peak increased significantly when the sample was annealed at 450 ℃ and 500 ℃ compared with that annealed at 400 ℃. Moreover, the sample annealed at 500 ℃ also shows a peak at 12 ° for (101) α-V_2O_5 as well as a new weak peak at 12.6 ° for (002) β-V_2O_5.[73] In particular, when the annealing temperature increases to 550 ℃, the intensity of some peaks of α-V_2O_5 decreases, while the peak at 12.6 ° for β-V_2O_5 increases. This result reveals that the annealing temperature not only affects the forming crystals but also causes phase transition in the local crystalizing of the V_2O_5 structure. During the annealing, the energy for the diffusion of V and O ions is enough to form α-V_2O_5 at low temperature (below 500 ℃). At higher temperature (500 – 550 ℃), some of the α-V_2O_5 structures become unstable and are distorted to form mixed phases of α-β V_2O_5 structures.[205] The process of transition from the α phase to the β phase and restructuring into α-V_2O_5 occurs simultaneously. This process is just the beginning, so the XRD intensity of the sample is very weak.

Fig. 3.3a and 3.3b show cross-sectional SEM images of the sample before and after annealing, respectively. The as-grown sample shows uniform thickness about 698 nm while the sample annealed at 500 ℃ reveals coexistence of thin film with thickness about 340 nm and nanorods with length 979 nm and diameter 206 nm. Fig 3.3c shows a TEM image of the nanorods and the high-resolution TEM (inset image) indicates high crystallinity of V_2O_5 film. The survey of XPS spectroscopy (Fig. 3.3d) shows that there exist composition of F1s, O1s, V2s, and V2p. The composition of F1s belongs to FTO substrate and O1s in pure V_2O_5 which appears in peak at 530.0 eV (inset Fig. 3.3d) corresponds to the bonding of oxygen with vanadium in V_2O_5 lattice. The peaks at 524.5 eV and 517.2 eV (inset Fig. 3.3d) correspond to $V2p_{1/2}$ and $V2p_{3/2}$ of V^{5+} (V_2O_5).[206]

Fig. 3.4 reveals the room-temperature PL spectra of the V_2O_5 micro-nanostructure. The PL spectrum shows three peaks located around 410 – 430 nm, 520 – 540 nm, and 690 – 710 nm. The main peak around 520 – 540 nm is from the band-edge transition of V_2O_5, while the peak around 410 - 430 nm is caused by the transition from the top of the conduction band to the valance band.[74,171,207,208] The emission at 690 – 710 nm is the extrinsic transition formed by oxygen vacancies due to the annealing process.[69,72,159] The PL intensity increases due to the rearrangement of the structure with longer nano-rods when the sample is annealed at higher temperature.[159,174] In particular, the peak around 690 – 710 nm was strongly enhanced compared with other peaks, which clearly shows the effect of the annealing temperature on the defects in the V_2O_5 films.

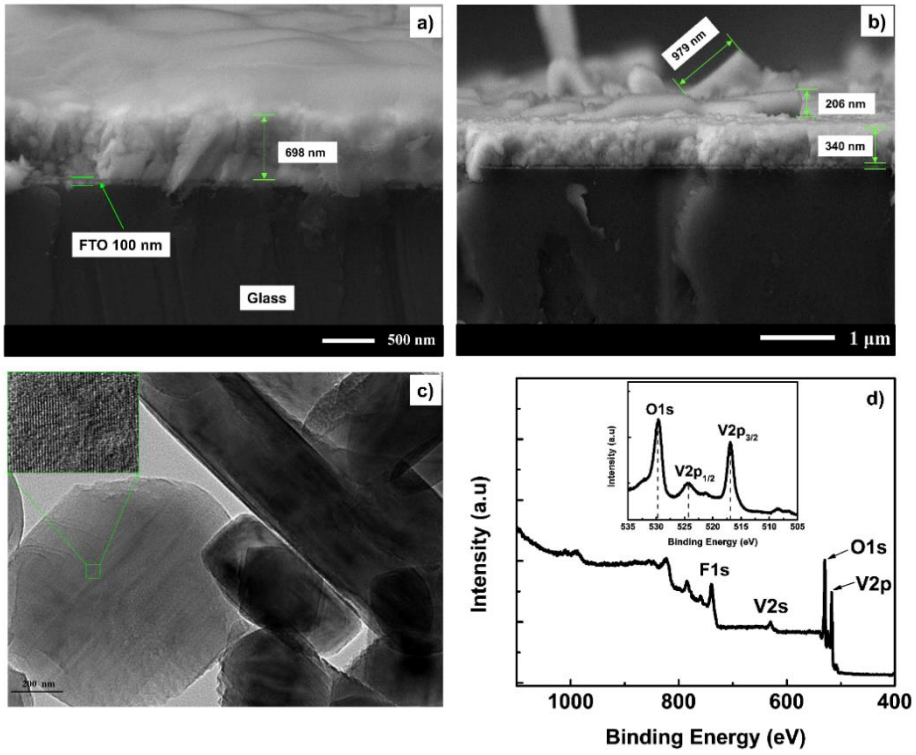

Figure 3.3. Cross-sectional SEM images of thin film before annealing (a), after annealing (b), TEM images (c), and XPS survey spectrum of V_2O_5 film (d).

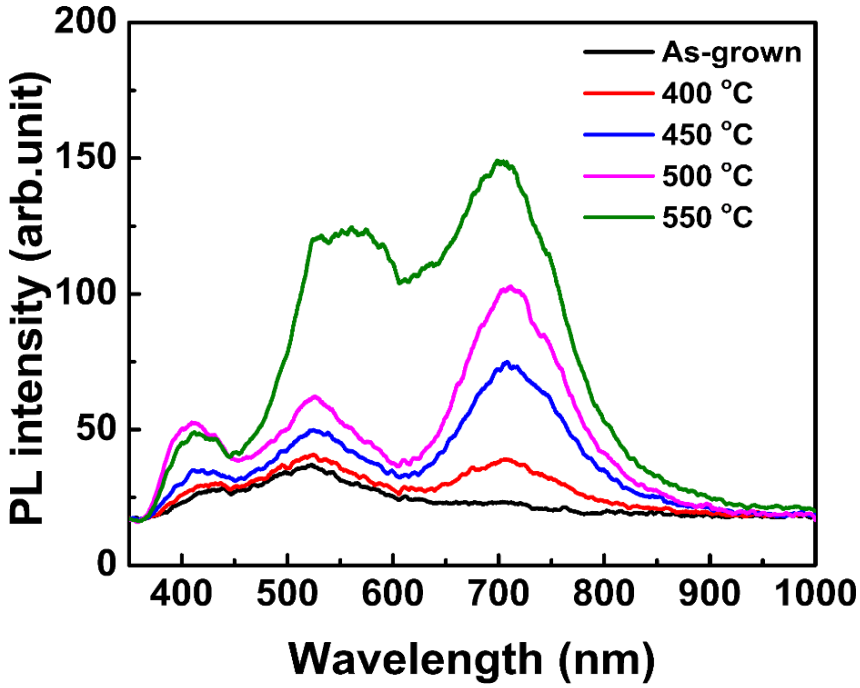

Figure 3.4. Room-temperature PL spectra of V_2O_5 thin films annealed at different temperatures.

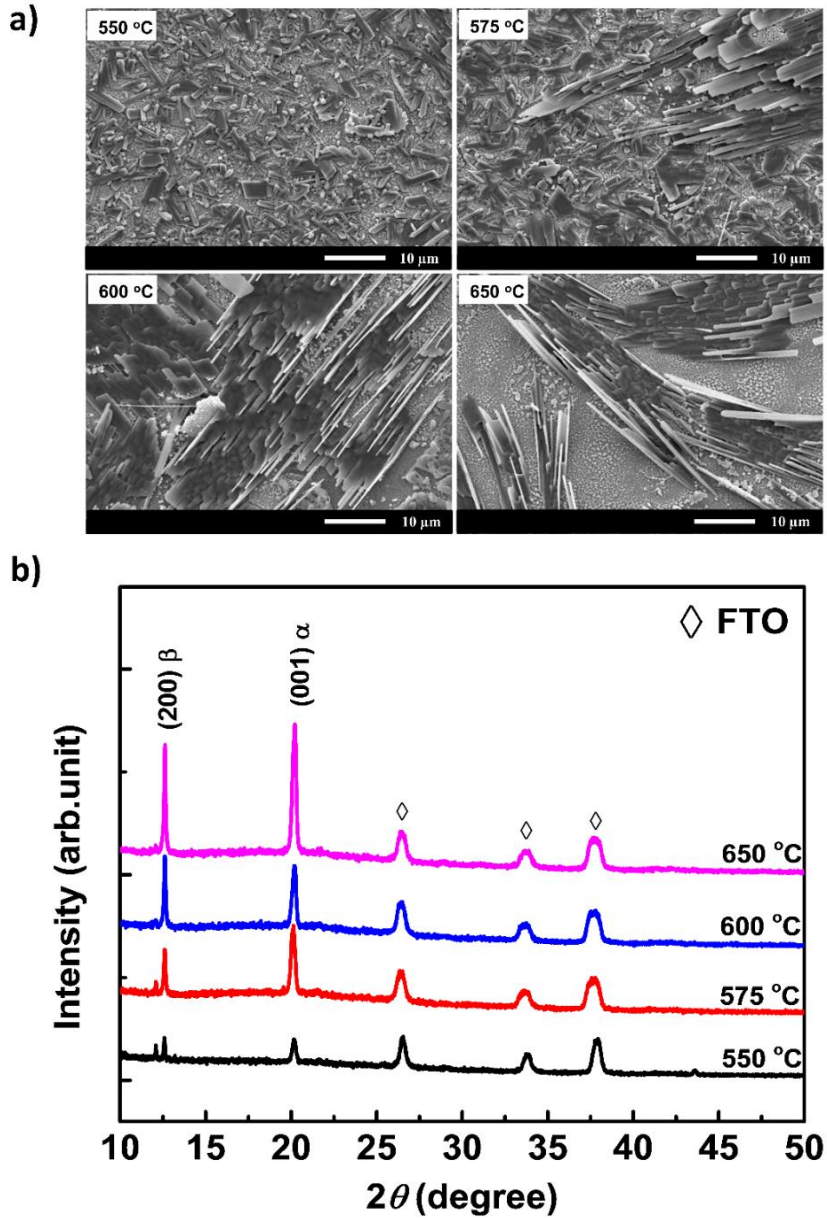

Figure 3.5. Effect of annealing temperature on the surface morphology and structural properties of V_2O_5 film. (a) SEM images of V_2O_5 film and (b) XRD of V_2O_5 film.

The mixing of α-V_2O_5 and β-V_2O_5 phases was clearly shown when the annealing temperature increased from 550 to 650 ℃. As shown in Fig 3.5a, when the annealing temperature increased to 575 ℃, the rod array with length about 1 – 4µm and diameter about 200 - 500 nm coexisted with a plate array with length up to 10 µm and diameter ~ 2 – 5 µm. In the sample annealed at 600 ℃ and 650 ℃, the surface morphology of the thin film sharply changed to long rods with length up to 10 µm and diameter ~1 µm on the slices of V_2O_5 with length and width up to micrometer. Fig. 3.5b shows that the

intensity of the XRD peak of β-V_2O_5 at 12.6 ° strongly increases, while the peak of α-V_2O_5 at 12 ° disappears when the film is annealed at 650 ℃. The intensity of both XRD peaks from the (001)-α and (200)-β planes of the V_2O_5 film strongly increases at higher temperature. The mechanism of the α-β phase transition in V_2O_5 was explained in previous reports.[205,209,210] In this case, the process of the phase transition and arrangement into well-crystallized structure occurs simultaneously in the local structure of V_2O_5 during the high-temperature treatment to form a mixture of α-β phase V_2O_5.

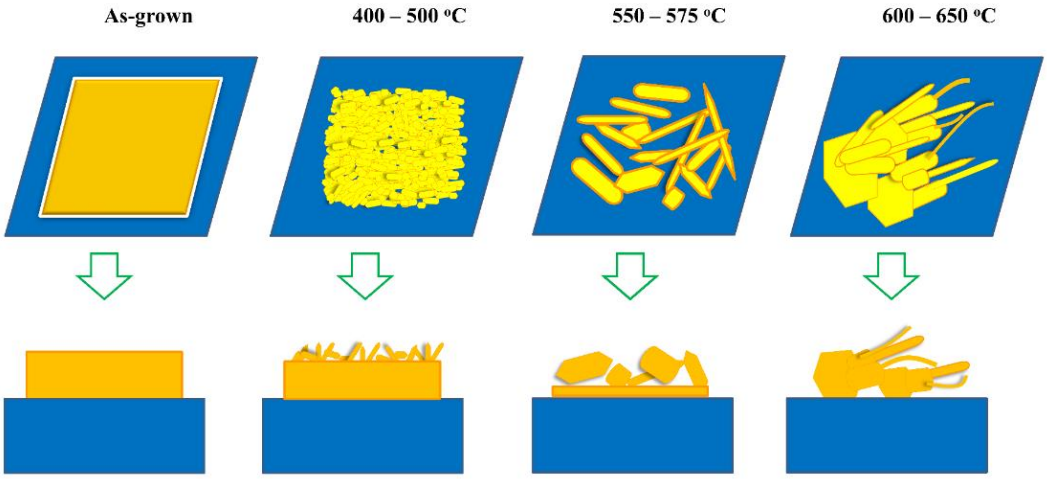

Figure 3.6. Schematic illustration of the temperature-dependent growth of V_2O_5 thin films.

The schematic in Fig. 3.6 summarizes the temperature-dependent growth of morphologies of V_2O_5 nanostructures. The initial amorphous thin film was deposited from electrolyte solution containing ionic cluster of vanadium oxide. During the annealing, thermal energy was provided for activating crystal and changing morphology.[76] Small crystallites coalesce together to form larger crystallites (at 400 ℃) and grain boundary diffusion at the surface was boosted (450 – 500 ℃) to form nanorod.[211] The post-annealing treatment at higher temperature (550 – 570 ℃), a higher surface diffusion mobility is more favorable for extending process of the length and width of nanorod.[76] For further higher annealing temperature (600 – 650 ℃), the rod's growth process continues. However, due to the coexisting growth of α- and β-V_2O_5, growth orientation is not preferential, therefore, the rods, plates, and slides like structure were observed.

Fig. 3.7a shows highly enhanced PL emission from the micro-length rod-plate mixture of α-β phase V_2O_5. The long length of up to over 10 μm of the micro-length rod-plate mixture of α-

β V_2O_5 can create numerous defects on the sample. This leads to an intense PL peak at 690 – 710 nm.[159] The enhanced absorption is due to the formation of large amounts of V^{3+} and V^{4+} oxidation states during annealing and may also have caused the enhanced PL intensity.[163] Interestingly, the PL peak intensity around 520 – 540 nm increases as the annealing temperature increases. This result could be explained by the difference in the surface morphology and local structure of the V_2O_5. The band gap of β-V_2O_5 is smaller than that of α-V_2O_5, and the split-off conduction band was wider for β-V_2O_5 than α-V_2O_5.[151,152] Absorption measurement revealed that band gap of V_2O_5 thin films was reduced from 2.68 to 2.32 eV due to the phase transition from α-V_2O_5 to β-V_2O_5.[153] Our sample has a mixture of α-β phase V_2O_5 structure, which means two band structures coexist in the V_2O_5 material. This leads to a concurrent transition in α-V_2O_5 and β-V_2O_5.

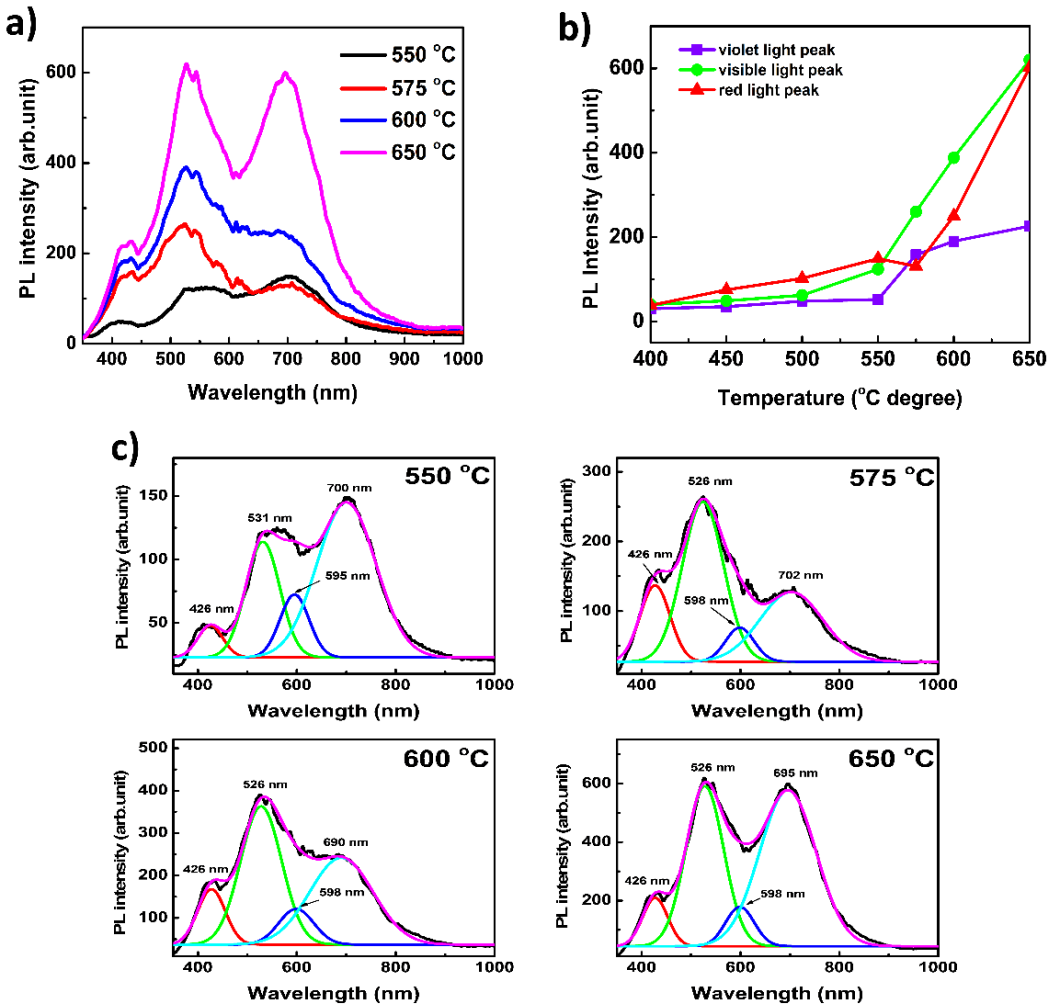

Figure 3.7. Room-temperature photoluminescence behavior of mixed α-β phase V_2O_5: (a) Room-temperature PL spectra, (b) Effect of mixed α-β phase V_2O_5 on PL intensity, and (c) Fit of PL spectrum by Gaussian graph.

Fig. 3.7b shows a summary of the effect of annealing on the PL properties of the V_2O_5 films. The PL intensity of the three peaks increases when the annealing temperature increases. In particular, the PL intensity of visible light emission increases more strongly compared with other emissions when the mixture of α-β phase V_2O_5 was formed. Fig. 3.7c reveals the film emitted visible light, which was fitted to four Gaussian graphs. The peak at 526 – 531 nm belongs to the band-edge transition of α-V_2O_5,[72,171] while the peak at 595 – 598 nm is believed to be from the band-edge transition of β-V_2O_5. The coexisting emission of α-V_2O_5 and β-V_2O_5 in thin film leads to the more wide emission from 400 to 800 nm compared with emission of single α-V_2O_5[72,212] or single β-V_2O_5.[161]

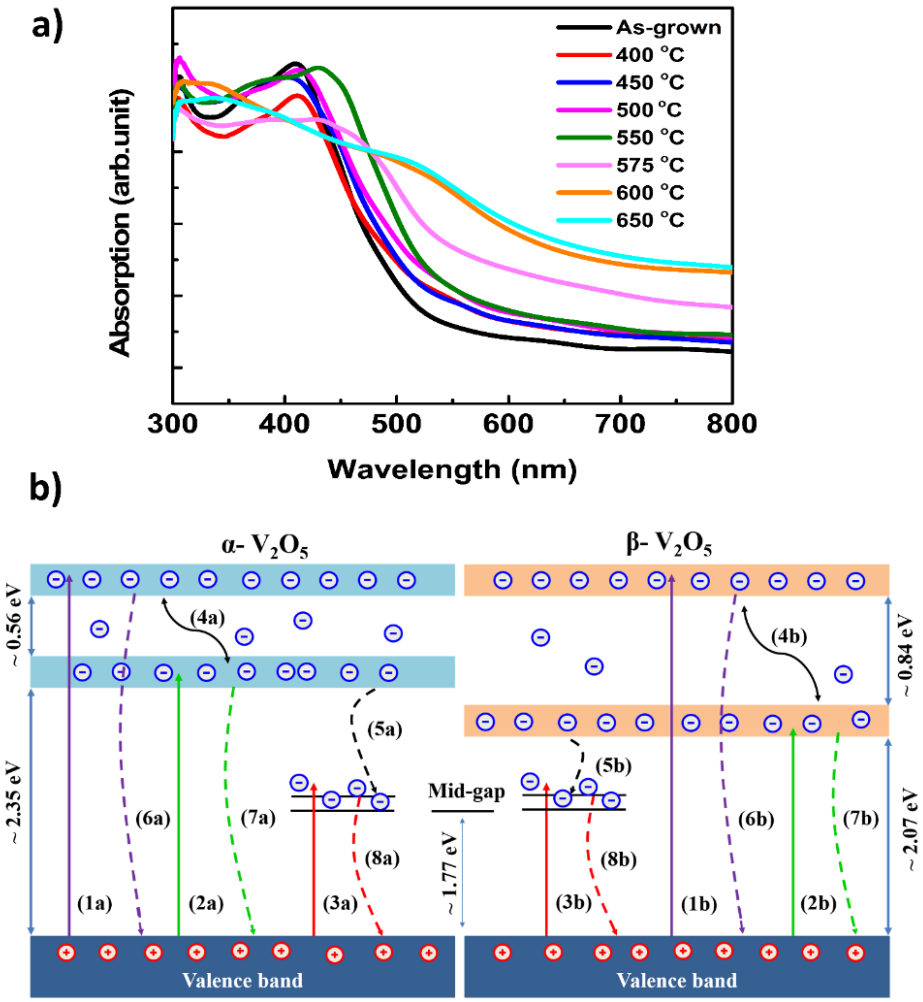

Figure 3.8. (a) Absorption spectra of α-V_2O_5 and mixed α-β phase V_2O_5 and (b) Processing mechanism of charge separation and charge recombination in mixed α-β phase V_2O_5.

We next carried out measurements using UV-vis spectra. Fig. 3.8a shows that α-V_2O_5 strongly absorbs light at a wavelength of 410 nm with a peak around this wavelength. The absorption slightly shifts toward blue light, while the tailing of the absorption from 410 nm to 530 nm quickly decreases. This blue-shift may be affected by the crystallite size and strain values.[122,153] When the sample is annealed at 550 ℃, the absorption shifts toward a long wavelength due to the structure change to form the mixture of the α-β phase V_2O_5 structure. When the annealing temperature increases from 575 to 650 ℃, the tailing absorption strongly shifts to lower energy with high intensity absorption. This result is believed to be a consequence of the simultaneous and intense absorption of the α-V_2O_5 and β-V_2O_5, as well as the enhanced PL intensity. Moreover, the increase of absorbance near the infrared range is a result of optical excitation of the mid-gap state.[118]

Fig. 3.8b illustrates the process of the charge separation and recombination mechanism. Electrons are separated from the valence band into three states: the V3*d* state ("1a" and "1b" in Fig. 8b), the V3*d* split-off conduction band ("2a" and "2b" in Fig. 3.8b), and the mid-gap state ("3a" and "3b" in Fig. 3.8b).[69,119,213] After that, the electrons relax into the conduction band ("4a" and "4b" in Fig. 3.8b) or relax to the mid-gap state ("5a" and "5b" in Fig. 3.8b) before recombination ("6a", "7a", "8a", and "6b", "7b", "8b" in Fig. 3.8b).[69] In the α-V_2O_5 structure, the PL peak intensity around 690 - 700 nm from the defect states is higher than that of other peaks due to electrons relaxing to the mid-gap state before recombining. In the mixture of the α-β phase V_2O_5, the recombination process in the band-edge transition of α-V_2O_5 and β-V_2O_5 ("6a" and "6b" in Fig. 3.8b) occurs simultaneously. This leads to high enhancement of the visible light emission. That means that after high temperature treatment, a higher-quality crystal is formed, and the mixture of α-β phase V_2O_5 films leads to enhanced band-edge transition in the V_2O_5 due to the contribution of both transitions in α-V_2O_5 and β-V_2O_5.

3.3 Chapter summary

In summary, V_2O_5 thin films were fabricated by an environmentally friendly method. The results revealed that the annealing temperature strongly affects the surface morphology, structures, and optical properties of the V_2O_5 film. As the annealing temperature increases, the as-prepared amorphous film transforms to a nano-rod film and becomes micro-nano-rods and plates as the temperature increases from 550 to 650 ℃ with coexisting α-V_2O_5 and β-V_2O_5 structures. In particular, the V_2O_5 film strongly

absorbs visible light due to the formation of high-quality crystals of mixed α-β phase V_2O_5 structure, which leads to enhanced PL intensity from the band-edge transition.

Chapter 4. Morphology, Structure, and Optical Characterization of V_2O_5 Micro-nanostructures

4.1. Motivation

Thin-film V_2O_5 shows visible PL due to a band edge transition and defects, but its emission intensity is very weak at room temperature.[212] Therefore, to enhance PL intensity, various V_2O_5 nanostructures such as NRs have been grown,[214] and hybrid nanostructures have been also developed.[68,161] Other researchers have reported that the PL intensity of the V_2O_5 nanostructure strongly depends on the synthesis method, crystal structure, and external treatment.[160,174] These enhanced PL properties can make V_2O_5 a promising material for applications such as indicators and light sources. The effect of morphologies V_2O_5 nanostructure including thin film, NSs, and NWs to PL peak position have been reported.[61] However, the effect of morphologies to PL intensity is not discussed.

In this chapter, synthesis of various V_2O_5 nanostructures, along with their resulting room-temperature PL properties was presented. Four types of nanostructures, NPs, NRs, NWs, and NSs, are fabricated by the hydrothermal method[30,202] and the chemical reaction method,[46] and their morphologies, structures, and oxidation states are investigated. Room temperature PL for each of the nanostructures are also carried out and discussed.

4.2. Results and discussion

Fig. 4.1 and 4.2 show the morphologies of V_2O_5 nanostructures according to SEM and TEM measurements, respectively. As shown in figure, four kinds of V_2O_5 nanostructures were grown with varying sizes: Fig. 4.1a and 4.2a show that V_2O_5 NPs had a small size of 30 – 50 nm. The morphology of V_2O_5 NRs is shown in Fig. 4.1b and 4.2c. The NRs had a diameter of about 50 – 100 nm and a length of about 250 – 450 nm. Fig. 4.1c and 4.2e are typical images of V_2O_5 NWs. The images reveal flexible, belt-like structures with diameters of roughly 30 – 50 nm and lengths up to 10 μm. SEM and TEM images in Fig. 4.1d and 4.2g reveal V_2O_5 NSs with homogenous shape and diameters of

about 150 – 400 nm. Higher-magnification TEM images (Fig. 4.2b, 4.2d, 4.2f, and 4.2h) show the formation of an "outer shell" of the V_2O_5 nanostructures that is distinct from the internal structure. Compared with the other nanostructures, the NSs have entirely spherical morphologies with a thicker "outer shell" formed during annealing.

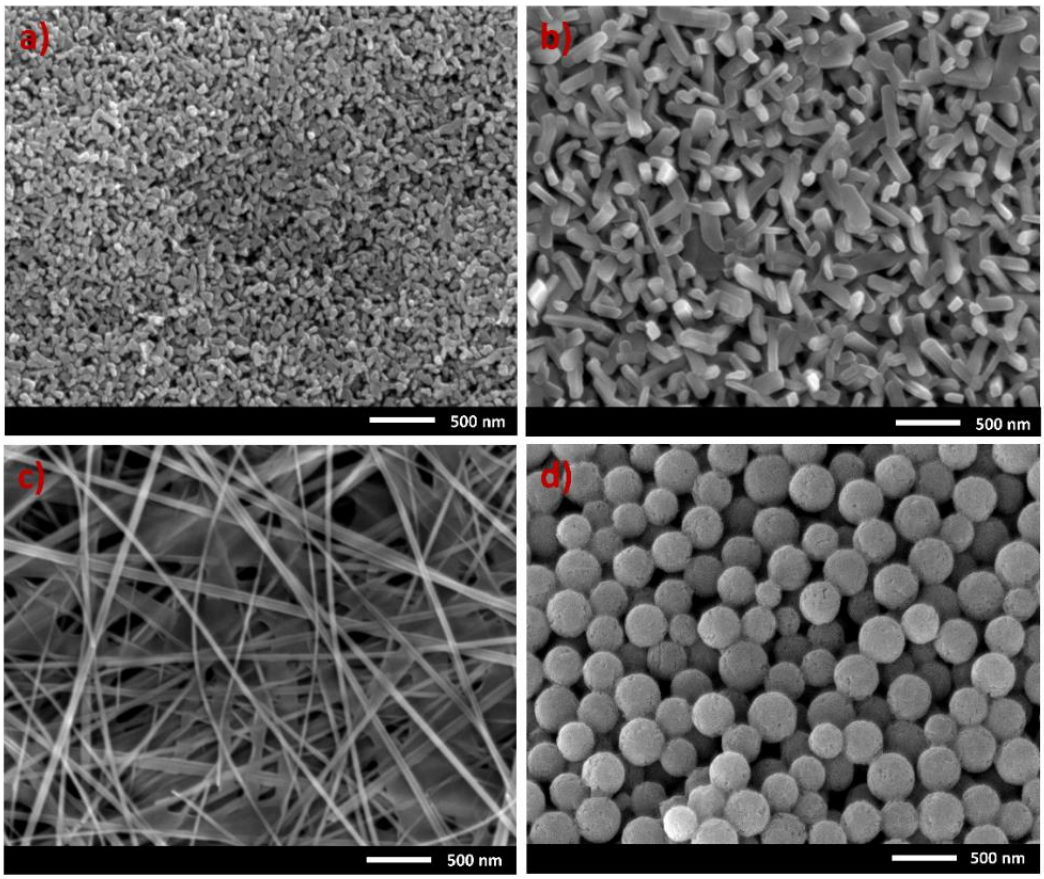

Figure 4.1. SEM images of V_2O_5 (a) nanoparticles, (b) nanorods, (c) nanowires, and (d) nanospheres.

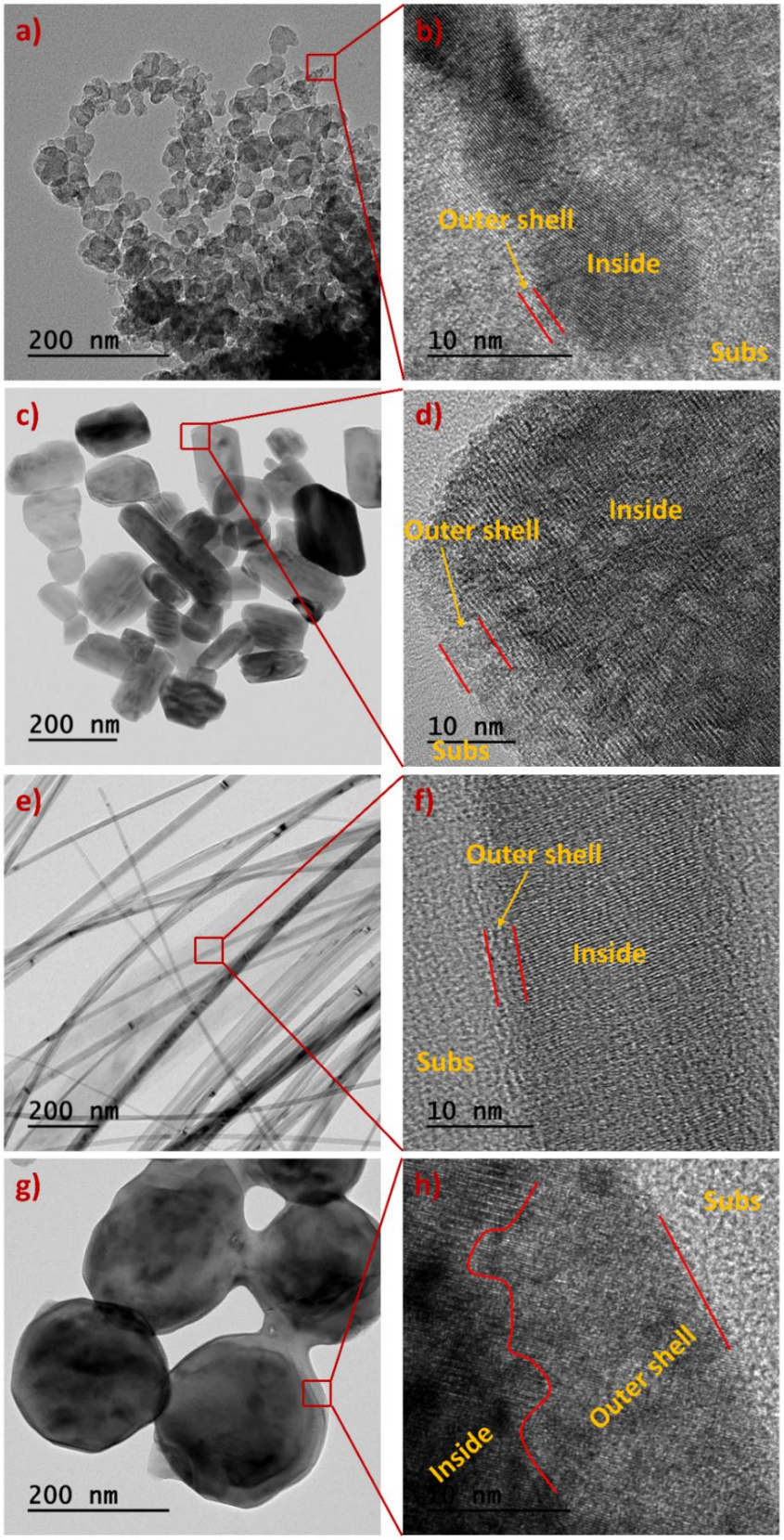

Figure 4.2. TEM images of V_2O_5 (a-b) nanoparticles, (c-d) nanorods, (e-f) nanowires, and (g-h) nanospheres.

Fig. 4.3a shows the XRD patterns of V_2O_5 nanostructures. All the nanostructures showed a diffraction peak corresponding to the (001) plane of orthorhombic α-V_2O_5 at 20.3°.[71,79] Additional peaks corresponding to the (200), (101), (110), and (301) planes also were observed in all structures. V_2O_5 NPs, NRs, and NSs also revealed peaks corresponding to (011) and (310) planes at 32.4° and 34.3°, respectively, while these peaks were not observed in V_2O_5 NWs.

To support the XRD results, the Raman spectra of V_2O_5 nanostructures were measured and are presented in Fig. 4.3b. The spectra reveal the typical Raman-active modes of α-V_2O_5.[71,79] The predominant low-frequency Raman peak at 145 cm^{-1} corresponds to bent vibration mode B_{3g}, while the peak at 197 cm^{-1} comes from the bending vibration of O-V-O. The A_g mode of atoms oscillating at V=O is observed in the peaks at 282, 302, and 403 cm^{-1}. V_2O_5 NPs, NRs, and NWs show high intensity peaks at 483, 526, and 700 cm^{-1} from the vibration modes A_g (V-O_3-V), v (d_4), and v (d_3), respectively, while these vibrations were very weak in the Raman spectra of NSs. The highest-frequency v (d_1) mode at 996 cm^{-1} comes from the displacement of O_1 atoms through the V=O_1 double bonds.[30,215,216]

Fig. 4.4a shows the variation of XPS spectra according to particle structure. The O1s (530.05 eV), V2$p_{1/2}$ (524.80 eV), and V2$p_{3/2}$ (517.10 eV) core-level spectra of NPs, NRs, and NWs are consistent with each other, while those of the NSs shift toward lower binding energy. Deconvolution fits (Fig. 4.4b) elucidate that the V2p peaks ($p_{3/2}$) of the NPs, NRs, and NWs mainly consist of the V^{5+} oxidation state (517.3 eV) corresponding to the phase of α-V_2O_5.[217] However, the V^{4+} oxidation state (516.3 eV) is negligible in the NPs, is significant in the NRs and NWs, and is almost dominant in the NSs. The V^{4+} oxidation states are created from the thermal activation of V=O through V=O ↔ V^{4+}+O^- due to thermal treatment.[218] The amounts of V^{4+} in the V2$p_{3/2}$ peaks were 4.7, 10.9, 12.8, and 30.0 % in NPs, NRs, NWs, and NSs, respectively. The V_2O_5 NSs formed layer-by-layer as nanoplate-like structure on the surface.[32,219] This leads to formation of a thick “outer shell” between interface plates and an associated increase to the V^{4+} oxidation states and defects in the NSs.

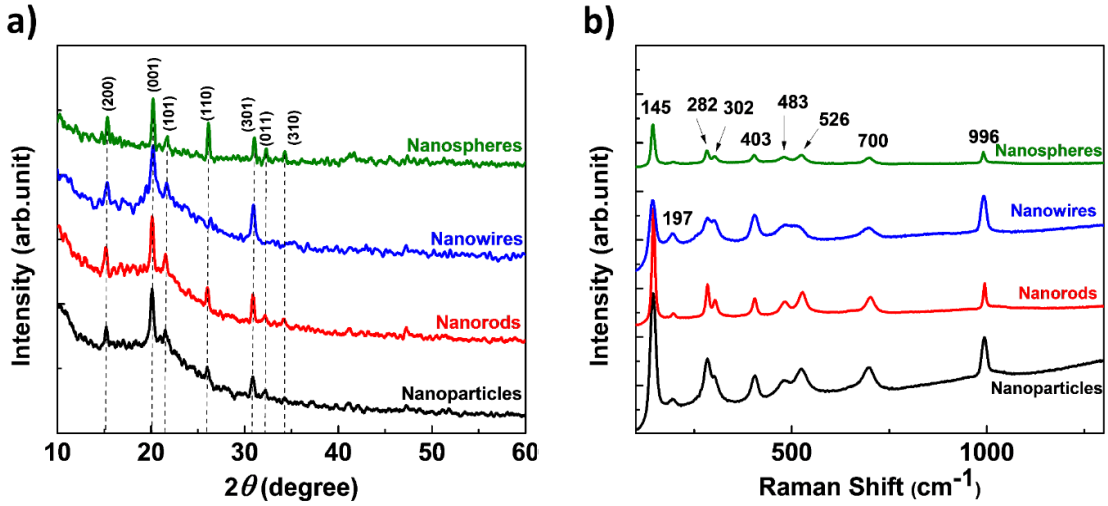

Figure 4.3. XRD patterns (a) and Raman spectra (b) of V_2O_5 nanostructures.

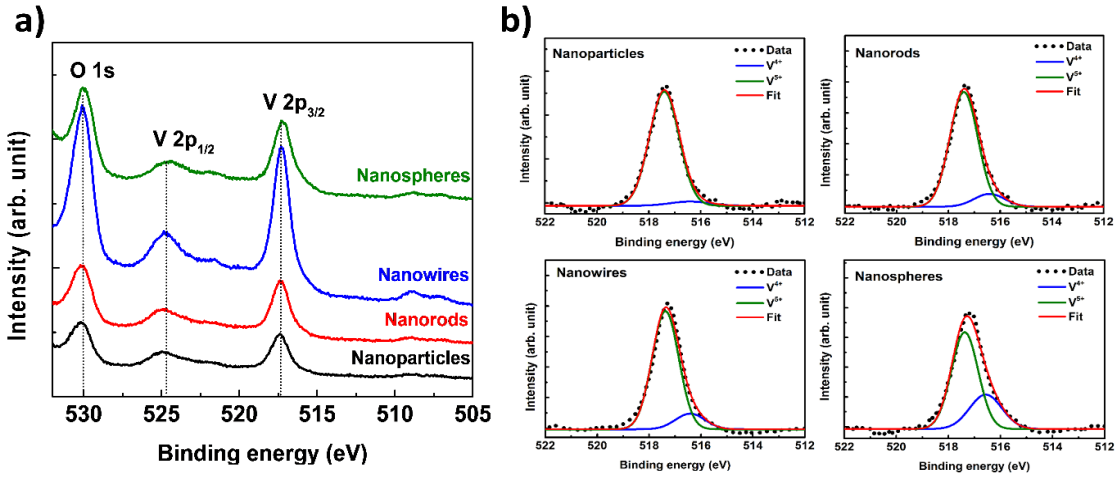

Figure 4.4. XPS spectra of V_2O_5 nanostructures. (a) Full spectra and (b) the $V2p_{3/2}$ peak deconvolved into two Gaussians corresponding to the V^{4+} and V^{5+} oxidation states.

Fig. 4.5a represents the PL spectra of V_2O_5 nanostructures measured at room temperature. The PL of V_2O_5 nanostructures showed a broad emission peak, centered at 395 nm (3.14 eV) for NSs and at 426 nm (2.91 eV) for the other nanostructures, caused by the transition from the top of the conduction band to the valance band.[61,74] The peak at ~526 nm (2.35 eV) is due to the band edge transition in V_2O_5 with a bandgap energy of 2.30 – 2.40 eV.[72,220] V_2O_5 NPs and NRs revealed another PL peak centered at ~665 nm (1.86 eV), while V_2O_5 NWs and NSs show a PL peak centered at 710 nm (1.74 eV) due to mid-gap states formed by oxygen vacancies incorporated into the structure during growth.[212,214,221] Fig. 4.5a shows that V_2O_5 NSs produce very high PL intensity, while NPs, NRs, and NWs exhibit weaker and slightly morphology-

dependent PL. The slightly enhanced PL intensities of NWs and NRs compared to NPs are due to long length of the structure when the samples were annealed at higher temperature (NRs) or grown for longer time (NWs).[174,214]

The PL intensity of NSs was strongly enhanced compared with other structures. As shown in Fig. 4.5a, the PL intensities from mid-gap states of V_2O_5 NPs, NRs, and NWs were very weak, their intensities were amplified 28.7, 19.1, and 17.7 times, respectively, for comparison with the PL spectra of NSs. In particular, the highest energy peak of the NSs spectrum was 252, 251.5, and 137 times greater than the corresponding peak of the NPs, NRs, and NWs spectra, respectively. This result may be explained by the differences in how the structures are grown, which may lead to the special structure of the NSs. The structures of the V_2O_5 NPs, NRs, and NWs tended to increase in size (length and width) when the samples were thermally treated (Fig. 4.6 and Fig. 4.7). A rod-like structure is observed when the sample was annealed at 400 ℃ (Fig. 4.6a), and the structures began to transform into nanorod arrays at 450 ℃ (Fig. 4.6b). Similarly, Fig. 4.7a reveals the rod-like nanostructures formed as hydrothermal treatment at 180 ℃ for 48h and rod-wire-belt-like nanostructures were formed at 205 ℃ for 24h. In contrast, when annealed at increasing temperatures, the dense, solid NSs started to partition into plate-like structures and were eventually distorted and destroyed to form nanoparticles and nanorods (Fig. 4.8).

The schematic in Fig. 4.9 summarizes the temperature-dependent and time-dependent growth of morphologies of V_2O_5 nanostructures. Wang *et al.* [61] investigated the effect of morphologies V_2O_5 nanostructure to PL peak position, consequence, the PL spectrum show the peak at 391 nm for thin film, peak at 385 nm for NSs while the NWs reveal three peaks at 391, 620, and 688 nm. However, the effect of morphologies to PL intensity is not discussed. Wang *at al.*[214], Hu *et al.*[160], and Zou *et al.*[161] reported the highly intensity visible PL (broad emission range about from 500 – 750 nm) of NRs and V_2O_5/ZnO NRs obtain due to excess electron from defect in V_2O_5 or transferred from ZnO.

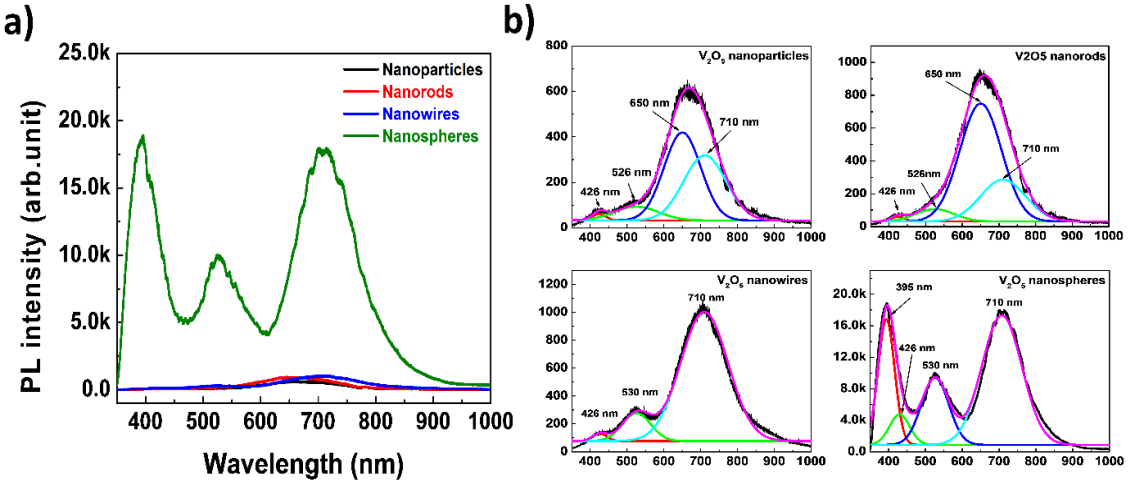

Figure 4.5. (a) Room-temperature PL spectra of V_2O_5 nanostructures and (b) deconvolution of the PL spectra into Gaussian components.

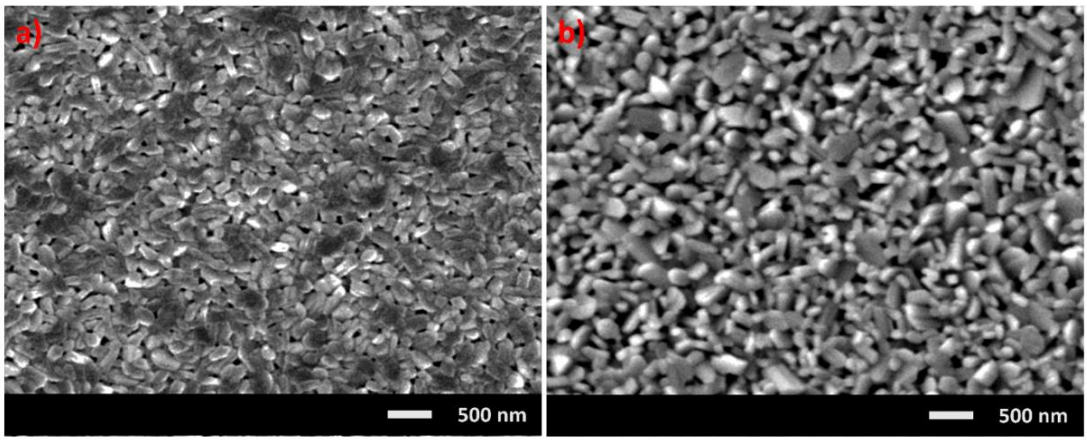

Figure 4.6. The samples were annealed at 400 ℃ (a) and 450 ℃ (b) for 2h.

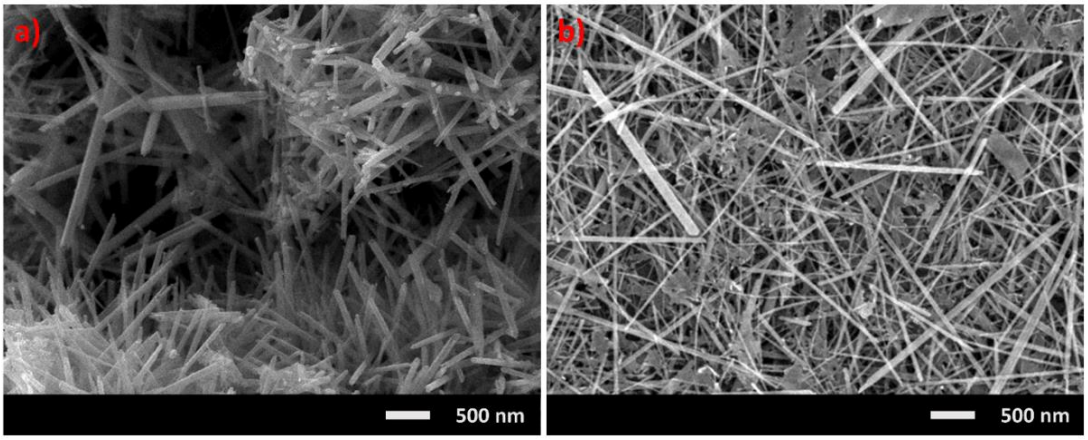

Figure 4.7. Hydrothermal treatment at 180 ℃ for 48h (a) and at 205 ℃ for 24h (b).

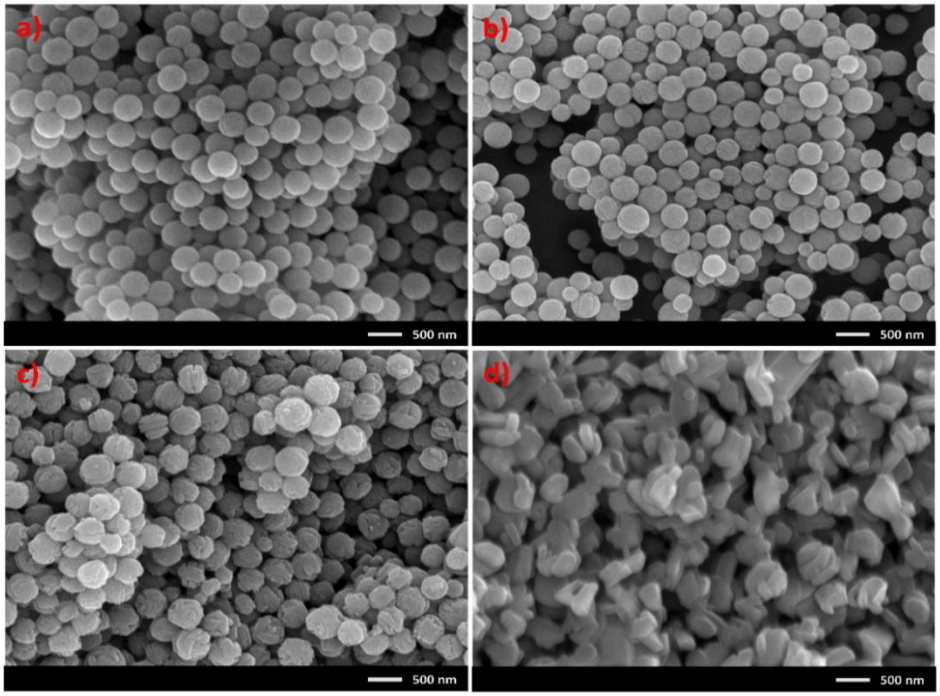

Figure 4.8. $V(OH)_2NH_2$ nano-spheres (a) without annealing, (b) with annealing at 375 ℃, (c) with annealing at 400 ℃, and (d) with annealing at 450 ℃ for 2h.

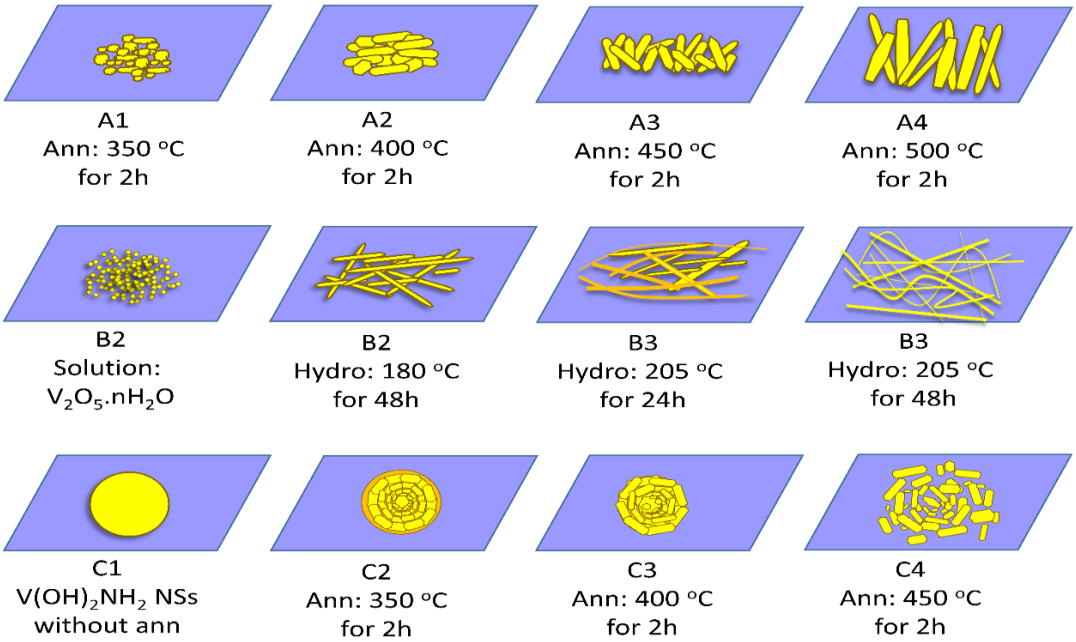

Figure 4.9. Schematic illustration of the temperature-dependent and time-dependent growth of V_2O_5 nanostructures. A1, A2, A3, and A4 correspond to products from fabrication system A. B1, B2, B3, and B4 correspond to products from fabrication system B. C1, C2, C3, and C4 correspond to products from fabrication system C.

The photoluminescence of V_2O_5 have relative with the V=O double bonds vibration state due to formed (V^{4+}-O^-) from (V^{5+}=O^{2-}) when it absorbed laser source.[156–158,222,223] This is process of optical transition between neighboring non-isovalent cations V^{4+} and V^{5+} due to the optical absorption.[224] As shown in Fig. 4.4a and 4.4b, the contribution of V^{4+} oxidation state to the $V2p_{3/2}$ peaks was much greater in the NSs sample (30 %) compared to the NPs (4.7%), NRs (10.9%), and NWs (12.8%). The enhanced number of V^{4+} oxidation states in the NSs may be due to formation of defects in the "outer shell" and in the interfaces of their internal plate-like structures. The large number of V^{4+} oxidation states NSs was also reflected in the weak Raman intensity (Fig. 4.3b), showing that the V=O double bonds in the "outer shell" of NSs were weaker than those in the other structures. An electron can therefore transfer more easily from oxygen to the vanadium ion, which increases strong excitation by UV light in V_2O_5 NSs to form excited singlet and triplet states.[157,158,163,222] Moreover, the vanadium atoms near the vicinity of defects receive excess electrons from the crystal due to removed oxygen atoms.[86,118,162] These electrons can fill a part of the conduction band or the split-off band.[118] As a result, the photoluminescence in V_2O_5 NSs is strongly enhanced.

Fig. 4.5b shows deconvolution of the PL to a number of Gaussians: the NWs spectrum was fitted with three Gaussians, and spectra of the other structures were fitted with four Gaussians. In NPs and NRs, the peak due to oxygen vacancies shifted to higher energy compared to those seen in the PL spectroscopy of NWs and NSs. This peak can be well-fit by two Gaussians centered at 650 nm (1.9 eV) and 710 nm (1.74 eV). As indicated in Fig. 4.5b, V_2O_5 NSs showed an intense ultraviolet PL (UV PL) peak centered at ~395 nm (3.14 eV) that was not observed from the NPs, NRs, and NWs. This PL peak again demonstrates that the V_2O_5 NSs were strongly excited by the UV light source and the direct recombination from electrons from V$3d$-t_{2g} state with ground state.

4.3. Chapter summary

V_2O_5 NPs, NRs, NWs, and NSs were prepared by hydrothermal and chemical reaction methods. XRD and Raman results revealed that all of these nanostructures had an α-V_2O_5 phase with an orthorhombic structure. The oxidation states in the micro-nanostructures were investigated, and a large increase of the V^{4+} oxidation state was observed in the NSs. The NPs, NRs, and NWs showed weak and broad PL properties, whereas the NSs revealed much higher PL intensity due to numerous electrons that were

created from oxygen vacancies. In particular, the NSs showed intense UV PL near 395 nm (3.14 eV). These electrons also enhanced sunlight photocatalytic activity in V_2O_5 NSs. Moreover, the small size of V_2O_5 NPs increases the surface contact area with water molecules, resulting in more efficient photo-degradation than V_2O_5 NRs and NWs. The PL and photocatalytic activity properties in the nanostructures showed strong dependence on the oxidation state and morphology of the nanostructures.

Chapter 5. Room Temperature Photoluminescence Behaviour of V_2O_5 Micro-nanospheres

5.1 Motivation

To enhance the PL intensity, various V_2O_5 micro-nanostructures have been grown, such as thin film, micro-nanoplates, micro-nanoslides, nanoparticles, micro-nanorods, micro-nanowires, and nanospheres (as shown in chapter 3 and chapter 4). The result shows the super PL intensity in V_2O_5 nanospheres compared with other micro-nano structures morphologies.

In this chapter, I report on the synthesis of V_2O_5 micro-nanospheres with different size and their PL properties at room temperature with difference distributions. The micro-nanostructure and oxidation state of the micro-nanospheres were investigated, and PL measurements were performed at room temperature. The life time (TRPL) and PL mechanism of the nanospheres are discussed.

5.2 Results and discussion

Fig. 5.1a and 5.1b show the morphology and a histogram of V_2O_5 nanospheres (Sample B) obtained from SEM measurements. The size distribution of the nanospheres was evaluated using the histogram, which has a Gaussian profile. The SEM image and histogram reveal that the nanospheres have a diameter of 284±22 nm, spherical morphology, and numerous defects on their surfaces. These defects are due to the growth feature of V_2O_5 with a layer-by-layer (plate-like) structure and the formation of plate-like structure edges for growth by etching.[225,226]

A TEM image of the nanospheres is shown in Fig. 5.1c. The image shows solid sphere structures. Fig. 5.1d shows a high-resolution TEM image. An atomic array of V_2O_5 is observed at the center of the sphere, indicating high crystallinity. On the surface (outer shell), the atomic array becomes disordered due to the etching, implying poor crystallinity and the formation of numerous defects. In the observed region, a lattice parameter of b=3.39 Å for α-V_2O_5 was obtained from the TEM image (Fig. 5.1d). The center of the sphere shows a preferential [010] orientation.

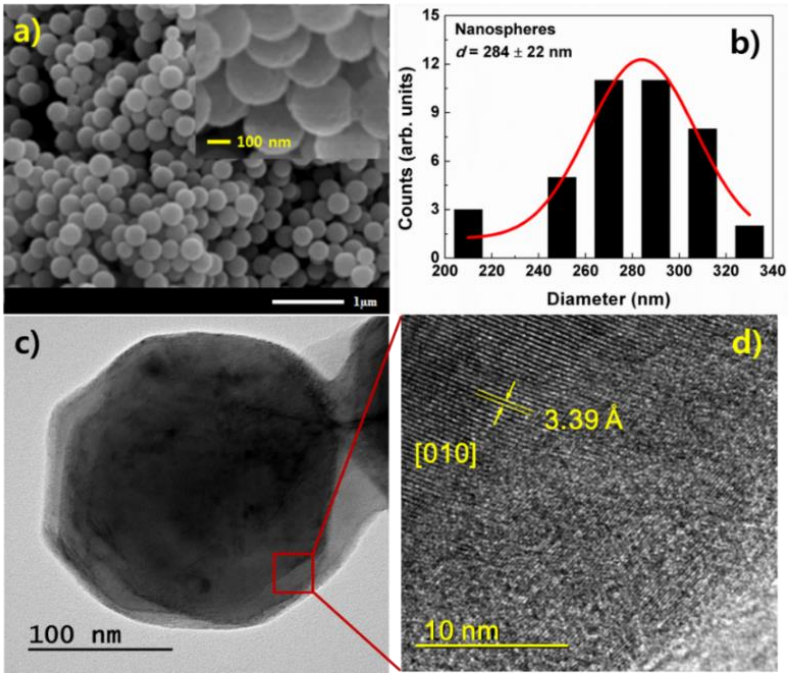

Figure 5.1. (a) SEM image, (b) Histogram of V_2O_5 nanospheres, (c) TEM image of the nanospheres showing the solid sphere structure, and (d) High-resolution TEM image with atomic array of V_2O_5 observed at center of the nanosphere.

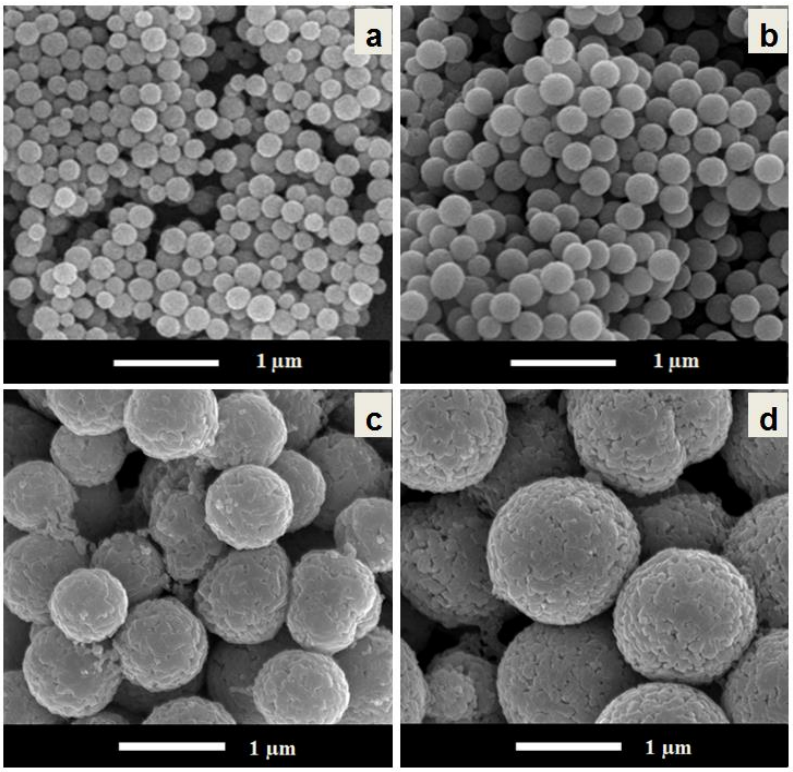

Figure 5.2. SEM images of V_2O_5 micro-nanosphere: (a) sample A, (b) sample C, (c) sample E, and (d) sample F.

Table 5.1. The dependence size of micro-nanosphere on solution concentration.

Sample	NH_4VO_3 (gram)	H_2O (mL)	1M HCl (mL)	$N_2H_4 \cdot H_2O$ (mL)	Size (nm)
A	0.117	90	0.5	1.5	50-200
B	0.234	90	1	3	200-350
C	0.234	75	1	3	200-400
D	0.234	60	1	3	300-500
E	0.234	45	1	3	600-800
F	0.234	30	1	3	1000-1200

Fig. 5.2 shows the different sizes of micro-nanospheres, the sphere size increase from nano to micro scale with the increasing solution concentration. The detail parameter of solution concentration and scale was listed in Table (5.1).

Fig. 5.3a shows the XRD pattern of the nanospheres (Sample B), where there is a diffraction peak corresponding to the (001) plane of α-V_2O_5 at 20.3°. Additional peaks corresponding to the (200), (101), (110), and (301) planes are also observed. The measured Raman spectra are presented in Fig. 5.3b. The spectra reveal the typical Raman-active mode of α-V_2O_5.[216,227] The results in Fig. 5.3a and 5.3b indicate that the nanospheres contain the α-V_2O_5 phase.

Fig. 5.3c shows the XPS spectra of the nanospheres. The V2p and O1s core-level spectra of the nanospheres shift toward lower binding energy with the appearance of an additional oxygen peak at higher binding energy, which are attributed to the SiO_2 substrate. A deconvolution fit indicates that the V2p peak ($p_{3/2}$) of the nanospheres mainly consists of the V^{4+} oxidation state (516.1 eV). The energy of the peak is very small (0.8 eV) compared with the V^{5+} oxidation state (516.9 eV) corresponding to the α-

V_2O_5 phase.[206,217,228] This result implies that the states are oxidized into a lower oxidation state. Furthermore, the peak maxima of the O1s core-level spectra shifts to lower energy for the nanospheres. The stoichiometry ratios (S_{ij}) of the nanospheres are calculated from the XPS spectra using the following Eq. (5.1).[229]

$$S_{ij} = \frac{C_i}{C_j} = \frac{I_i/ASF_i}{I_j/ASF_j} \qquad (5.1)$$

where C_i and C_j are the concentrations of the elements, I_i and I_j the background corrected intensities of the photoelectron emission lines and ASF_i and ASF_j the atomic sensitivity factors for photoionization of the i_{th} and j_{th} elements. For example, ASF_O and ASF_V are 2.93 and 9.66, which are supplied with the instrument.[229] The O/V rate of the nanospheres is 3.04, while the amount of V^{4+} in the V2p peak is 84%.

Fig. 5.4a presents the PL spectra of phase nanospheres measured at room temperature. The nanospheres exhibit highly intense PL with three main peaks. The PL peak centered at ~530 nm (2.34 eV) is due to the band edge transition in V_2O_5 with a bandgap energy of 2.30 – 2.40 eV.[163,208] Another PL peak centered at ~710 nm (1.74 eV) is attributed to mid-gap states (~1.84 eV) formed by oxygen defects that occurred during growth.[212,214,221] The nanospheres show an intense UV PL peak centered at ~396 nm (3.13 eV), which has not been reported previously. This peak is considered to be due to strong UV absorption resulting from the large amount of V^{4+} oxidation states in the nanospheres (Fig. 5.3c), which can be strongly excited by UV light with wavelength in the range of 250 – 350 nm.[163] Meyn *et al*.[163] investigated the PL properties of V^{4+}-doped oxides such as Al_2O_3 and $YAlO_3$ and reported that the UV light absorption in the oxides can be enhanced by V^{4+}.

The V^{5+} and V^{4+} oxidation states have valence-electron configurations of V $3d^0$ and V $3d^1$ in the valence band,[230,231] respectively. The binding energy (516.1 eV) of the nanospheres with a dominant V^{4+} oxidation state decreases to 0.8 eV, which is small compared with that of α-V_2O_5 (516.9 eV) with a dominant V^{5+} oxidation state. The $3d^1$ valence-electron configuration and the lower binding energy of the V^{4+} oxidation state can significantly increase the probability of transition from the valance band to the V3*d*-t_{2g} and V3*d*-e_g conduction bands via UV light absorption (Fig. 5.5h).[86,207] The enhanced

transition leads to intense PL in the nanospheres. Thus, the PL properties of V_2O_5 nanospheres are considered to strongly depend on the oxidation state.

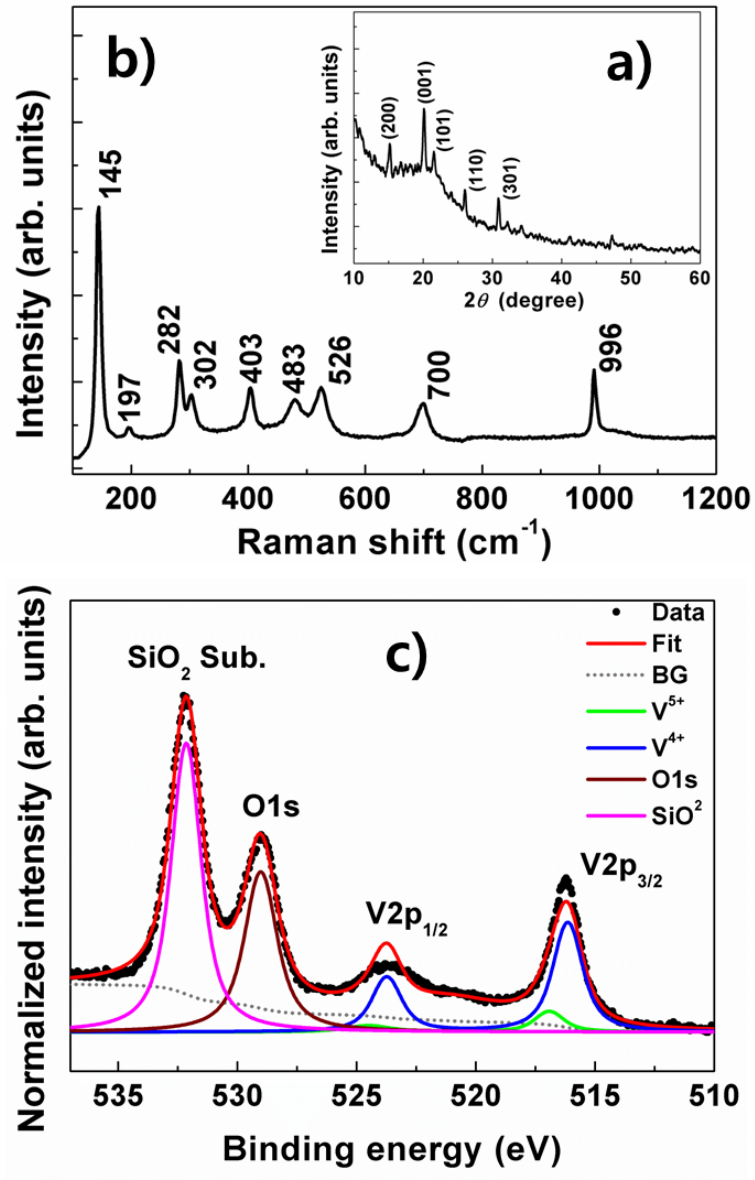

Figure 5.3. (a) XRD pattern and (b) Raman spectrum of V_2O_5 nanospheres. (c) XPS spectrum of the nanospheres. The V2p and O1s core-level spectra shift toward lower binding energy, and the peak at 532.2 eV originated from the SiO_2 substrate.

Fig. 5.4b reveals the PL spectra with the distribution of the nanospheres. As shown in the inset of Fig. 5.4b, the distribution of V_2O_5 nanospheres is not uniform. Therefore, we measured the PL spectra with different distributions of the nanospheres. The PL intensities in locations (1) and (2) with an individual distribution do not change much. However, the intensity at location (3), which has a cluster distribution, significantly decreases over the entire spectral range without variation of the emission shape. This

result is attributed to the reduction of the absorption due to light scattering in the nanospheres with a cluster distribution. The result in Fig. 5.4b is confirmed in Fig. 5.4c and 5.4d. As the spin-coating frequency increases, the nanospheres distribution changes from clusters to many stacks, and the PL intensity decreases considerably without variation of the emission shape.

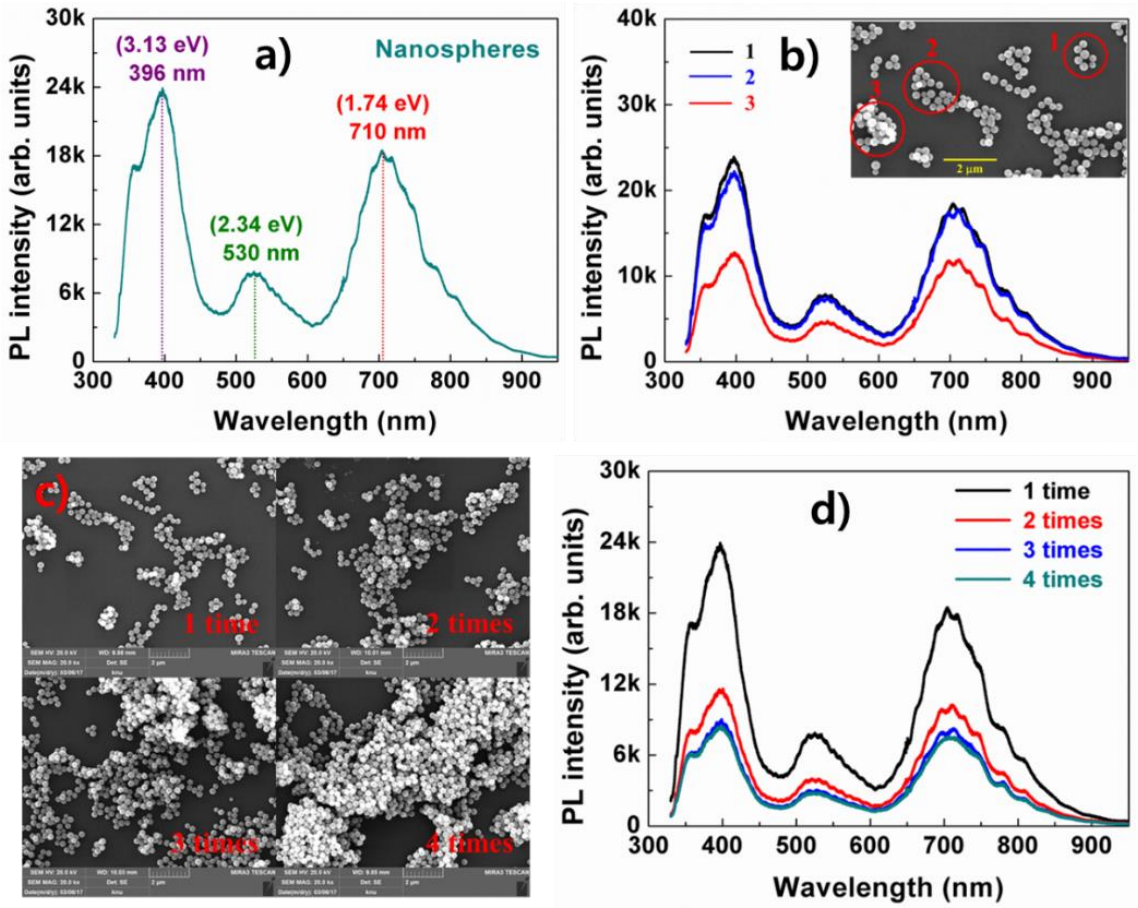

Figure 5.4. (a) Room-temperature PL spectrum in V_2O_5 nanospheres, (b) PL spectra with distribution of the nanospheres and (Inset) SEM image, (c) SEM images, and (d) PL spectra with respect to spin-coating frequency of the nanospheres.

The TRPL spectra for the three PL peaks of the V_2O_5 nanospheres are shown in Fig. 5.5a–d**.** An exponential fit was performed using Symphotime-64 software (Ver. 2.2) with a bi-exponential decay model, $I(t) = \sum A_i e^{-t/\tau_i}$, where $I(t)$ is the time-dependent PL intensity, A is the amplitude, τ is the PL lifetime, and the ordinal i is 1 or 2 in this study. The lifetimes for the PL peaks at 396, 530, and 710 nm were obtained from the bi-exponential decay fit.

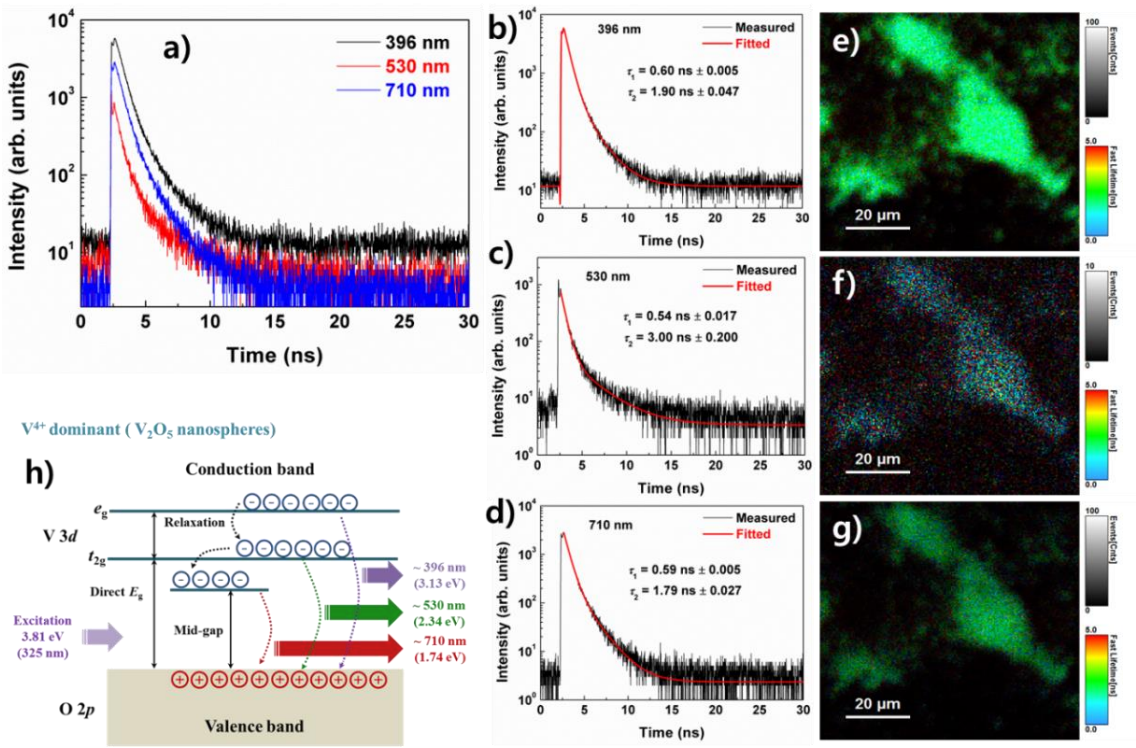

Figure 5.5. (a) TRPL spectra in V_2O_5 nanospheres. The lifetimes for the PL peaks at (b) 396, (c) 530, and (d) 710 nm were obtained from the bi-exponential decay fit. (e)–(g) TRPL images obtained using the time-tagged time-resolved (TTTR) data acquisition method. (h) Band diagram of the PL process of V_2O_5 nanospheres.

As shown in Fig. 5.5b–d, the TRPL spectra of the three PL peaks reveal fast decay with a lifetime of less than 1 ns. The fast component (τ_1) and slow component (τ_2) of the lifetimes for the three PL peaks are 0.6 and 1.90 ns at 396 nm, while they are 0.54 and 3.00 ns at 530 nm and 0.59 and 1.79 ns at 710 nm. This decay feature of the nanospheres may indicate a lack of non-radiative channels. Fig. 5.5e–g show the TRPL images obtained using the TTTR data acquisition method. The images of the PL peaks at 396 and 710 nm reveal similar aspects, whereas the image of the PL peak at 530 nm shows a slow decay feature compared with those at 396 and 710 nm. The increase of the red spot in Fig. 5.5f indicates an increase of the slow component in lifetime.

Fig. 5.5h shows a band diagram for the PL process in the V_2O_5 nanospheres. The electronic band structure of V_2O_5 is formed by the associated hybridization of the O 2*p* orbitals with V 3*d* orbitals (*p*–*d* hybridization) involved in chemical bonding.[86,207,231] The V 3*d* state in the conduction band is split into a low t_{2g} state and a high e_g state. In the case of the V^{4+} ($3d^1$)-dominant nanospheres, carriers are strongly excited due to the

V^{4+}, and the PL peaks originating from the t_{2g} state and mid-gap state are highly enhanced. Furthermore, the highly intense UV PL (~396 nm) is due to carrier recombination in the e_g state.

5.3 Chapter summary

The V_2O_5 nanospheres prepared by a chemical reaction method showed a large amount of V^{4+} oxidation states (84%). Furthermore, the nanospheres revealed very high PL intensity. In particular, the nanospheres showed intense UV PL near 396 nm (3.13 eV), which was attributed to the enhanced transition probability in terms of the large amount of the V^{4+} ($3d^1$) oxidation states. The PL properties of the nanospheres showed strong dependencies on the oxidation state and their distribution on the substrate.

Chapter 6. Photocatalytic Activities of Pure V_2O_5 and V_2O_5/RGO Nanocomposites

6.1 Motivation

V_2O_5 is a semiconductor with three bands: the gap between the top of the O*2p* and the bottom of the V*3d* band at about 3.30 eV, O*2p* and V*3d* split-off at about 2.30 – 2.40 eV, and O*2p* and mid-gap states at about 1.70 - 1.80 eV.[91] Therefore, V_2O_5 can absorb UV-light (3.10 – 3.30 eV), visible-light (2.20 – 2.40 eV), and red light (1.7 – 1.8 eV). Thus, V_2O_5 is suitable for visible sunlight absorption or photocatalytic activity with sunlight.[21,127] However, pure V_2O_5 nanostructures have low photo-degradation efficiency compared with other metal oxides such as TiO_2, $SrTiO_3$, and ZnO.[182] In photocatalytic water splitting, high efficiency was achieved when the bottom level of the CB of the semiconductor was more negative than the redox potential of H^+/H_2 (eV vs. NHE), while the bottom level of the CB of V_2O_5 was less negative.[179,182] This leads to the difficulty of electron transport from V_2O_5 to water molecules reducing to form H_2, resulting in low catalytic activity.

Interestingly, V_2O_5 materials can be prepared with various morphologies to improve the photocatalytic performance. In recent decades, great attention has been given to hetero-nanostructures between V_2O_5 and other nanomaterials such as carbon nanostructures/V_2O_5,[199] and RGO/V_2O_5[200] due to the superior enhancement in the catalytic performance of V_2O_5. In particular, carbonaceous materials are generally employed to improve the photocatalytic activity due to their low cost, environmental friendliness, and large-scale production. Reduced graphene oxide (RGO) has been widely used as an effective supporting material for enhancing the charge transfer and adsorption capability due to unique characteristics including outstanding electrical conductivity, large surface area, and good optical properties. Therefore, V_2O_5/RGO nanocomposites may provide a new generation of materials for excellent photocatalytic activity. Moreover, the multiple advantages such as enhancing performance rate, prolonging cyclability, and higher sulfur utilization rates can be reached by combination of RGO with VO_x.[232,233]

In chapter 4 and chapter 5, V_2O_5 nanospheres showed high PL intensity compared with other nanostructures due to the large number of V^{4+} oxidation states.[164] The presence of V^{4+} enhanced the amount of separation, but the photocatalytic activity of pure V_2O_5 is still low due to the fast recombination of electron-hole pairs. In this chapter, I demonstrate the synthesis of

V_2O_5 nanostructures and V_2O_5/RGO nanocomposites. The role of V^{4+} in pure V_2O_5 in the absorption, PL, and photocatalytic activity is discussed along with the role of RGO in the V_2O_5/RGO nanocomposites for decreasing the emission intensity in the PL and enhancing the photocatalytic efficiency.

6.2 Results and discussion

The SEM image (Fig. 6.1a) shows V_2O_5 NSs with uniform diameters of about 200 - 400 nm. They have spherical morphology with rough surface a due to the growth features of V_2O_5 with a layer-by-layer plate-like structure.[32,219] When the $V(OH)_2NH_2$ NSs were hydrothermally treated at 120 ℃ for 6 h, the $V(OH)_2NH_2$ NSs became NHs. Fig. 6.1b reveals that the rough surface, of the hollows became porous structures. The porous structure can form numerous defects and enhance the surface area. Fig. 6.1c and 6.1d demonstrate that the RGO wrapped and attached to the V_2O_5 nanostructures to form V_2O_5/RGO nanocomposites. The decoration of V_2O_5 on RGO is beneficial for transporting electrons to anywhere on the surface of the sample.

Figs.6.1e and 6.1f show the TEM images of V_2O_5 NSs/RGO and V_2O_5 NHs/RGO composites which clearly reveal the firm contact between RGO ultra-sheet and V_2O_5 nanostructures. The TEM images (Fig. 6.1e) also shows that the NSs are dense and solid with rough surfaces. TEM images (Fig. 6.1f) show porous structures such as nanoparticles and nanoplate-like exists on the surfaces of the V_2O_5 NHs

Fig. 6.2a shows the XRD patterns of pure V_2O_5 nanostructures and V_2O_5/RGO nanocomposites. Both the pure V_2O_5 and V_2O_5/RGO composite samples show diffraction peaks of the V_2O_5 located at around 15.3°, 20.3°, 21.6°, 26.0°, 30.9°, 32.3°, 33.2°, 34.2°, 47.3°, and 51.2°, which correspond to the (200), (001), (101), (110), (301), (011), (111), (310), (600), and (020) planes of orthorhombic α-V_2O_5, respectively.[33,48] The main peak of RGO are not observed in the V_2O_5/RGO due to overlapping with the (110) reflection of V_2O_5.[234]

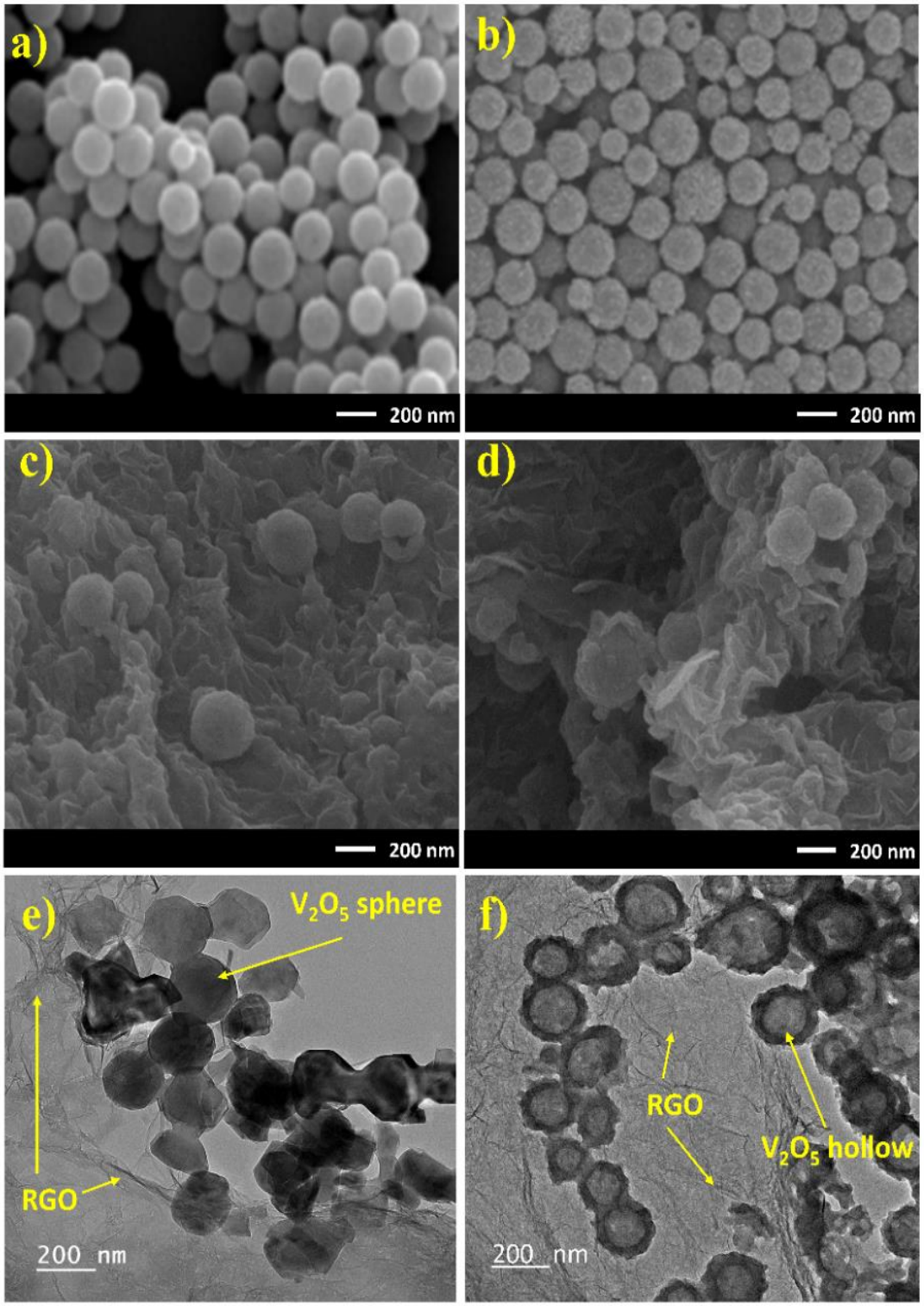

Figure 6.1. SEM and TEM images of V_2O_5 nanostructures and V_2O_5/RGO nanocomposites: (a) V_2O_5 NSs, (b) V_2O_5 NHs, (c) V_2O_5 NSs/RGO, and (d) V_2O_5 NHS/RGO.

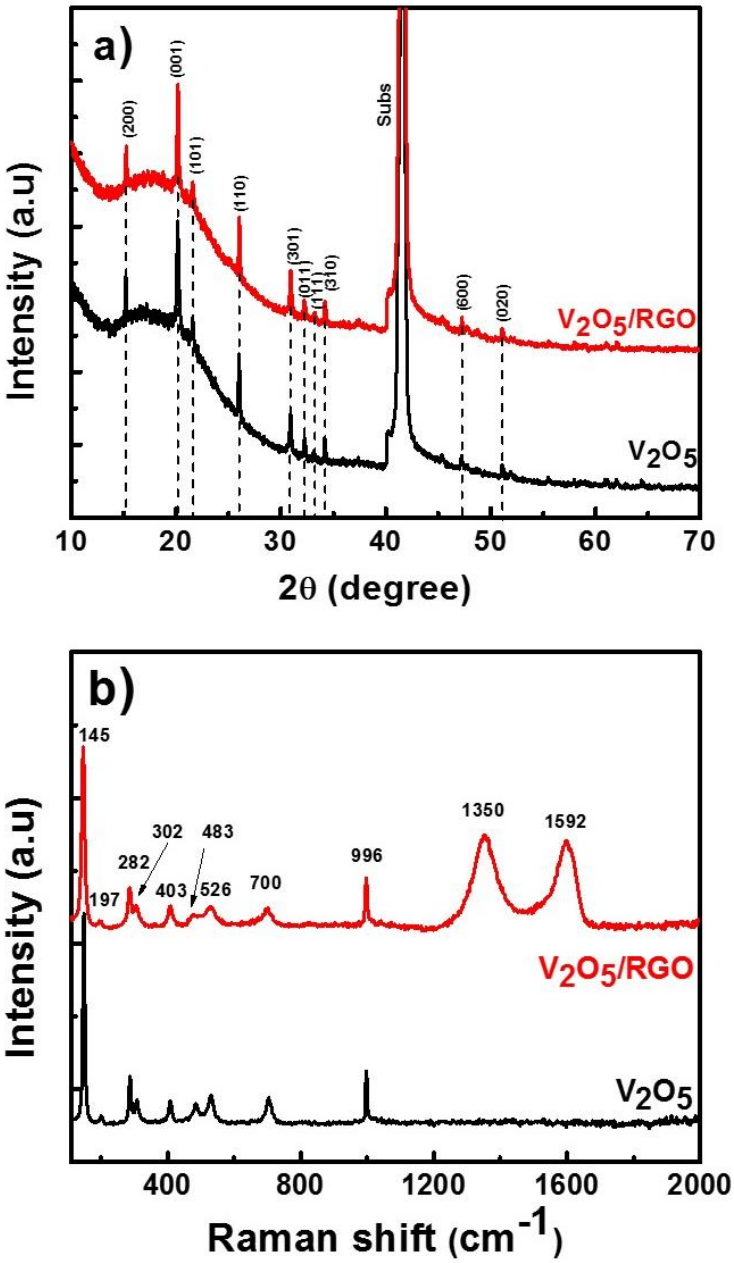

Figure 6.2. (a) XRD patterns and (b) Raman spectra of V_2O_5 NHs and V_2O_5 NHs/RGO nanocomposites.

Raman spectroscopy of the V_2O_5 nanostructures and V_2O_5/RGO nanocomposites (Fig. 6.2b) shows multiple peaks located at 145, 197, 282, 302, 403, 483, 526, 700, and 996 cm^{-1}. The predominant low-frequency peak at 145 cm^{-1} corresponds to the bending mode vibration B_{3g}, while the peak at 197 cm^{-1} comes from the bending vibration of O-V-O. The oscillating A_g mode of V= atoms O is represented by the peaks at 282, 302, and 403 cm^{-1}. The peaks at 483, 526, and 700 cm^{-1} are due to the vibration mode A_g of (V-O_3-V), $v(d_4)$, and $v(d_3)$. The highest-frequency $v(d_1)$ mode at 996 cm^{-1} comes from the displacement of O_1 atoms through V=O_1 double bonds.[30,174,216] The peak at 1350 cm^{-1} corresponds to the D-band of the RGO in the

V_2O_5/RGO composite, and the peak at 1592 cm^{-1} corresponds to its G-band.[235] The shape of the of both the XRD and Raman spectroscopy peaks of V_2O_5/RGO nanocomposites are slightly different compared from those of pure V_2O_5 due to the effects of the RGO attached to the V_2O_5.

Fig. 6.3a shows the XPS survey spectra, which indicates a composition of C*1s*, O*1s*, and V*2p*. Fig. 6.3b shows two peaks at 284.5 eV and 286.8 eV due to the C-C and C-O carbon bonds in RGO.[235] Fig. 6.3c demonstrates the composition of O*1s* in pure V_2O_5, which is shown by the peak at 530.6 eV corresponding to the bonding of oxygen with vanadium in the V_2O_5 lattice. In contrast, the peak in the spectrum for O*1s* in V_2O_5/RGO is shifted to higher energy due to the contribution of the two peaks from the O*1s* bonding of vanadium and carbon in the RGO. The peak at 530.6 eV belongs to O*1s* in pure V_2O_5, while the peak at 531.5 eV belongs to the O*1s* composition of RGO.[191]

Fig. 6.3d shows the variation of the XPS spectra of V_2O_5 nanostructures and V_2O_5/RGO nanocomposites. The V$2p_{3/2}$ peaks at 517.1 eV correspond to the α-V_2O_5 phase.[217] Moreover, the V^{4+} oxidation peak at 516.3 eV is created by the thermal activation of V=O through V=O ↔ V^{4+}+O^- due to the heat treatment.[218] The amount of V^{4+} oxidation states in pure V_2O_5 nanostructures is approximately to 20% that based on the ratio of the area between the curves of V^{4+} and V^{5+} (V^{4+}/V^{5+}).

The absorption curve of V_2O_5 nanostructures shows two regions: one at $hv > 2.34$ eV and a lower one at $hv < 2.34$ eV, as shown in Fig. 6.4 The absorption peaks at 410 nm and at shorter wavelengths correspond to the electronic transition from O*2p* and V*3d* (region I). The absorbed shoulder (region I) from 410 nm to 530 nm corresponds to the transition between O*2p* states and the V*3d* split-off band. The low-energy absorption (region II) with a peak at 610 nm is due to transitions involving the mid-gap states and surface states.

This absorption peak is believed to be caused by V^{4+} oxidation states. V^{4+} was formed due to the oxygen vacancies and creates excess electrons. These excess electrons fill a part of the split-off states and shift the Fermi level to a higher energy state. Moreover, the oxygen vacancies form defect sates (mid-gap state).[118] This leads to the concurrent transition of electrons in V_2O_5 and forms two absorption regions. Compared with pure V_2O_5, the intensity of absorptions in the V_2O_5/RGO composites is slightly different due to the good optical transition of the RGO nanosheets.

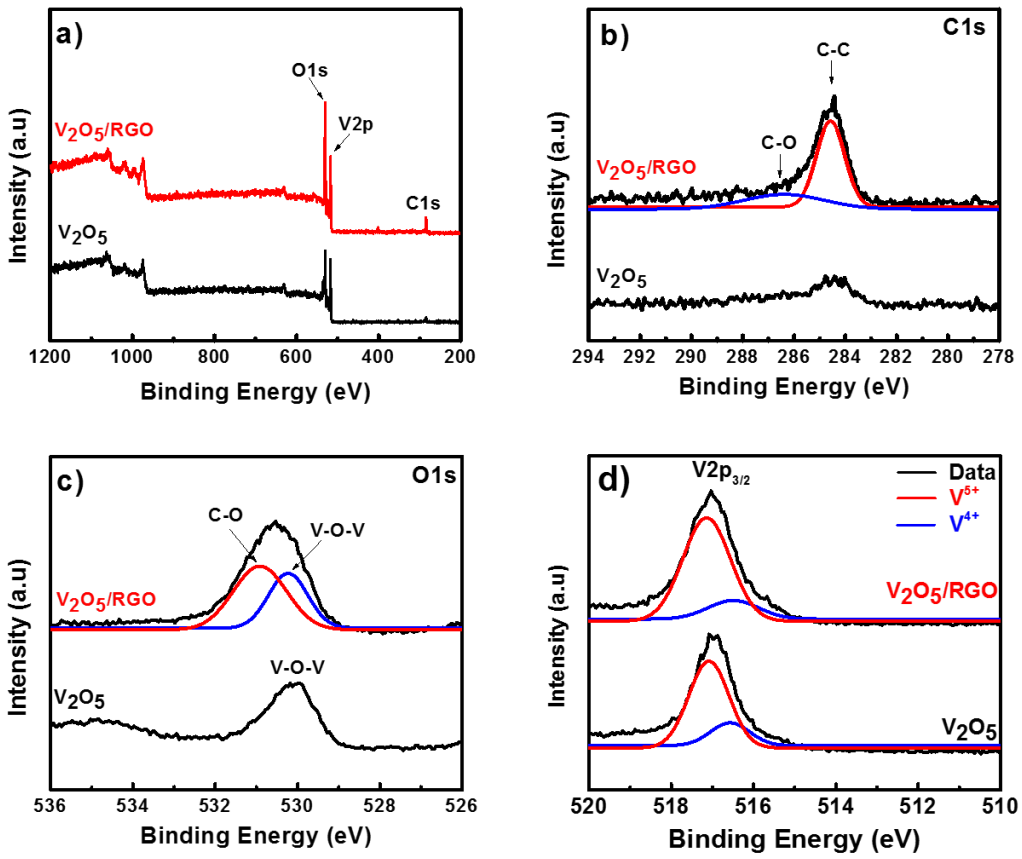

Figure 6.3. XPS spectra of V_2O_5 NHs and V_2O_5 NHs/RGO nanocomposites: (a) Survey spectrum, (b) Fitted C*1s* spectrum, (c) Fitted O*1s* spectrum, (d) Fitted V*2p* spectrum.

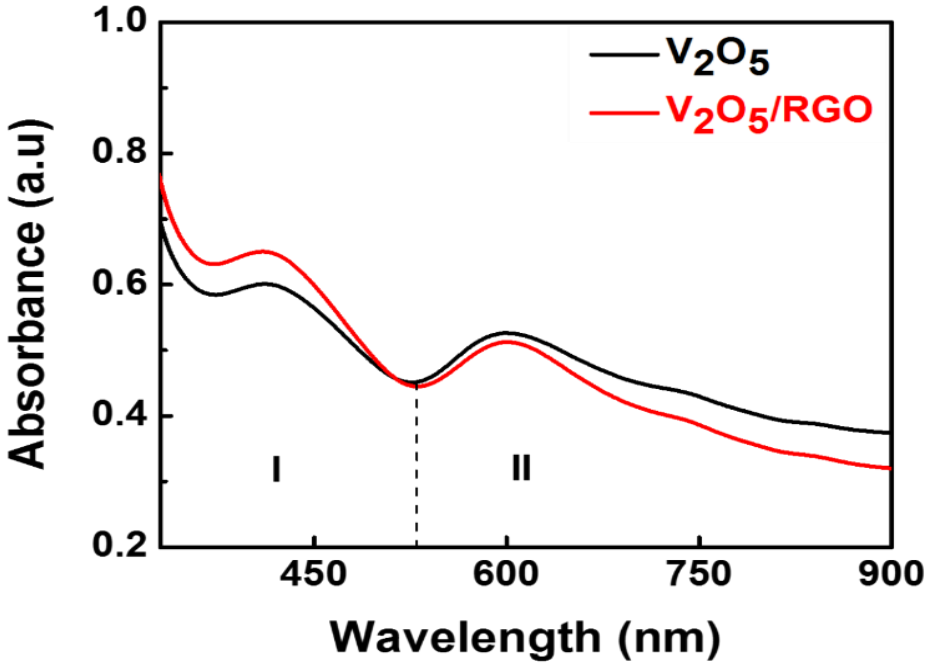

Figure 6.4. Absorption spectra of the V_2O_5 NHs and V_2O_5 NHs/RGO nanocomposites

Fig. 6.5 shows the PL spectra of pure V_2O_5 nanostructures and V_2O_5/RGO nanocomposites measured at room temperature. The PL of V_2O_5 nanostructures showed a broad emission peak centered around 400 – 430 nm and corresponding 3.10 – 2.88 eV, which is caused by the transition from the V*3d* states of the CB to the VB.[61,74] The peak around 510 - 530 nm corresponding to 2.43 – 2.34 eV is due to the band edge transition in V_2O_5.[72,220] The PL peaks centered at about 640 – 710 nm (1.93 – 1.74 eV) in pure V_2O_5 exhibit high intensity, while the peaks in the V_2O_5/RGO nanocomposites are very weak. These peaks were caused by the mid-gap states formed by oxygen vacancies incorporated into the structure during growth.[69]

The PL of V_2O_5 has a relation with the V=O double bond vibration state due to the formation of (V^{4+}-O^{-}) from (V^{5+}=O^{2-}) when it absorbs the laser light.[156–158,222,223] The V^{4+} oxidation in V_2O_5 contributes to the PL intensity due to the enhanced absorption and enhances defect states as surface states and mid-gap states.[164] Defects are formed by excess oxygen during the growth of the materials, so the carriers relax into the CB and can be transferred to this state before recombining with the ground state, which makes an emission peak around 670 nm.

However, the PL of the V_2O_5/RGO nanocomposites reveals that the intensity of the PL peak at 670 nm is lower by approximately 3.2 times in the NSs and 7.6 times in the NHs. We believe that in this case, the electrons easily transfer from the V_2O_5 to the RGO. The diminished PL intensity in V_2O_5 NHs/RGO is lower than that of V_2O_5 NSs/RGO, which could be caused by the strong wrapping of RGO with porous V_2O_5 on the hollow surface. The PL intensity at the peak around 670 nm of the V_2O_5/RGO dramatically decreases compared with that of pure V_2O_5, while the photoluminescence intensity of the two peaks at 400 - 430 nm and 510 - 530 nm is still the same. This result proves that the electrons transfer from V*3d* to the interface and from the mid-gap state to the RGO.

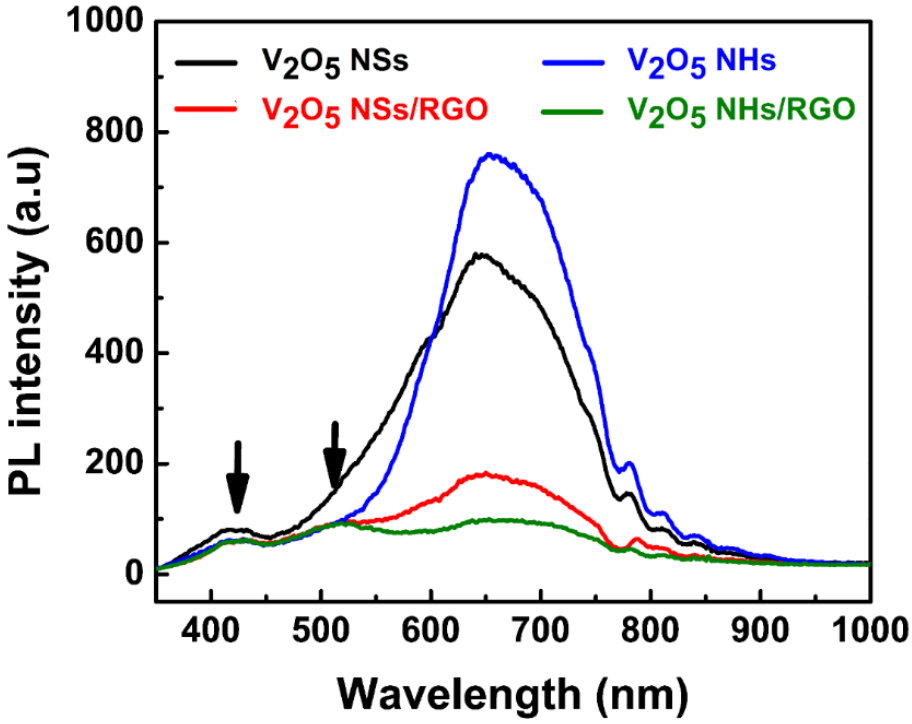

Figure 6.5. PL spectra of the V_2O_5 and V_2O_5/RGO nanocomposites at room temperature.

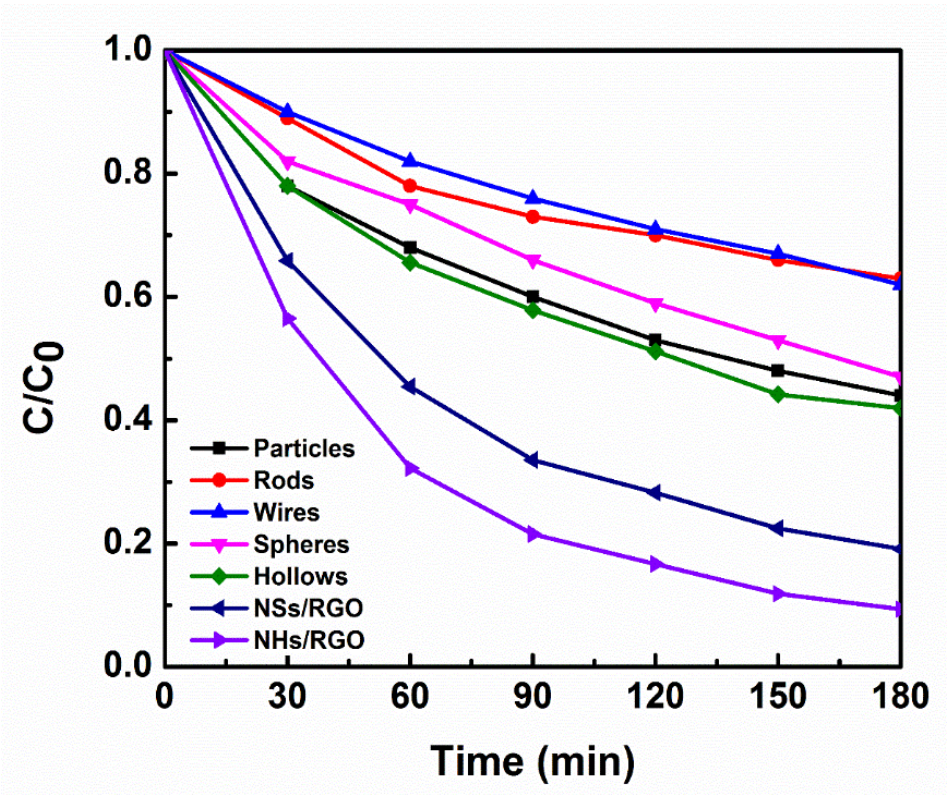

Figure 6.6. Photocatalytic activity of MB dye under sunlight irradiation in pure V_2O_5 and V_2O_5/RGO nanocomposites.

Table 6.1. Photocatalytic performance of V_2O_5 nanostructures and RGO/V_2O_5 hetero-structures.

Sample	Method	Irradiation source, time, and dye solution	Performance (%)	Publication
V_2O_5 nanospheres	WCR	Sunlight, 180 min, Methyl Blue	~52	[236,237]
V_2O_5 nanoparticles.	Hydrothermal		~56	
V_2O_5 nanowires	Hydrothermal		~39	
V_2O_5 nanorods	Hydrothermal		~37	
V_2O_5 nanohollows	WCR+ Hydrothermal		~58	
V_2O_5 NSs/RGO nanocomposites	WCR+ Hydrothermal		~81	
V_2O_5 NHs/RGO nanocomposites	WCR+ Hydrothermal		~91	

Photocatalytic activity measurements were carried out using a UV-vis spectrophotometer (HP8453) and Xe-lamp irradiation every 30 min for 180 min. As shown in Fig. 6.6 and Table 6.1, the enhanced photo-degradation of V_2O_5/RGO nanocomposites was compared with that of pure V_2O_5 nanostructures. In pure V_2O_5 nanostructure, the V_2O_5 NPs, NSs, and NHs have porous surfaces, and the large surface contact area increases the photocatalytic activity compared to NRs and NW. V_2O_5 NHs exhibited higher photocatalytic activity than NSs due to the existence of the porous surface, such as nano-dots on the surface. The surface area measurements reveal that the surface area (Brunauer Emmett Teller – BET) of NHs is 157.4 m^2 g^{-1} and it is larger than that of NSs with 18.6 m^2 g^{-1}. Moreover, the pores on the surface can enhance the absorption due to the multiple reflections of the incident light. However, the

efficiency of pure V_2O_5 is only with 58 % (V_2O_5 NHs), 56 % (V_2O_5 NPs), and 52% (V_2O_5 NSs) after 180 minutes of irradiation due to the recombination being faster than the reduction/oxidation reaction at the surface. The slight enhancing photocatalytic performance in V_2O_5 NHs compared with V_2O_5 NSs demonstrates that the surface area is not the main factor to improve photocatalytic activity in pure V_2O_5 nanostructure due to the less negative of the bottom level of the CB of V_2O_5.

The width of the band gap, amount of charge separation, mobility, and surface area are factors that play important roles in the photocatalytic activity. Compared to pure V_2O_5, V_2O_5/RGO nanocomposites have a larger surface and are more active due to the facilitation of electron transfer and movement on the surface of the RGO nanosheets. The evaluated BETs of V_2O_5 NSs/RGO and V_2O_5 NHs/RGO are 24.5 $m^2 g^{-1}$ and 206.3 $m^2 g^{-1}$, respectively. Moreover, the RGO surface has several residual functional groups like hydroxyl and carboxyl groups.[191] This leads to more $O_2^{\bullet}$ oxide radicals due to the reduction process between electrons and residual functional groups. Therefore, the V_2O_5/RGO nanocomposites have excellent sunlight photocatalytic activity.

Fig. 6.7 shows a diagram of the synthesis of V_2O_5/RGO nanocomposites as well as the relation between absorption, PL, and photocatalytic activity. Fig. 6.7a reveals the relation of the charge separation, recombination, and degradation mechanism. As shown in the absorption and PL spectroscopy of the electron transition (Fig. 6.4 and Fig. 6.5), electrons are separated from the O*2p* states of the VB into three states: V*3d* states ("1" in Fig. 6.7a), V*3d* split-off of CB ("2" in Fig. 6.7a), mid-gap states ("3" in Fig. 6.7a), and from mid-gap states to CB ("4" in Fig. 6.7a), which depend on the absorption wavelength.[69,91,118,164] After that, the electrons easily relax to lower states in the CB ("5" in Fig. 6.7a). Moreover, electrons can relax or recombine to the mid-gap state ("6" in Fig. 6.7a) and recombine with holes at VB ("7", "8", and "9" in Fig. 6.7a).

The PL spectroscopy shows that the PL intensity at the peak around 670 nm is higher than that of the two peaks around 400 – 430 nm and 510 – 530 nm. This means that the electrons tend to relax to the mid-gap state before recombining. The reduction/oxidation reaction at active sites occurs in parallel with recombination.[179] The lowest part of the CB of V_2O_5 lies at about 5.1 eV (Fermi level: about 5.55 eV),[183,184] while the negative potential of the redox potential of H^+/H_2 (0 eV vs. NHE) is about 4.5 eV (vacuum level).[180,185] The VB and CB potentials of V_2O_5 at the point of zero charge can be

calculated using Eq (1.9) and Eq (1.10).[186,187] Therefore, the potential E_x was derived from the PL position where V*3d* of the conduction band is about 0.05 – 0.16 (eV vs. NHE), the V*3d* split-off state is about 0.38 - 0.43 (eV vs. NHE), and the mid-gap state is about 0.63 – 0.73 (eV vs. NHE).

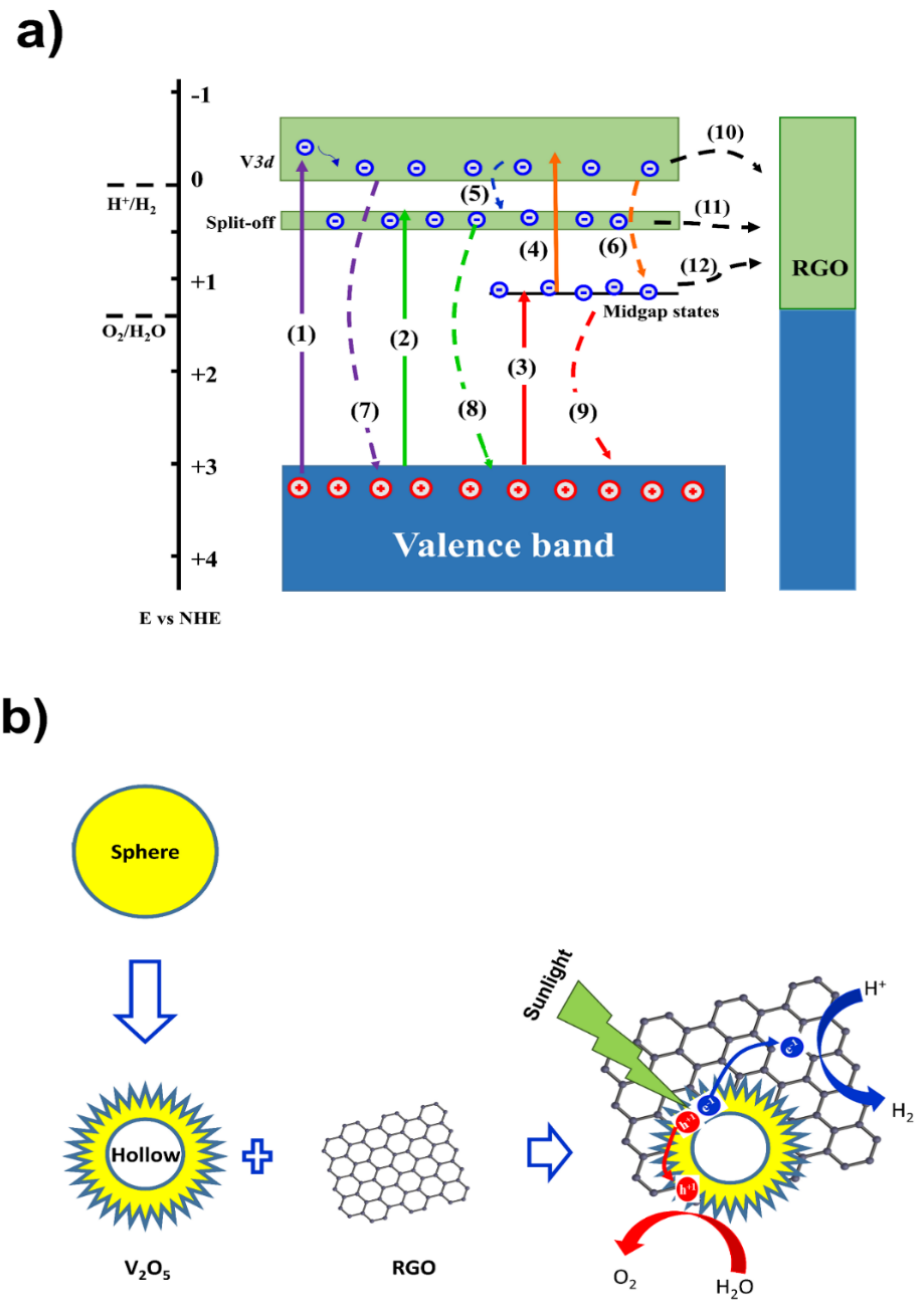

Figure 6.7. (a) Diagram of mechanisms of charge separation by photoexcitation, charge recombination, and charge transportation for photo-degradation of pure V_2O_5 and V_2O_5/RGO nanocomposites. (b) Diagram of formation of V_2O_5 NHs, V_2O_5 NHs/RGO composite, and electron transfer at the interface of V_2O_5 NHs/RGO.

Electrons at the upper state in the CB easily execute reduction reactions, while it is more difficult for electrons at the lowest CB (split-off states) and mid-gap state. The photocatalytic activity mainly occurs due to oxidation to produce $HO^{\bullet}$. The presence of V^{4+} due to the surface defects plays a vital role in the generation of $O_2^{\bullet-}$ radicals.[21] However, the relaxation to lower states in local states and recombination are much faster than the reduction/oxidation reaction in pure V_2O_5, which that leads to lower photo-degradation efficiency.

In the V_2O_5/RGO composite, RGO has high electrical conductivity with the equivalence of a free electron on the hydrogen. Therefore, electrons easily transfer from V_2O_5 to RGO ("10", "11", and "12" in Fig. 6.7a) and move entirely to the surface of RGO nanosheets. This leads to reduced recombination in V_2O_5/RGO nanocomposites.[238] Moreover, RGO has a large surface area, and the Fermi energy level is similar to the NHE of H^+. This leads to a fast reduction reaction and enhanced photocatalytic performance of the V_2O_5 NHs/RGO nanocomposites.

Fig. 6.7b illustrates the formation of V_2O_5 NHs from NSs and V_2O_5 NHs/RGO nanocomposites, the separated electron-hole pairs, and the redox reaction on the surface of the V_2O_5/RGO nanocomposites. The separated electron-hole pairs, electron transfer, and redox reaction of the V_2O_5 NHs/RGO composites can be expressed as Eqs. (6.1) – (6.4):

$$V_2O_5 + RGO \overset{h\nu}{\leftrightarrow} V_2O_5(h^+) + RGO(e^-) \quad (6.1)$$

$$\text{RGO}\ (e^-) + H^+ \rightarrow RGO + O^{\cdot} + H_2 \quad (6.2)$$

$$V_2O_5(h^+) + OH^- \rightarrow V_2O_5 + OH^{\cdot} + O_2 \quad (6.3)$$

$$OH^{\cdot} + O^{\cdot} + MB \rightarrow CO_2 + H_2O \quad (6.4)$$

6.3 Chapter summary

The morphology, crystal structure, and composition of pure V_2O_5 nanostructures and V_2O_5/RGO nanocomposites were investigated by SEM, TEM, XRD, Raman spectroscopy, and XPS. The results showed that the RGO nanosheets wrapped on the V_2O_5 NSs and NHs to form nanocomposites. The V^{4+} oxidation states in V_2O_5 nanostructures form another energy band and extended the absorption range. The

transfer of electrons from V_2O_5 to RGO leads to reduced PL intensity at the peak around 670 nm in V_2O_5/RGO. The results illustrate that V_2O_5/RGO has a large amount of charge separation and high surface area and exhibits excellent photocatalytic activity under sunlight irradiation. The physical and chemical mechanisms of photo-excitation, recombination, and photo-degradation processes were clarified by energy and morphology diagrams.

Chapter 7. Conclusions and Recommendations

7.1 Conclusions

In this work, V_2O_5 micro-nanostructures with various morphologies including thin film, particles, rods, wires, spheres, hollows, and RGO/V_2O_5 composites were successfully fabricated by environmentally friendly and low-cost methods. The morphology, crystal structure, band structure, oxidation state, absorption, photoluminescence, and photocatalytic activity of pure V_2O_5 and V_2O_5/RGO composites were widely discussed.

The background section demonstrates the special electron structure of V_2O_5 to form three bands, including V*3d* states, V*3d* split-off states, and mid-gap states, which lead to interesting optical properties of V_2O_5 micro-nanostructures. They have four main transitions: the transition between VB and V*3d* states of CB, the transition between VB and V*3d* split-off of CB, the transition between VB and the mid-gap defect state, and the transition between mid-gap defect states and CB. The intensity of these transitions was affected by factors such as the morphologies, growth conditions, phase transition, crystal size, micro-nano size, phase mixing, temperature, and so on.

This work also discussed factors such as morphologies and phase transition that affect the band edge of the absorption and peak position of the emission, which lead to the broad emission and PL intensity. In particular, the relation between the absorption, photoluminescence, and photo-degradation shows that the bottom level of the CB of V_2O_5 has to be less negative than the redox potential of H^+/H_2 (eV vs. NHE), but electrons in the CB can react in the oxidation reaction with dye solution.

The annealing temperature strongly affects the surface morphology, structures, the form of micro-nano-rods and plates with coexisting α-V_2O_5 and β-V_2O_5 structures which lead to the strong absorption of visible light, visible PL, and enhanced PL intensity from the band-edge transition. The effect of morphology to the PL properties, the NPs, NRs, and NWs showed weak and broad PL properties, whereas the NSs revealed much higher PL intensity due to numerous oxygen vacancies. Moreover, the effect of NSs distribution

to PL intensity, the NSs revealed very high PL intensity with the individual distribution. The V^{4+} oxidation states in V_2O_5 nanostructures form another energy band and extended the absorption range. It not only affects to PL intensity but also contributes to sunlight photocatalytic activity of pure V_2O_5 micro-nanostructures. The transfer of electrons from V_2O_5 to RGO leads to the reduction of PL intensity at the peak around 670 nm in V_2O_5/RGO composites. The dissertation also demonstrates the role of RGO in V_2O_5/RGO hetero-structures for slowing down recombination, prolonging lifetime, improving electron-hole separation, and increasing photocurrent to enhance the photocatalytic activity.

7.2 Recommendations

Several recommendations can be given for future researches. The most important to get high performance in V_2O_5 micro-nano devices is deep understanding of the fundamental properties of V_2O_5 micro-nanostructures. There are many factors that affect the optical characterization of pure V_2O_5 micro-nanostructures however, the experiments in this work just investigated the effect of the morphologies, distribution, and mixing phase. Other factors such as growth conditions, phase transition, crystal size, micro-nano size, phase mixing, and temperature should be investigated. Moreover, optical properties of metal-doped V_2O_5, material-decorated V_2O_5, and material/V_2O_5 composites should be investigated to compare with low dimension pure V_2O_5.

These results could be used as important data in applications such as photo-catalysts, photovoltaic cells, optical indicators, and white light sources (white light LED). Moreover, due to the layer structure of V_2O_5, the injection or extraction of metal ions can change the color of the V_2O_5 material and M/V_2O_5 composites, so they could be used in electrochromic and smart window. In particular, V_2O_5 micro-nanospheres have numerous oxygen vacancies on the outer shell which leads to high intensity transition in the UV and NIR region, therefore, they can be used in UV and NIR sensor application. These devices could be widely fabricated based on the discussion in this work.

References

[1] M. Liu, B. Su, Y. Tang, X. Jiang, A. Yu, *Adv. Energy Mater.* **2017**, *1700885*, 1.

[2] S. Surnev, M. G. Ramsey, F. P. Netzer, *Prog. Surf. Sci.* **2003**, *73*, 117.

[3] W. Ying, C. Guozhong, *Chem. Mater* **2006**, *18*, 2787.

[4] N. Bahlawane, D. Lenoble, *Chem. Vap. Depos.* **2014**, *20*, 299.

[5] C. R. Cho, S. Cho, S. Vadim, R. Jung, I. Yoo, *Thin Solid Films* **2006**, *495*, 375.

[6] J. Livage, *Materials (Basel).* **2010**, *3*, 4175.

[7] C. Zhang, Q. Yang, C. Koughia, F. Ye, M. Sanayei, S. J. Wen, S. Kasap, *Thin Solid Films* **2016**, *620*, 64.

[8] I. Mjejri, A. Rougier, M. Gaudon, *Inorg. Chem.* **2017**, *56*, 1734.

[9] A. Mauger, C. M. Julien, *AIMS Mater. Sci.* **2018**, *5*, 349.

[10] J. Wisniak, *Educ. Quim.* **2014**, *25*, 455.

[11] J. A. . Ketelaar, *Nature* **1936**, 316.

[12] A. Moretti, S. Passerini, *Adv. Energy Mater.* **2016**, *6*, 1600868.

[13] Y. Yue, H. Liang, *Adv. Energy Mater.* **2017**, *7*, 1602545.

[14] J. Yao, Y. Li, R. C. Massé, E. Uchaker, G. Cao, *Energy Storage Mater.* **2018**, *11*, 205.

[15] X. Liu, J. Zeng, H. Yang, K. Zhou, D. Pan, *RSC Adv.* **2018**, *8*, 4014.

[16] C. Xiong, A. E. Aliev, Ḱ. B. Gnade, K. J. Balkus, *ACS Nano* **2008**, *2*, 293.

[17] K. C. Cheng, F. R. Chen, J. J. Kai, *Sol. Energy Mater. Sol. Cells* **2006**, *90*, 1156.

[18] C. Q. Feng, S. Y. Wang, R. Zeng, Z. P. Guo, K. Konstantinov, H. K. Liu, *J. Power Sources* **2008**, *184*, 485.

[19] S. F. Cogan, N. M. Nguyen, S. J. Perrotti, R. D. Rauh, *J. Appl. Phys.* **1989**, *66*, 1333.

[20] M. Kang, J. Jung, S. Y. Lee, J. W. Ryu, S. W. Kim, *Thermochim. Acta* **2014**, *576*, 71.

[21] M. Aslam, I. M. I. Ismail, N. Salah, S. Chandrasekaran, M. T. Qamar, A. Hameed, *J. Hazard. Mater.* **2015**, *286*, 127.

[22] R. An, H. Liu, C. Zhang, F. Li, *Chem. Eng. J.* **2002**, *23*, 458.

[23] F. Natalio, R. André, A. F. Hartog, B. Stoll, K. P. Jochum, R. Wever, W. Tremel, *Nat. Nanotechnol.* **2012**, *7*, 530.

[24] R. Wang, S. Yang, R. Deng, W. Chen, Y. Liu, H. Zhang, G. S. Zakharova, *RSC Adv.* **2015**, *5*, 41050.

[25] W. Jin, S. Yan, L. An, W. Chen, S. Yang, C. Zhao, Y. Dai, *Sensors Actuators, B Chem.* **2015**, *206*, 284.

[26] A. A. Mane, A. V. Moholkar, *Appl. Surf. Sci.* **2017**, *416*, 511.

[27] Y. Chen, C. Chen, W. Chen, H. Liu, J. Zhu, *Prog. Nat. Sci. Mater. Int.* **2015**, *25*, 42.

[28] C. Zhu, J. Shu, X. Wu, P. Li, X. Li, *J. Electroanal. Chem.* **2015**, *759*, 184.

[29] Y. Wang, K. Takahashi, H. Shang, G. Cao, *J. Phys. Chem. B* **2005**, *109*, 3085.

[30] T. Zhai, H. Liu, H. Li, X. Fang, M. Liao, L. Li, H. Zhou, Y. Koide, Y. Bando, D. Golberg, *Adv. Mater.* **2010**, *22*, 2547.

[31] G. Li, S. Pang, L. Jiang, Z. Guo, Z. Zhang, *J. Phys. Chem. B* **2006**, *110*, 9383.

[32] F. Guo, M. Fan, P. Jin, H. Chen, Y. Wu, G.-D. Li, X. Zou, *CrystEngComm* **2016**, *18*, 4068.

[33] J. Pan, L. Zhong, M. Li, Y. Luo, G. Li, *Chem. - A Eur. J.* **2016**, *22*, 1461.

[34] H. Pang, Q. Song, P. Tian, J. Cheng, N. Zou, G. Ning, *Mater. Lett.* **2016**, *171*, 5.

[35] Y. Yang, S. P. Albu, D. Kim, P. Schmuki, *Angew. Chemie* **2011**, *123*, 9237.

[36] S. Wang, S. Li, Y. Sun, X. Feng, C. Chen, *Energy Environ. Sci.* **2011**, *4*, 2854.

[37] C. Xie, C. Cheng, J. Yang, J. Hou, D. Liu, S. Liu, J. Han, Y. Zhang, M. Xu, *Ceram. Int.* **2016**, *42*, 16956.

[38] S. Liang, Y. Hu, Z. Nie, H. Huang, T. Chen, A. Pan, G. Cao, *Nano Energy* **2015**, *13*, 58.

[39] H. Wang, D. Ma, Y. Huang, X. Zhang, *Chem. - A Eur. J.* **2012**, *18*, 8987.

[40] H. Liu, W. Yang, *Energy Environ. Sci.* **2011**, *4*, 4000.

[41] W. Fan, D. Kirkwood, J. Lu, S. A. Wolf, *Appl. Phys. Lett.* **2009**, *95*, 232110.

[42] S. Hornkjøl, I. M. Hornkjøl, *Electrochim. Acta* **1991**, *36*, 577.

[43] J. Mu, J. Wang, J. Hao, P. Cao, S. Zhao, W. Zeng, B. Miao, S. Xu, *Ceram. Int.* **2015**, *41*, 12626.

[44] N. Wang, Y. Zhang, T. Hu, Y. Zhao, C. Meng, *Curr. Appl. Phys.* **2015**, *15*, 493.

[45] P. P. Wang, Y. X. Yao, C. Y. Xu, L. Wang, W. He, L. Zhen, *Ceram. Int.* **2016**, *42*, 14595.

[46] C. Wu, X. Zhang, B. Ning, J. Yang, Y. Xie, *Inorg. Chem.* **2009**, *48*, 6044.

[47] G. Zhang, L. Yu, H. Bin Wu, H. E. Hoster, X. Wen, D. Lou, **2013**, *5*, 7671.

[48] M. Zou, W. Wen, J. Li, H. Lai, Z. Huang, *J. Alloys Compd.* **2016**, *681*, 268.

[49] M. Wu, X. Zhang, S. Gao, X. Cheng, Z. Rong, Y. Xu, H. Zhao, L. Huo, *CrystEngComm* **2013**, *15*, 10123.

[50] B. Yan, X. Li, Z. Bai, Y. Zhao, L. Dong, X. Song, D. Li, C. Langford, X. Sun, *Nano Energy* **2016**, *24*, 32.

[51] J. Liu, H. Xia, D. Xue, L. Lu, *J. Am. Chem. Soc.* **2009**, *131*, 12086.

[52] H. Shi, H. Liang, F. Ming, Z. Wang, *Angew. Chemie - Int. Ed.* **2016**, *55*, 1.

[53] J. Shao, Y. Ding, X. Li, Z. Wan, C. Wu, J. Yang, Q. Qu, H. Zheng, *J. Mater. Chem. A* **2013**, *1*, 12404.

[54] Q. Yue, H. Jiang, Y. Hu, G. Jia, C. Li, *Chem. Commun.* **2014**, *50*, 13362.

[55] A. Pan, T. Zhu, H. Bin Wu, X. W. Lou, *Chem. - A Eur. J.* **2013**, *19*, 494.

[56] G. C. Huanqiao Song, Cuiping Zhang, Yaguang Liu, Chaofeng Liu, Xihui Nan, *J. Power Sources J.* **2015**, *294*, 1.

[57] D. Vernardou, A. Sapountzis, E. Spanakis, G. Kenanakis, E. Koudoumas, N. Katsarakis, *J. Electrochem. Soc.* **2012**, *160*, D6.

[58] J. K. Lee, G. P. Kim, I. K. Song, S. H. Baeck, *Electrochem. commun.* **2009**, *11*, 1571.

[59] K. Takahashi, S. J. Limmer, Y. Wang, G. Cao, *J. Phys. Chem. B* **2004**, *108*, 9795.

[60] N. K. Nandakumar, E. G. Seebauer, *Thin Solid Films* **2011**, *519*, 3663.

[61] Y. Wang, Q. Su, C. H. Chen, M. L. Yu, G. J. Han, G. Q. Wang, K. Xin, W. Lan, X. Q. Liu, *J. Phys. D. Appl. Phys.* **2010**, *43*, 185102.

[62] L. S. Price, I. P. Parkin, M. N. Field, A. M. E. Hardy, R. J. H. Clark, T. G. Hibbert, K. C. Molloy, *J. Mater. Chem.* **2000**, *10*, 1863.

[63] H. Groult, E. Balnois, A. Mantoux, K. Le Van, D. Lincot, *Appl. Surf. Sci.* **2006**, *252*, 5917.

[64] M. B. Sahana, S. A. Shivashankar, *J. Mater. Res.* **2004**, *19*, 2859.

[65] L. Crociani, G. Carta, M. Natali, V. Rigato, G. Rossetto, *Chem. Vap. Depos.* **2011**, *17*, 6.

[66] D. Barreca, L. Armelao, F. Caccavale, V. Di Noto, A. Gregori, G. A. Rizzi, E. Tondello, *Chem. Mater.*

2000, *12*, 98.

[67] H. A. Le, S. Chin, E. Park, G. Bae, J. Jurng, *Chem. Vap. Depos.* **2012**, *18*, 6.

[68] H. Yin, K. Yu, J. Hu, C. Song, B. Guo, Z. Wang, Z. Zhu, *Dalt. Trans.* **2015**, *44*, 4671.

[69] A. Othonos, C. Christofides, M. Zervos, *Appl. Phys. Lett.* **2013**, *103*, 133112.

[70] H. Yin, K. Yu, H. Peng, Z. Zhang, R. Huang, J. Travas-Sejdic, Z. Zhu, *J. Mater. Chem.* **2012**, *22*, 5013.

[71] M. Kang, I. Kim, S. W. Kim, J.-W. Ryu, H. Y. Park, *Appl. Phys. Lett.* **2011**, *98*, 131907.

[72] M. Kang, M. Chu, S. W. Kim, J.-W. Ryu, *Thin Solid Films* **2013**, *547*, 198.

[73] C. W. Zou, X. D. Yan, D. A. Patterson, E. A. C. Emanuelsson, J. M. Bian, W. Gao, *CrystEngComm* **2010**, *12*, 691.

[74] C. Díaz-Guerra, J. Piqueras, *Cryst. Growth Des.* **2008**, *8*, 1031.

[75] C. Navone, R. Baddour-Hadjean, J. P. Pereira-Ramos, R. Salot, *Electrochim. Acta* **2008**, *53*, 3329.

[76] C. Zou, L. Fan, R. Chen, X. Yan, W. Yan, G. Pan, Z. Wu, W. Gao, *CrystEngComm* **2012**, *14*, 626.

[77] Y. U. Hua, C. Wen, D. A. I. Ying, M. A. I. Liqiang, Q. I. Yanyuan, P. Junfeng, *J. Wuhan Univ. Technol. - Mater. Sci. Ed.* **2006**, *21*, 38.

[78] R. Levi, M. Bar-Sadan, A. Albu-Yaron, R. Popovitz-Biro, L. Houben, C. Shahar, A. Enyashin, G. Seifert, Y. Prior, R. Tenne, *J. Am. Chem. Soc.* **2010**, *132*, 11214.

[79] N. Fateh, G. A. Fontalvo, C. Mitterer, *J. Phys. D. Appl. Phys.* **2007**, *40*, 7716.

[80] P. Balog, D. Orosel, Z. Cancarevic, C. Schön, M. Jansen, *J. Alloys Compd.* **2007**, *429*, 87.

[81] I. P. Zibrov, V. P. Filomenko, S. G. Lyapin, V. A. Sidorov, *High Press. Res.* **2013**, *33*, 399.

[82] M. Prześniak-Welenc, M. Łapiński, T. Lewandowski, B. Kościelska, L. Wicikowski, W. Sadowski, *J. Nanomater.* **2015**, *2015*, 1.

[83] A. Asadov, S. Mukhtar, W. Gao, *J. Vac. Sci. Technol. B* **2015**, *33*, 041802.

[84] P. Singh, D. Kaur, *J. Appl. Phys.* **2008**, *103*, 043507.

[85] S. Beke, *Thin Solid Films* **2011**, *519*, 1761.

[86] A. Chakrabarti, K. Hermann, R. Druzinic, M. Witko, F. Wagner, M. Petersen, *Phys. Rev. B* **1999**, *59*, 10583.

[87] S. Atzkern, S. Borisenko, M. Knupfer, M. Golden, J. Fink, A. Yaresko, V. Antonov, *Phys. Rev. B - Condens. Matter Mater. Phys.* **2000**, *61*, 12792.

[88] J. Haber, M. Witko, R. Tokarz, *Appl. Catal. A Gen.* **1997**, *157*, 3.

[89] Z. R. Xiao, G. Y. Guo, *J. Chem. Phys.* **2009**, *130*, 214704.

[90] M. Singh, P. Kumar, G. B. Reddy, *Adv. Mater. Interfaces* **2018**, *1800612*, 1.

[91] T. K. Le, M. Kang, S. W. Kim, *Mater. Sci. Semicond. Process.* **2019**, *94*, 15.

[92] V. Eyert, K.-H. Höck, *Phys. Rev. B* **1998**, *57*, 12727.

[93] M. V. Ganduglia-pirovano, J. Sauer, *J. Phys. Chem. C* **2008**, *112*, 9903.

[94] J. C. Parker, D. J. Lam, Y. N. Xu, W. Y. Ching, *Phys. Rev. B* **1990**, *42*, 5289.

[95] W. Lambrecht, B. Djafari-Rouhani, J. Vennik, *J. Phys. C Solid State Phys* **1981**, *14*, 4785.

[96] A. Talledo, C. G. Granqvist, *J. Appl. Phys.* **1995**, *77*, 4655.

[97] M. Fox, *Book, Deparment Phys. Astron. Univeristy Sheffied.* **2001**, DOI 10.1119/1.1691372.

[98] J. Tauc, *North-Holland, Amsterdam* **1972**, P.277.

[99] M. Kang, S. W. Kim, Y. Hwang, Y. Um, J. W. Ryu, *AIP Adv.* **2013**, *3*, 052129.

[100] R. Irani, S. M. Rozati, S. Beke, *Mater. Chem. Phys.* **2013**, *139*, 489.

[101] E. Østreng, O. Nilsen, H. Fjellvåg, *J. Phys. Chem. C* **2012**, *116*, 19444.

[102] P. D. Raj, S. Gupta, M. Sridharan, *Ceram. Int.* **2017**, *43*, 9401.

[103] J. Luksich, C. R. Aita, *J. Vac. Sci. Technol. A Vacuum, Surfaces, Film.* **1991**, *9*, 542.

[104] C. R. Aita, M. L. Kao, *J. Vac. Sci. Technol. A Vacuum, Surfaces, Film.* **1987**, *5*, 2714.

[105] C. R. Aita, Y. L. Liu, M. L. Kao, S. D. Hansen, *J. Appl. Phys.* **1986**, *60*, 749.

[106] A. Venkatesan, N. Krishna Chandar, S. Arjunan, K. N. Marimuthu, R. Mohan Kumar, R. Jayavel, *Mater. Lett.* **2013**, *91*, 228.

[107] R. Santos, J. Loureiro, A. Nogueira, E. Elangovan, J. V. Pinto, J. P. Veiga, T. Busani, E. Fortunato, R. Martins, I. Ferreira, *Appl. Surf. Sci.* **2013**, *282*, 590.

[108] R. Abazari, S. Sanati, L. A. Saghatforoush, *Chem. Eng. J.* **2014**, *236*, 82.

[109] N. Singh, A. Umar, N. Singh, H. Fouad, O. Y. Alothman, F. Z. Haque, *Mater. Res. Bull.* **2018**, *108*, 266.

[110] M. Beaudoin, M. Meunier, C. J. Arsenault, *Phys. Rev. B* **1993**, *47*, 2197.

[111] R. Basu, S. Dhara, *J. Appl. Phys.* **2018**, *123*, 161550.

[112] A. Pérez-Pacheco, D. R. Acosta-Najarro, R. Castañeda-Guzmán, H. Cruz-Manjarrez, L. Rodriguez-Fernandez, J. C. Pineda-Santamaría, M. Aguilar-Franco, *J. Appl. Phys.* **2013**, *113*, 184307.

[113] R. P. Blum, H. Niehus, C. Hucho, R. Fortrie, M. V. Ganduglia-Pirovano, J. Sauer, S. Shaikhutdinov, H. J. Freund, *Phys. Rev. Lett.* **2007**, *99*, 226103.

[114] S. K. Jayaraj, V. Sadishkumar, T. Arun, P. Thangadurai, *Mater. Sci. Semicond. Process.* **2018**, *85*, 122.

[115] N. Kenny, C. R. Kannewurf, D. H. Whoop, *J Phys Chem Solids* **1966**, *27*, 1237.

[116] P. Clauws, J. Vennik, *Phys Status Solidi b* **1974**, *66*, 553.

[117] W. Lambrecht, *J. Phys. C Solid state Phys.* **1980**, *13*, 595.

[118] Q. Wang, M. Brier, S. Joshi, A. Puntambekar, V. Chakrapani, *Phys. Rev. B* **2016**, *94*, 245305.

[119] G. Wu, K. Du, C. Xia, X. Kun, J. Shen, B. Zhou, J. Wang, *Thin Solid Films* **2005**, *485*, 284.

[120] M. Benmoussa, E. Ibnouelghazi, A. Bennouna, E. . Ameziane, *Thin Solid Films* **1995**, *265*, 22.

[121] B. Joseph, A. Iadecola, L. Maugeri, M. Bendele, M. Okubo, H. Li, H. Zhou, T. Mizokawa, N. L. Saini, *Appl. Phys. Lett.* **2013**, *103*, 2.

[122] S. Thiagarajan, M. Thaiyan, R. Ganesan, *New J. Chem.* **2015**, *39*, 9471.

[123] S. Raja, G. Subramani, D. Bheeman, R. Rajamani, C. Bellan, *Optik (Stuttg).* **2016**, *127*, 461.

[124] K. Chen, H. Gu, *Thin Solid Films* **2008**, *516*, 4659.

[125] F. N. Dultsev, L. L. Vasilieva, S. M. Maroshina, L. D. Pokrovsky, *Thin Solid Films* **2006**, *510*, 255.

[126] C. L. Wu, Ming-cheng, *J. Solid State Chem.* **2009**, *182*, 2285.

[127] W. Avansi, V. R. De Mendon, O. F. Lopes, C. Ribeiro, *RSC Adv.* **2015**, *5*, 12000.

[128] A. Venkatesan, N. R. Krishna Chandar, A. Kandasamy, M. Karl Chinnu, K. N. Marimuthu, R. Mohan Kumar, R. Jayavel, *RSC Adv.* **2013**, *5*, 21778.

[129] C. Diaz, G. Barrera, M. Segovia, M. L. Valenzuela, M. Osiak, C. O'Dwyer, *J. Nanomater.* **2015**, *2015*, 105157.

[130] C. W. Zou, X. D. Yan, J. Han, R. Q. Chen, W. Gao, *J. Phys. D. Appl. Phys.* **2009**, *42*, 145402.

[131] N. S. Kumar, M. S. Raman, J. Chandrasekaran, R. Priya, M. Chavali, R. Suresh, *Mater. Sci. Semicond. Process.* **2016**, *41*, 497.

[132] H. Liu, Y. Gao, J. Zhou, X. Liu, Z. Chen, C. Cao, H. Luo, M. Kanehira, *J. Solid State Chem.* **2014**, *214*, 79.

[133] Y. Li, J. L. Kuang, Y. Lu, W. Bin Cao, *Acta Metall. Sin. (English Lett.* **2017**, *30*, 1017.

[134] T. Yang, H. Yu, B. Xiao, Z. Li, M. Zhang, *J. Alloys Compd.* **2017**, *699*, 921.

[135] Y. Vijayakumar, G. K. Mani, M. V. R. Reddy, J. B. B. Rayappan, *Ceram. Int.* **2015**, *41*, 2221.

[136] O. Monfort, T. Roch, L. Satrapinskyy, M. Gregor, T. Plecenik, A. Plecenik, G. Plesch, *Appl. Surf. Sci.* **2014**, *322*, 21.

[137] B. Liu, X. Li, Q. Zhao, J. Liu, S. Liu, S. Wang, M. Tade, *J. Mater. Chem. A* **2015**, *3*, 15163.

[138] M. M. Margoni, S. Mathuri, K. Ramamurthi, R. R. Babu, V. Ganesh, K. Sethuraman, *Appl. Surf. Sci.* **2018**, *449*, 193.

[139] T. Puangpetch, S. Chavadej, T. Sreethawong, *Powder Technol.* **2011**, *208*, 37.

[140] B. Yan, L. Liao, Y. You, X. Xu, Z. Zheng, Z. Shen, J. Ma, L. Jong, T. Yu, *Adv. Mater.* **2009**, *21*, 2436.

[141] F. K. Butt, C. Cao, F. Idrees, M. Tahir, R. Hussain, A. Z. Alshemary, *New J. Chem.* **2015**, *39*, 5197.

[142] Y. Zhou, Z. Qiu, M. Lü, A. Zhang, Q. Ma, *Mater. Lett.* **2007**, *61*, 4073.

[143] C. V. Ramana, O. M. Hussain, S. Uthanna, B. S. Naidu, *Opt. Mater. (Amst).* **1998**, *10*, 101.

[144] R. Irani, S. M. Rozati, S. Beke, *Appl. Phys. A Mater. Sci. Process.* **2018**, *124*, 0.

[145] M. B. Sahana, C. Sudakar, C. Thapa, G. Lawes, V. M. Naik, R. J. Baird, G. W. Auner, R. Naik, K. R. Padmanabhan, *Mater. Sci. Eng. B Solid-State Mater. Adv. Technol.* **2007**, *143*, 42.

[146] C. V. Ramana, R. J. Smith, O. M. Hussain, C. C. Chusuei, C. M. Julien, *Chem. Mater.* **2005**, *17*, 1213.

[147] N. M. Abd-Alghafour, N. M. Ahmed, Z. Hassan, S. M. Mohammad, M. Bououdina, M. K. M. Ali, *J. Mater. Sci. Mater. Electron.* **2016**, *27*, 4613.

[148] A. A. Mane, V. V. Ganbavle, M. A. Gaikwad, S. S. Nikam, K. Y. Rajpure, A. V. Moholkar, *J. Anal. Appl. Pyrolysis* **2015**, *115*, 57.

[149] Z. Luo, Z. Wu, X. Xu, M. Du, T. Wang, Y. Jiang, *Vacuum* **2010**, *85*, 145.

[150] S. Thiagarajan, M. Thaiyan, R. Ganesan, *RSC Adv.* **2016**, *6*, 82581.

[151] J. M. Gallardo-Amores, N. Biskup, U. Amador, K. Persson, G. Ceder, E. Morán, M. E. Arroyo y de Dompablo, *Chem. Mater.* **2007**, *19*, 5262.

[152] B. Zhou, Q. Su, D. Y. He, *Chinese Phys. B* **2009**, *18*, 4988.

[153] B. Etemadi, J. Mazloom, F. E. Ghodsi, *Mater. Sci. Semicond. Process.* **2017**, *61*, 99.

[154] A. Bouzidi, N. Benramdane, A. Nakrela, C. Mathieu, B. Khelifa, R. Desfeux, A. Da Costa, *Mater. Sci. Eng. B Solid-State Mater. Adv. Technol.* **2002**, *95*, 141.

[155] M. Benkahoul, M. K. Zayed, A. Solieman, S. N. Alamri, *J. Alloys Compd.* **2017**, *704*, 760.

[156] A. M. Gritscov, V. A. Shvets, V. B. Kazansky, *Chem. Phys. Lett.* **1975**, *35*, 511.

[157] K. Teramura, T. Hosokawa, T. Ohuchi, T. Shishido, T. Tanaka, *Chem. Phys. Lett.* **2008**, *460*, 478.

[158] M. Anpo, I. Tanahashi, *J. Phys. Chem.* **1980**, *84*, 3440.

[159] Y. Wang, Z. Li, X. Sheng, Z. Zhang, *J. Chem. Phys.* **2007**, *126*, 164701.

[160] Y. Hu, Z. Li, Z. Zhang, D. Meng, *Appl. Phys. Lett.* **2009**, *94*, 103107.

[161] C. W. Zou, X. D. Yan, J. M. Bian, W. Gao, *Opt. Lett.* **2010**, *35*, 1145.

[162] D. O. Scanlon, A. Walsh, B. J. Morgan, G. W. Watson, *J. Phys. Chem. C* **2008**, *112*, 9903.

[163] J.-P. Meyn, T. Danger, K. Petermann, G. Huber, *J. Lumin.* **1993**, *55*, 55.

[164] T. K. Le, M. Kang, S. W. Han, S. W. Kim, *RSC Adv.* **2018**, *8*, 41317.

[165] N. V. Hullavarad, S. S. Hullavarad, P. C. Karulkar, *J. Electrochem. Soc.* **2008**, *155*, 84.

[166] L. Wu, Y. Yu, X. Han, T. Xu, Y. Zhang, Y. Li, J. Zhi, *J. Mater. Chem. C* **2013**, *1*, 6703.

[167] M. Li, F. Kong, H. Wang, G. Li, *CrystEngComm* **2011**, *13*, 5317.

[168] I. Pradeep, E. Ranjith Kumar, N. Suriyanarayanan, C. Srinivas, M. V. K. Mehar, *Ceram. Int.* **2018**, *44*, 7098.

[169] M. S. Raman, N. S. Kumar, J. Chandrasekaran, R. Priya, P. Baraneedharan, M. Chavali, *Optik (Stuttg).* **2018**, *157*, 410.

[170] K.-Y. Pan, D.-H. Wei, *Nanomaterials* **2016**, *6*, 140.

[171] M. Kang, E. Oh, I. Kim, S. W. Kim, J. W. Ryu, Y. G. Kim, *Curr. Appl. Phys.* **2012**, *12*, 489.

[172] R. K. Sharma, P. Kumar, G. B. Reddy, *J. Alloys Compd.* **2015**, *638*, 289.

[173] V. G. Pol, S. V Pol, J. M. Calderon-moreno, A. Gedanken, *J. Phys. Chem* **2009**, *113*, 10500.

[174] G. Faggio, V. Modafferi, G. Panzera, D. Alfieri, S. Santangelo, *J. Raman Spectrosc.* **2012**, *43*, 761.

[175] W. Avansi, L. J. Q. Maia, C. Ribeiro, E. R. Leite, V. R. Mastelaro, *J. Nanoparticle Res.* **2011**, *13*, 4937.

[176] S. Nishio, M. Kakihana, *Chem. Mater.* **2002**, *14*, 3730.

[177] S. Krishnakumar, C. . Menon, *Phys. status solidi* **1996**, *153*, 439.

[178] A. Othonos, *J. Appl. Phys.* **1998**, *83*, 1789.

[179] Y. Wang, Q. Wang, X. Zhan, F. Wang, M. Safdar, J. He, *Nanoscale* **2013**, *5*, 8326.

[180] A. Ganguly, O. Anjaneyulu, K. Ojha, A. K. Ganguli, *CrystEngComm* **2015**, *17*, 8978.

[181] A. Kudo, Y. Miseki, *Chem. Soc. Rev.* **2009**, *38*, 253.

[182] M. Miyauchi, A. Nakajima, T. Watanabe, K. Hashimoto, *Chem. Mater.* **2002**, *14*, 2812.

[183] G. Terán-Escobar, J. Pampel, J. M. Caicedo, M. Lira-Cantú, *Energy Environ. Sci.* **2013**, *6*, 3088.

[184] F. Xie, W. C. H. Choy, C. Wang, X. Li, S. Zhang, J. Hou, *Adv. Mater.* **2013**, *25*, 2051.

[185] E. Environ, M. Batzill, *Energy Environ. Sci. View* **2011**, 3275.

[186] J. Su, X. X. Zou, G. D. Li, X. Wei, C. Yan, Y. N. Wang, J. Zhao, L. J. Zhou, J. S. Chen, *J. Phys. Chem. C* **2011**, *115*, 8064.

[187] B. Tatykayev, F. Donat, H. Alem, L. Balan, G. Medjahdi, B. Uralbekov, R. Schneider, *ACS Omega* **2017**, *2*, 4946.

[188] Y. Xu, M. A. . Schoonen, *Am. Mineral.* **2000**, *85*, 543.

[189] Y. Wang, L. Liu, L. Xu, X. Cao, X. Li, Y. Huang, C. Meng, Z. Wang, W. Zhu, *Nanoscale* **2014**, *6*, 6790.

[190] M. Shahid, D. S. Rhen, I. Shakir, S. P. Patole, J. B. Yoo, S. J. Yang, D. J. Kang, *Mater. Lett.* **2010**, *64*, 2458.

[191] M. Shanmugam, A. Alsalme, A. Alghamdi, R. Jayavel, *ACS Appl. Mater. Interfaces* **2015**, *7*, 14905.

[192] H. Yin, K. Yu, C. Song, R. Huang, Z. Zhu, *ACS Appl. Mater. Interfaces* **2014**, *6*, 14851.

[193] X. Xu, S. Kou, X. Guo, X. Li, X. Ma, H. Mao, *J. Phys. Chem. C* **2017**, *121*, 16257.

[194] M. Shahid, I. Shakir, S. J. Yang, D. J. Kang, *Mater. Chem. Phys.* **2010**, *124*, 619.

[195] M. Epifani, S. Kaciulis, A. Mezzi, D. Altamura, C. Giannini, R. Díaz, C. Force, A. Genç, J. Arbiol, P. Siciliano, E. Comini, I. Concina, *Sci. Rep.* **2017**, *7*, 1.

[196] S. Martha, D. P. Das, N. Biswal, K. M. Parida, *J. Mater. Chem.* **2012**, *22*, 10695.

[197] Y. Liu, L. Wang, W. Jin, C. Zhang, M. Zhou, W. Chen, *J. Alloys Compd.* **2017**, *690*, 604.

[198] R. Ajay Rakkesh, D. Durgalakshmi, S. Balakumar, *RSC Adv.* **2015**, *5*, 18633.

[199] P. K. Boruah, S. Szunerits, R. Boukherroub, M. R. Das, *Chemosphere* **2018**, *191*, 503.

[200] E. Aawani, N. Memarian, H. R. Dizaji, *J. Phys. Chem. Solids* **2019**, *125*, 8.

[201] K. Bhattacharyya, S. Varma, A. K. Tripathi, S. R. Bharadwaj, A. K. Tyagi, *J. Phys. Chem. C* **2008**, *112*, 19102.

[202] H. J. Song, M. Choi, J. C. Kim, S. Park, C. W. Lee, S. H. Hong, D. W. Kim, *Mater. Lett.* **2016**, *180*, 243.

[203] W. S. Hummers, R. E. Offeman, *J. Am. Chem. Soc.* **1958**, *80*, 1339.

[204] M. Losurdo, D. Barreca, G. Bruno, E. Tondello, *Thin Solid Films* **2001**, *384*, 58.

[205] Q. Su, W. Lan, Y. Y. Wang, X. Q. Liu, *Appl. Surf. Sci.* **2009**, *255*, 4177.

[206] G. Silversmit, D. Depla, H. Poelman, G. B. Marin, R. De Gryse, *J. Electron Spectros. Relat. Phenomena* **2004**, *135*, 167.

[207] T. M. Tolhurst, B. Leedahl, J. L. Andrews, P. M. Marley, S. Banerjee, A. Moewes, *Phys. Chem. Chem. Phys.* **2016**, *18*, 15798.

[208] C. Lamsal, N. M. Ravindra, *J. Mater. Sci.* **2013**, *48*, 6341.

[209] M. B. Smirnov, V. Y. Kazimirov, R. Baddour-Hadjean, K. S. Smirnov, J. P. Pereira-Ramos, *J. Phys. Chem. Solids* **2014**, *75*, 115.

[210] V. P. Filonenko, M. Sundberg, P.-E. Werner, I. P. Zibrov, *Acta Crystallogr. Sect. B Struct. Sci.* **2004**, *60*, 375.

[211] D. R. Hang, S. E. Islam, K. H. Sharma, S. W. Kuo, C. Z. Zhang, J. J. Wang, *Nanoscale Res. Lett.* **2014**, *9*, 632.

[212] M. Kang, S. W. Kim, Y. Hwang, Y. Um, J.-W. Ryu, *AIP Adv.* **2013**, *3*, 052129.

[213] A. Talledo, B. Stjerna, C. G. Granqvist, *Appl. Phys. Lett.* **1994**, *65*, 2774.

[214] Y. Wang, Z. Li, X. Sheng, Z. Zhang, *J. Chem. Phys.* **2007**, *126*, 2005.

[215] R. Baddour-Hadjean, J. P. Pereira-Ramos, C. Navone, M. Smirnov, *Chem. Mater.* **2008**, *20*, 1916.

[216] C. V. Ramana, R. J. Smith, O. M. Hussain, M. Massot, C. M. Julien, *Surf. Interface Anal.* **2005**, *37*, 406.

[217] M. Demeter, M. Neumann, W. Reichelt, *Surf. Sci.* **2000**, *454*, 41.

[218] Y. Chen, K. Xie, Z. Liu, *Appl. Surf. Sci.* **1998**, *126*, 347.

[219] J. Shao, X. Li, Z. Wan, L. Zhang, Y. Ding, L. Zhang, Q. Qu, H. Zheng, *ACS Appl. Mater. Interfaces* **2013**, *5*, 7671.

[220] Z. . El Mandouh, M. . Selim, *Thin Solid Films* **2000**, *371*, 259.

[221] M. Li, W. Wu, W. Ren, H. M. Cheng, N. Tang, W. Zhong, Y. Du, *Appl. Phys. Lett.* **2012**, *101*, 103107.

[222] H. Garcia, J. M. L. Nieto, E. Palomares, B. Solsona, *Catal. Letters* **2000**, *69*, 217.

[223] H. H. Patterson, J. Cheng, S. Despres, M. Sunamoto, M. Anpo, *J. Phys. Chem.* **1991**, *95*, 8813.

[224] Y. Wang, L. Pan, Y. Li, A. I. Gavrilyuk, *Appl. Surf. Sci.* **2014**, *314*, 384.

[225] L. Abello, E. Husson, Y. Repelin, G. Lucazeau, *Spectrochim. Acta* **1983**, *39A*, 641.

[226] D. W. Murphy, P. A. Christian, F. J. Disalvo, J. V. Waszczak, *Inorg. Chem.* **1979**, *18*, 2800.

[227] L. J. Meng, R. A. Silva, H. N. Cui, V. Teixeira, M. P. dos Santos, Z. Xu, *Thin Solid Films* **2006**, *515*, 195.

[228] G. . Sawatzky, D. Post, *PHSICAL Rev. B* **1979**, *20*, 1546.

[229] Q. H. Wu, A. Thissen, W. Jaegermann, M. Liu, *Appl. Surf. Sci.* **2004**, *236*, 473.

[230] T. M. Tolhurst, B. Leedahl, J. L. Andrews, P. M. Marley, S. Banerjee, A. Moewes, *Phys. Chem. Chem. Phys.* **2016**, *18*, 15798.

[231] R. J. O. Mossanek, A. Mocellin, M. Abbate, B. G. Searle, P. T. Fonseca, E. Morikawa, *Phys. Rev. B* **2008**, *77*, 075118.

[232] Y. Song, W. Zhao, N. Wei, L. Zhang, F. Ding, Z. Liu, J. Sun, *Nano Energy* **2018**, *53*, 432.

[233] Y. Song, W. Zhao, L. Kong, L. Zhang, X. Zhu, Y. Shao, F. Ding, Q. Zhang, J. Sun, Z. Liu, *Energy Environ. Sci.* **2018**, *11*, 2620.

[234] K. Palanisamy, J. H. Um, M. Jeong, W. S. Yoon, *Sci. Rep.* **2016**, *6*, 1.

[235] L. G. Guex, B. Sacchi, K. F. Peuvot, R. L. Andersson, A. M. Pourrahimi, V. Ström, S. Farris, R. T. Olsson,

Nanoscale **2017**, *9*, 9562.

[236] T. K. Le, M. Kang, S. W. Kim, *Mater. Charact.* **2019**, *153*, 52.

[237] T. K. Le, M. Kang, V. T. Tran, S. W. Kim, *Mater. Sci. Semicond. Process.* **2019**, *100*, 159.

[238] S. Dong, Y. Cui, Y. Wang, Y. Li, L. Hu, J. Sun, J. Sun, *Chem. Eng. J.* **2014**, *249*, 102.

List of publication and conference meetings

A. Publications

1) **Top Khac Le,** Manil Kang, Sang Wook Han and Sok Won Kim, Highly intense room-temperature photoluminescence in V_2O_5 nanospheres. *RSC Advances*, 2018, 8, 41317-41322.

2) **Top Khac Le,** Manil Kang, and Sok Won Kim, Room-temperature photoluminescence behavior of α-V_2O_5 and mixed α-β phase V_2O_5 films grown by electrodeposition. *Materials Science in Semiconductor Processing*, 2019, 94, 15-21.

3) **Top Khac Le,** Manil Kang, and Sok Won Kim, Morphology engineering, room-temperature photoluminescence behavior, and sunlight photocatalytic activity of V_2O_5 nanostructures. *Materials Characterization*, 2019, 153, 52-59.

4) **Top Khac Le,** Manil Kang, and Sok Won Kim, A Review on the Optical Characterization of V_2O_5 Micro-Nanostructures. *Ceramics International*, 2019, 45, 15781-15798.

5) **Top Khac Le,** Manil Kang, Van Tam Tran, and Sok Won Kim, Relation of Photoluminescence and Sunlight Photocatalytic Activities on Pure V_2O_5 Nanohollows and V_2O_5/RGO Nanocomposites. *Materials Science in Semiconductor Processing*, 2019, 100, 156-166.

B. Conference meetings

1) **Top Khac Le,** Manil Kang, and Sok Won Kim, Structural and optical properties of nanostructured V_2O_5 films grown by electrodeposition method, KPS-autumn 2016 (poster).

2) **Top Khac Le,** Manil Kang, and Sok Won Kim, V_2O_5 Nanoparticles, Nanorods, and Nanowires: Fabrication, Structural and Optical Characterization, KPS-spring 2017 (oral).

3) **Top Khac Le,** Manil Kang, and Sok Won Kim, Analysis of Room Temperature Photoluminescence from V_2O_5 Micro-Nanospheres, KPS-autumn 2017 (oral, best presentation).

4) **Top Khac Le,** Manil Kang, and Sok Won Kim, Sunlight Photocatalytic Activity of Graphene-V_2O_5 Micro/Nano spheres, KPS-spring 20187 (oral).

5) **Top Khac Le,** Manil Kang, Van Tam Tran, and Sok Won Kim, Enhanced Photocatalytic Activities of V_2O_5 NHs/RGO composites, KPS-autumn 2018 (oral).

6) **Top Khac Le** and Sok Won Kim, Synthesis and physical properties of micro-nanostructured V_2O_5: structure, optical characterization, and sunlight photocatalytic activity, 35th World Congress on Materials Science and Nanotechnology, July-2019 Melbourne, Australia (oral).